

Politechnika Lubelska
Wydział Budownictwa i Architektury

BUDOWNICTWO
I ARCHITEKTURA

Vol. 19(3) 2020

Politechnika Lubelska
Lublin, 2020

Politechnika Lubelska
Wydział Budownictwa i Architektury

BUDOWNICTWO
I ARCHITEKTURA



Vol. 19(3) 2020

Politechnika Lubelska
Lublin, 2020

Rada Naukowa/Scientific Council

Tomasz Bajda (AGH Kraków)
Ivan Baláž (University of Economics in Bratislava)
Mykola Bezv (National University Lviv Polytechnic)
Eduard-Marius Craciun, Ovidius (University of Constanta)
Grażyna Dąbrowska-Milewska (Politechnika Białostocka)
Wiesława Głodkowska (Politechnika Koszalińska)
Adam Goliger (The Council for Scientific and Industrial Research - CSIR)
Zbyněk Keršner (Brno University of Technology)
Halit Cenani Mertol (Atılım University)
Carlos M. Mozos (University of Castilla - La Mancha)
Adam Nadolny (Politechnika Poznańska)
Sandro Parrinello (Pavia University)
Stanislav Pospíšil (Institute of Theoretical and Applied Mechanics)
Wojciech Radomski (Politechnika Łódzka i Politechnika Warszawska)
Elżbieta Radziszewska-Zielina (Politechnika Krakowska)
Petro Rychkov (National University of Water Management and Nature Resources Use)
Shamsher Bahadur Singh (Birla Institute of Technology and Science)
Anna Sobotka (AGH Kraków)
Bogusław Szmygin, Lublin University of Technology, Poland
Thomas Thiis (Norwegian University of Life Sciences)
Viktor Tur (Technical University of Brest)
Tim K.T. Tse (The Hong Kong University of Science and Technology)

Kolegium Redakcyjne/Editorial Board

Redaktor naczelny/Editor-in-Chief: **Wojciech Franus**
Zastępca redaktora naczelnego/Deputy Editor: **Tomasz Lipecki**
Zastępca redaktora naczelnego/Deputy Editor: **Lukasz Borowski**
Sekretariat/Secretary: **Aleksandra Szczypa**

Adres redakcji/Address:

Politechnika Lubelska, Wydział Budownictwa i Architektury
ul. Nadbystrzycka 40, 20-618 Lublin, e-mail: wb.bia@pollub.pl

Strona czasopisma/Journal website:

<https://ph.pollub.pl/index.php/bia/>

Indeksacja/Indexed in:

Arianta, BASE, BazTech, CEEOL, Dimensions, DOAJ, EBSCO, ERIH Plus, Google Scholar, Index Copernicus, Infona, PBN/POL-Index, Publons, Sherpa Romeo, TIB, WorldWideScience

Publikacja wydana za zgodą Rektora Politechniki Lubelskiej.
Published with the consent of the Rector of Lublin University of Technology.

Finansowana w ramach środków Ministra Nauki i Szkolnictwa Wyższego.
Financing by the Polish Ministry of Science and Higher Education.

© Copyright by Politechnika Lubelska 2020

ISSN 1899-0665

Realizacja/Published by: Biblioteka Politechniki Lubelskiej
Ośrodek ds. Wydawnictw i Biblioteki Cyfrowej
ul. Nadbystrzycka 36A, 20-618 Lublin, email: wydawca@pollub.pl


SPIS TREŚCI
CONTENTS

Marcin Burdziński, Maciej Niedostatkiwicz, Patryk Ziółkowski <i>Tests of bond between concrete and steel bars</i> – literature background and program of own research	5
Łukasz Drobiec, Wojciech Mazur, Remigiusz Jokiel <i>Studies on the effects of superficial strengthening with FRCM system</i> on compressive strength of AAC masonry	21
Marcin Giedrowicz <i>Digital fabrication in the process of creation of the parametric concrete fenceings</i>	31
Michał Goldyn, Tadeusz Urban <i>Effect of load level of corner columns on punching shear resistance of flat slabs</i>	41
Jakub Gontarz, Jerzy Podgórski <i>Simulation of four-point beam bending test using the X-FEM method</i>	53
Łukasz Jabłoński, Anna Halicka <i>Influence of the interface reinforcement on static performance</i> of concrete composite T-shaped beams	63
Ewelina Kołodziejczyk, Tomasz Waśniewski <i>Nonlinear analysis of lightweight aggregate concrete columns</i>	77
Wojciech Mazur, Tomasz Rybarczyk <i>Analysis of precast lintel behaviour in AAC masonry walls</i> confined by reinforced lightweight and ordinary concrete	89
Andrzej S. Nowak, Olga Iatsko <i>Load and resistance factors for prestressed concrete girder bridges</i>	101
Małgorzata Pająk <i>Research on the recycled and hybrid fibre reinforced self-compacting</i> concrete under flexure	113
Adam Piekarczyk <i>The experimental investigation of the failure of load-bearing masonry walls</i> supported by a deflecting structure	123

Tests of bond between concrete and steel bars – literature background and program of own research

Marcin Burdziński¹, Maciej Niedostatkiwicz², Patryk Ziółkowski³

¹ *Doctoral School; Gdańsk University of Technology; Gabriela Narutowicza St. 11/12, 80-233 Gdańsk, Poland;*

marcin.burdzinski@pg.edu.pl  0000-0001-5965-4349

² *Department of Concrete Structures; Faculty of Civil and Environmental Engineering; Gdańsk University of Technology; Gabriela Narutowicza St. 11/12, 80-233 Gdańsk, Poland;*

mniedost@pg.edu.pl  0000-0002-6451-6220

³ *Department of Concrete Structures; Faculty of Civil and Environmental Engineering; Gdańsk University of Technology; Gabriela Narutowicza St. 11/12, 80-233 Gdańsk, Poland;*

patziolk@pg.edu.pl  0000-0001-8809-6702

Abstract: This article deals with the issue of the bond between concrete and reinforcement. The bond is crucial for reinforced concrete elements because it is possible to transfer forces (stresses) from concrete to the reinforcement. Basic information related to the cooperation of concrete and rebars was recalled in the article. Selected issues concerning theoretical and numerical analysis as well as experiments of the bond phenomenon were presented. The article also proposes its own concept of experimental studies on the bond on two types of specimens: so-called short specimen and large specimen that will be subjected to *pull-out tests*. The described concept is ultimately to form the basis for creating a numerical model, enabling the simulation of bond in various reinforced concrete elements, calibrated based on the results of experimental studies.

Keywords: reinforced concrete structures, bond, pull-out test, steel deformed bar, concrete

1. Introduction

The basis of reinforced concrete structures work is the interaction between concrete and reinforcement. It is possible due to the bond, i.e. the cooperation of concrete and rebars in the transfer of forces (stresses) caused by loads. In this aspect, the most important are three phenomena related to bond:

- adhesion;
- friction;
- mechanical resistance.

The first phenomenon that affects bond is adhesion. Adhesion is a chemical interaction and the forces (stresses) caused by it between concrete and bar are insignificant (according to researchers, the values of these stresses are usually from 0.4 to 0.8 MPa [1]). The primary bond is involved in the area of adhesion – then in the considered normal cross-section to bar the strain in the reinforcing bar (ε_s) and surrounding tension concrete (ε_{ct}) are given by Eq. 1.:

$$\varepsilon_s(x) = \varepsilon_{ct}(x) \quad (1)$$

If the bond stress exceeds the value of the stress associated with adhesion, then the mechanism of cooperation between concrete and reinforcement is referred to as the secondary bond. This means that in the considered cross-section, the strains of the steel bar (ε_s) are greater than the strains in the tensile concrete surrounding it (ε_{ct}), and the difference between these strains is called slip (s), as shown in Eq. 2:

$$\frac{ds}{dx} = \varepsilon_s(x) - \varepsilon_{ct}(x) \quad (2)$$

If a crack appears (which is primarily associated with exceeding the concrete tensile strength), then the stress at the concrete-bar interface increases rapidly, which causes local loss of bond and slip of reinforcement relative to the concrete. Due to the nature of reinforced concrete structures work, the secondary bond is the main object of analysis.

The second phenomenon that affects the bond is friction. Friction was important for plain bars, which now have been replaced by deformed bars. In the initial phase of the bond mechanism, friction does not play a significant role in the deformed bar. It acquires significance in the situation when there is advanced destruction of the bond, i.e. when the longitudinal cracks formed to the axis of the bar allow slipping at the interface of concrete between the bar ribs and the concrete surrounding the bar. In Fig. 3 the described situation is shown by a horizontal line. Concrete shrinkage plays a positive role in friction, which is usually not desirable in concrete structures due to the appearance of additional tensile stresses. It causes the rebar to be clamped by the concrete.

The last phenomenon affecting the bond is mechanical resistance. It is crucial in the case of deformed bars in terms of cooperation at the concrete-bar interface. In the plain bars used in the past, the only mechanical resistance was the hooks at their ends. Deformed bars interlock in concrete thanks to the ribs, which enable achieving much higher values of bond stress. According to [2], plain bars show up to 1.5 times less bond strength compared to deformed bars. The presence of ribs also causes the formation of internal cracks which at a sufficiently high level of effort are visible on the outer edge of the element (Fig. 1).

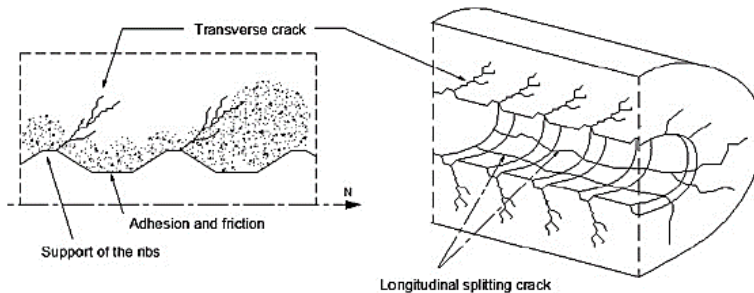


Fig. 1. The action of adhesion, friction, mechanical resistance, and cracking caused by the cooperation of concrete and deformed bar. *Source:* [3]

The problem of bond has been the subject for many years of both theoretical analyses, experimental studies conducted on various specimens as well as numerical analysis. The article will present issues related to the theoretical description of the bond phenomenon between concrete and steel deformed bars, selected methods, and elements for studying this phenomenon will be characterized. Besides, the own program of bond experimental studies will be presented.

2. Bond mechanism between concrete and bar

2.1. Theoretical analysis

The theoretical analysis of cooperation between concrete and reinforcement consists in a mathematical description of phenomena occurring in a reinforced concrete element during its work, which results in the deformability of the element. To make such a description, it is necessary to formulate functions that take into account given quantities in any cross-section on the considered length of the element (e.g. between two adjacent cracks). This section was prepared based on [1]. Important values are:

- strains in tensile concrete in extreme fibres (ε_{ct});
- strains in compressed concrete in extreme fibres (ε_c);
- tensile rebar strains (ε_s);
- bar slip relative to concrete (s);
- bond stress value (τ_b).

There are some assumptions and relationships between the above functions that make up the differential equations.

The first relationship is the strains compatibility condition, which was already presented in Eq. 2. It was assumed that the difference in strains of the rebar and the surrounding concrete is called slip. The interpretation of this condition depends on the analysed part of the specimen. For the specimen face, the slip is the difference in total strains in the rebar and the concrete. For the central part of the specimen, multiplying by two integrated Eq. 2 within the length of the bond violation section can be treated as the crack opening width.

The second relationship is the equilibrium condition of the forces in the cross-section of the bar. On Fig. 2 the equilibrium of the infinitesimal bar segment is presented.

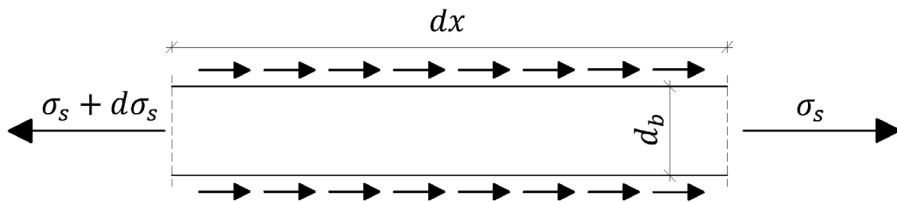


Fig. 2. Equilibrium of the infinitesimal bar segment. *Source:* own study

Equilibrium condition of the infinitesimal bar segment from Fig. 2 is described by Eq. 3:

$$(\sigma_s + d\sigma_s) \cdot \frac{\pi d_b^2}{4} - \sigma_s \cdot \frac{\pi d_b^2}{4} = -\pi d_b dx \tau_b \quad (3)$$

Finally, the equilibrium condition of the forces in cross-section of the bar has the form Eq. 4:

$$\frac{d\sigma_s}{dx} = \frac{-4\tau_b}{d_b} \quad (4)$$

The next relationships are the conditions of forces in the specimen cross-section. The form of these conditions is determined by the stress state of the specimen. Besides, these conditions must consider the bar slip relative to the concrete. Attention should be paid to the principle of flat cross-sections, which, when slip is considered, works only for concrete in the compression zone and reinforcing bars (for eccentric tension or bending).

The last relationship is a bond function. These functions describe the relationship between bond stress and the parameters which the analysed element has. These parameters take into account selected factors affecting the bond. Most often they are related to concrete strength and bar geometry. Bond functions play a key role in the transition from experimental studies to theoretical analysis, which is why they should be as simple as possible and accurately reflect the bond stress distribution relative to the adopted variables. The results of tests carried out in the past indicate that the obtained bond functions accurately represent only a specific situation, which means that it can be assigned to only one specimen. So far, no function has been obtained that comprehensively describes the entire specimen (i.e. the face and centre of the specimen).

Another issue is the “quality” of the bond function, and another the possibility of its use in the theoretical analysis of the bond. “Quality” is understood as the level of accuracy reflecting the distribution of bond stress in the specimen. It sometimes happens that the function is characterized by very high “quality”, but its use in theoretical analysis is not possible due to the differential equation that does not have a closed solution or the adopted boundary conditions relate to a too narrow range of analysis or specific case. The search for the bond function was and is the subject of interest of many researchers who over the years have presented various approaches to this issue. In general, bond functions can be divided into three groups:

Group no. 1– bond functions based on the assumption that the bond depends in any cross-section only on the slip value of the reinforcing bar (s) relative to the concrete surrounding the bar. The functions of the form are determined based on classic pull-out tests. This test consists in pulling out the bar from a concrete block in which the embedded length is from two to five of bar diameter. The most popular bond function representing this group is shown by Eq. 5:

$$\tau_b(s) = \tau_{\max} \cdot \left(\frac{s}{s_{\max}} \right)^\alpha \quad (5)$$

where:

- $\tau_b(s)$ – bond stress value corresponding to bar slip (s);
- τ_{\max} – maximum bond stress value (bond strength);
- s – slip of a pulling out bar;
- s_{\max} – slip corresponding to the value τ_{\max} ;
- α – experimental parameter.

This bond function was first formulated in the 1980s by Bertero, Eligehausen, and Popov. This function is found in CEB-FIP Model 1990 [5], as well as in fib Model Code 2010 [6] as part of the function describing the bond model (in the range $0 \leq s \leq s_1$) (Fig. 3).

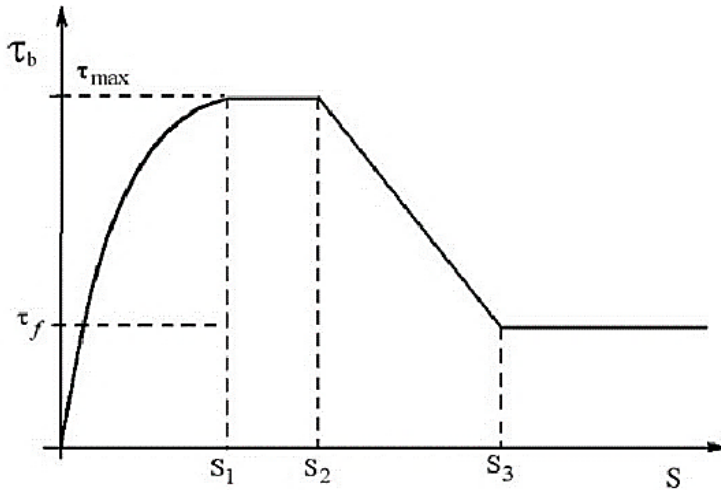


Fig. 3. Bond-slip curve according to CEB-FIP Model 1990 and fib Model Code 2010. *Source:* [5]

Group no. 1 also includes bond functions described by polynomials [7] or simplified linear or bilinear functions.

The undoubted advantage of the bond function from the group no. 1 is the simplicity of the tests that are carried out to determine it, as well as the ease of using them in the models used in FEM analysis. Unfortunately, there are serious and well-founded reservations about these functions. Firstly, Eq. 5 shows that a given slip (s) always corresponds to the same value of bond stress (τ_b), and this is not true. Secondly, the same formula also shows that the greater the slip value, the greater the bond stress value. In the cross-section in which the crack was formed, the bar has the greatest slip relative to the concrete, and the bond stress at this point is, in fact, zero, so the above observation is also not true.

The last problem related to the group no. 1 of the bond function is mathematical because in the deformation analysis these functions lead to differential equations that have no closed-form solutions.

Group no. 2 – bond functions depend on the location of the cross-section over the considered element length (x) and the slip value (s). These functions are determined based on tests carried out on large specimens, i.e. those in which the embedded length is much greater than five diameters of the anchored bar. The progenitor of the bond function from the group no. 2 is Arthur H. Nilson, who in the early 1970s presented his idea of describing the bond stress distribution. An example of the function from the group no. 2 is given by Eq. 6 [8]:

$$\tau_b(x, s) = (k_0 - k_1 x) \cdot s^\alpha \quad (6)$$

where:

$\tau_b(x, s)$ – bond stress value corresponding to the cross-sectional location (x) and the bar slip (s);

k_0, k_1, α – function parameters;

x – bar cross-section location;

s – bar slip.

Bond functions included in this group are characterized by a high level of reflecting the bond stress distribution. Unfortunately, the disadvantage is the lack of universalism because these functions apply to specific cases of tested elements that are not suitable for the analysis of other specimens. Unambiguous interpretation of the results of the experiments is also troublesome. Besides, these functions create problems through a complex mathematical form, which causes a lot of trouble in the theoretical analysis (no closed form). An attempt to get out of the situation is to use simplifications that inevitably reduce the “quality” of the function. An additional complication is a method of obtaining the bar slip value. In practice they are calculated, which raises doubts related to their correctness in relation to the actual values of slip.

A separate problem is the elements used in the tests to determine the bond function of the group no. 2. Unfortunately, the problems are related to the basic issues, which are measurements of strains in the reinforcing bar and concrete. Doubts often arise from the correctness of the measurements taken, their impact on the disturbance of element work, and, consequently, the usefulness of the obtained results. Problems and inconveniences related to that specimen are described in more detail later in the article.

Group no. 3 – bond functions dependent only on the cross-section position (x) between the cracks (independent of slip (s)). The bond functions of this group can be called compromise. Their form allows avoiding problems with obtaining differential equations in a closed-form. These functions depend only on the cross-section position, which is undoubtedly a simplification relative to the function of the group no. 2. It necessarily results in a decrease in the “quality” of these functions. The level of reduction in “quality” depends on the case of the bond function. An example of the function from the group no. 3 is given by Eq. 7 [9]:

$$\tau_b(x) = \tau_{b,\max} \cdot \left[1 - \left(1 - 4 \cdot \frac{x}{l_b} \right)^2 \right] \quad (7)$$

where:

$\tau_b(x)$ – value of the bond stress corresponding to the cross-section position (x);

$\tau_{b,\max}$ – maximum bond stress value (bond strength);

x – bar cross-section location;

l_b – length of the primary bond loss.

As already mentioned, the functions of this group depend on the location of the analysed cross-section. This means that the issue related to conducting the tests is identical to the bond function of the group no. 2, which in turn means the same problems as before. Besides, there is the issue of determining the length of the primary bond loss (l_b), which is most often taken as the distance between two adjacent cracks. The problem is significant because this length occurs in each bond function from the third group (see Eq. 7).

The study of the bond phenomenon and the conclusions drawn from them enable better analysis of the deformation of reinforced concrete elements. Due to the large number of factors that affect the bond, as well as the problems associated with conducting tests, and taking into account the complicated theoretical analysis of the concrete and rebar cooperation, one should approach the bond tests with great caution. According to [10], a general theoretical concept should be created, then on this base, the specimens on which the experiments will be conducted. It is also important to determine the research methodology. This approach can eliminate potential errors, but also increase the chance of better observation of the bond phenomenon. This is a major remark because the mentioned order usually was the reverse.

2.2. Experimental studies

Experimental studies regarding the cooperation between concrete and a deformed bar are carried out on three scales [11]:

- rib scale (Fig. 4a);
- bar scale (Fig. 4b);
- member scale (Fig. 4c).

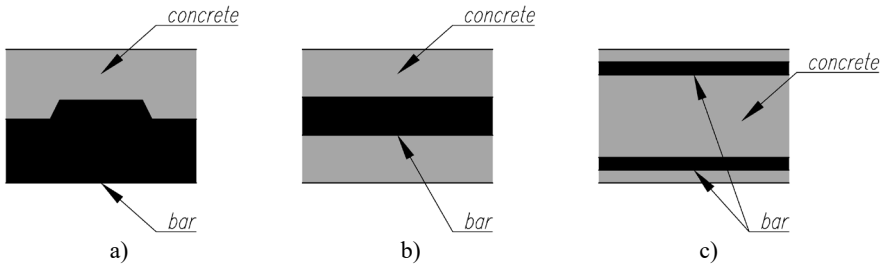


Fig. 4. Scales of the bond observation: a) rib scale, b) bar scale, c) member scale. *Source: own study*

The analysis of bond mechanisms carried out at the rib scale is the most detailed. It relates to contact phenomena occurring at the bar ribs-concrete interface. A classic test at this scale of observation is the *pull-out test* (Fig. 5), from which the information on the mechanisms of destruction of the bond is obtained. The embedded length, i.e. the section where the interaction between the bar and concrete takes place, is from two to five diameters of the pulling out bar ($2 - 5d_b$). They are the so-called “short specimens”, in which it is assumed that over such a short section bond stress has a constant value. The Eq. 8 can be used to determine the value of said bond stress during the *pull-out test*:

$$\tau_b = \frac{F}{\pi \cdot d_b \cdot l_b} \quad (8)$$

where:

τ_b – bond stress;

F – force with which the bar is pulling out;

d_b – bar diameter;

l_b – embedded length.

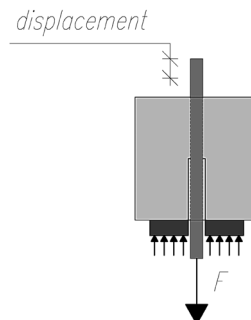


Fig. 5. Specimen using in classic *pull-out test*. *Source: own study*

The *pull-out test* consists in pulling out a reinforcing bar from a concrete block (usually cubic [12], but also cuboidal [13] or cylindrical [14]), during which the force with which the bar is pulling out is measured, and the bar end slip corresponding to this force (free end or free and fixed end). The main result of the *pull-out tests* is the bond-slip curve. Based on this test, bond functions are created and modified that only depend on the slip value (see section 2.1 – group no. 1 of the bond function). Recommendations regarding the *pull-out test* were released e.g. by RILEM [15] and were also included in the standard [16].

The *pull-out test* is extremely popular because it is easy to perform and is inexpensive, and at the same time it considers many factors related to concrete and rebar. That is why there are a lot of publications devoted to this study, in which the influence of selected factors on the bond is checked, e.g. new generation concretes [17], non-metallic bars [18], steel bar corrosion [19], extreme temperatures [18], [20] and others.

Results from a *pull-out test* on a short specimen should not be used for specimens at a different scale of bond observation. This is because the concrete in this test is compressed and the bar is tensile, which is in no way related to the work of the tension zone of the reinforced concrete elements. In addition, the short specimen prevents the formation of internal cracks, which results in excessive values of the bond strength ($\tau_{b,max}$), compared to real reinforced concrete elements. As mentioned, assumptions about the bond function obtained from this test and, as a consequence, their form exclude the possibility of their use in the bond analysis at other scales of bond observation, due to existing contradictions and inconveniences (see section 2.1 – group no. 1 of the bond function).

When conducting analysis at the bar scale, the matter is much more complicated. Carrying out experiments at this scale makes it possible to learn and refine the mechanisms of transfer forces (stresses). The bond stress distribution along the length of the specimen is of key importance. This is important from the point of view of engineering practice because the results of the conducted analysis can affect the calculation and control of the crack opening width and the development length. A typical test for this type of bond observation scale is the *pull-out test* on a large specimen (i.e. one where the embedded length is much greater than five diameters of the anchored bar) or *double pull-out test*, i.e. pulling out the bar on both sides of the specimen (Fig. 6). The advantage of this test is the correct representation of the tension zone of the reinforced concrete element.

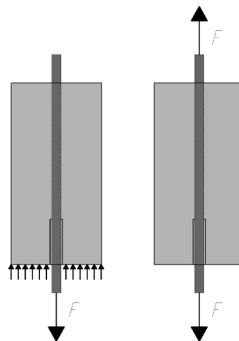


Fig. 6. Large specimen using in *pull-out test* (left), specimen using in *double pull-out test* (right). Source: own study

Analysis at the bar scale is very troublesome. The problem appears at the very beginning when selecting the research element. It must best reflect the conditions in the real structural element

while allowing the observation of phenomena occurring in the specimen. Another big issue is the method of measuring strains both in the reinforcing bar and in concrete. One way to measure strains in a bar is to cut it, place strain gauges inside it and reweld the bar [21]. There are serious doubts about the usefulness of the results obtained in this way. Firstly, cutting and rewelding change the steel structure of the bar. Secondly, making the specimen is difficult and expensive. Thirdly, there is usually a large dispersion of results, which leads to the reflection about which values are consistent with reality. On their basis, the bond stress is determined by Eq. 9:

$$\tau_{b,i} = \frac{-d_b}{4} \cdot \frac{\varepsilon_{s,i+1} - \varepsilon_{s,i-1}}{x_{i+1} - x_{i-1}} \cdot E_s \quad (9)$$

where:

$\tau_{b,i}$ – bond stress in cross-section ;

d_b – bar diameter;

$\varepsilon_{s,i+1}$ – strain in the reinforcing bar in cross-section $i + 1$;

$\varepsilon_{s,i-1}$ – strain in the reinforcing bar in cross-section $i - 1$;

x_{i+1} – position of the cross-section $x + 1$ relative to the specimen face;

x_{i-1} – position of the cross-section $x - 1$ relative to the specimen face;

E_s – Young's modulus of reinforcing steel.

The matter of measuring strains in concrete looks even worse. From the bond analysis, it should be known concrete strains near the bar. It is worth noting that the strains in concrete at the cross-section height are different. Also, the concrete strains along the element length are not uniform due to its cooperation with the reinforcement.

When analysing the bond at the bar scale, attention should be paid to the stress state of the tested specimen. The results of testing a specimen subjected to e.g. axial tension, in the bending element analysis cannot be accepted, because the stress state affects the bond mechanisms [22] and on the way cracks form [23].

Due to the long-embedded length, two types of bond functions are determined and modified based on the bar scale. The first type of bond function depends on the slip and position of the bar cross-section (see section 2.1 – group no. 2 of the bond function), while the second type of bond function depends only on the position of the bar cross-section (see section 2.1 – group no. 3 of the bond function).

The last scale of bond observation is the member scale. Tests on this level are carried out on construction elements, on a laboratory, semi-industrial or industrial scale (real construction elements). Thanks to this, the results of experiments on this observation scale of the bond phenomenon can be easily applied to engineering practice related primarily to the process of designing reinforced concrete structures (e.g. determination of the development length). Due to the widespread use, the most common research element on this scale is a simply supported reinforced concrete beam.

Because of the analysed specimen size, the bond is represented by the *tension stiffening* phenomenon. This phenomenon considers the effect of concrete work in the tension zone of a reinforced concrete element after cracking. During the design process, it is assumed that only reinforcement works in the tension zone. In fact, concrete also cooperates with reinforcement between cracks, which has a positive effect on the stiffness of the entire element.

In summary, the study of the bond phenomenon between concrete and reinforcing bars is carried out at three scales. Their selection determines the detail of the analysis, the method

of conducting investigations, and the obtained results. Unfortunately, the transition between these scales is not easy, which is a significant obstacle to the development of bond analysis. The most important for engineering practice are the two discussed scales of bond observation, i.e. bar scale and member scale, as the results obtained from them have the greatest impact on the issues of designing concrete structures. In the literature, one can find remarkable suggestions for the transition between these scales [24], as well as examples of their use [25].

2.3. Numerical analysis

The third way to analyse the bond between concrete and reinforcement is to use computer engineering analysis. Models used in computer mechanics for analysis of the bond have a broad spectrum – from simple linear finite elements imitating the interaction of concrete and reinforcement [26], through a simplified approach to bond modelling [27], ending with advanced, detailed, three-dimensional models using the fracture mechanics and taking into account formation of internal cracks in the vicinity of the bar [28].

Numerical analysis can consider many factors related to the bond and successfully reflect the specimens state subjected to tests. However, these analyses complement and extend the theoretical analysis and experimental studies. This is because the material models used in numerical calculations are calibrated based on experiments. There are therefore two doubts. Firstly, all problems and inconveniences associated with specimens and tests also automatically concern the computational model. Secondly, the computational model (better or worse) reflect specific specimen, while for another it may not show satisfactory convergence, which is characteristic of experimental studies, because their results are often burdened with the size effect, which consists in counting the influence of the element proportion on the characteristics of its work. That is why it is so important that the selected numerical models are based on algorithms concerning the lack or minimization of the size effect [29], [30].

3. Own program of testing the bond in concrete

The presented review on theoretical analysis, experimental studies and numerical analysis of the bond phenomenon was the basis for developing the authors' own program for testing cooperation between the concrete and deformed bar. The proposed solutions constitute a compromise, bearing in mind the problems, doubts and controversies that arise from the analyses described, e.g. the problem of measuring strains in a reinforcing bar. The main goal of this concept is the validation of the numerical model using the results of experimental studies of the bond phenomenon, which will allow for satisfactorily accurate simulation of the cooperation concrete and steel ribbed reinforcing bars in selected reinforced concrete elements. The authors would like to point out that this concept is at the initial stage of its creation. Its first stage is experimental studies of the bond using the *pull-out test* method.

3.1. Research elements – so-called short specimen

For the short specimen, a 16 mm diameter steel deformed bar (B500SP EPSTAL) anchored in a concrete cube (C30/37) with a side length equal to 160 mm (ten times the bar diameter) will be used for the *pull-out test*. The embedded length will be 80 mm (five times the bar diameter). It can, therefore, be assumed that the bond stress distribution over this section is constant, and the strains change along the bar axis are linear. On the

remaining 80 mm the bar will be surrounded by a 20 mm inner tube to ensure that the bar and concrete do not work together. The tube will not have contact with the pulling out bar, so it will not disturb measurements made during the test. The described specimens were mainly developed based on RILEM recommendations [15].

Tests will be carried out on four different specimens differing in position of the pulling out bar – i.e. in the middle of the specimen height (Fig. 7a), shifted down by 20 mm (Fig. 7b), shifted down by 40 mm (Fig. 7c) shifted down by 47 mm (Fig. 7d) relative to the centre of the specimen. The cover of the bars, measured from the bottom of the specimen, will be 72, 52, 32, 25 mm, respectively. The formwork for the described specimens is shown in Fig. 8.

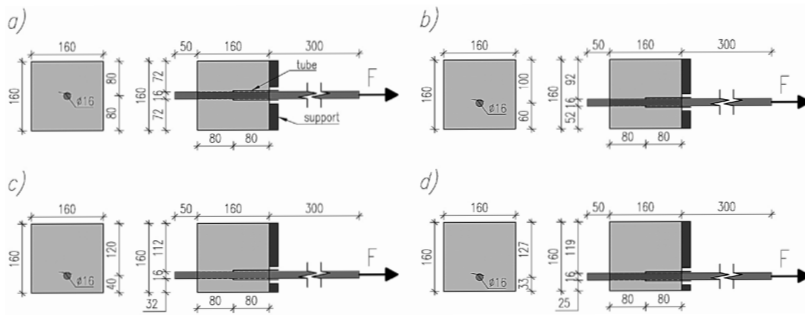


Fig. 7. Details of short specimens (description in the text). *Source:* own study

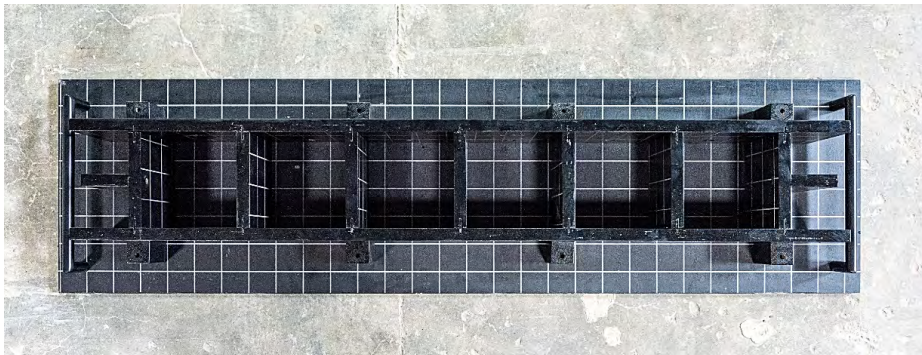


Fig. 8. Short specimens formwork. *Source:* own study

3.2. Research elements – so-called large specimen

For the large specimen, the *pull-out test* will be used a 16 mm steel deformed bar (B500SP EPSTAL) anchored along the axis of the concrete cuboid (C30/37) with a 160 mm square section and 800 mm length (five times the short specimen length). The bar cover will be equal to 72 mm. The embedded length will be 720 mm (45 times the diameter of the pulling out bar). In this situation, it is not possible to assume a constant bond stress distribution on this section of cooperation between the concrete and the bar. A tube is to be placed on the 80 mm section insulating the bar from the side of the loaded end of the bar, analogously to the short specimen, which will allow comparison of the bond stress distribution in the face part of the large specimen and short specimen.

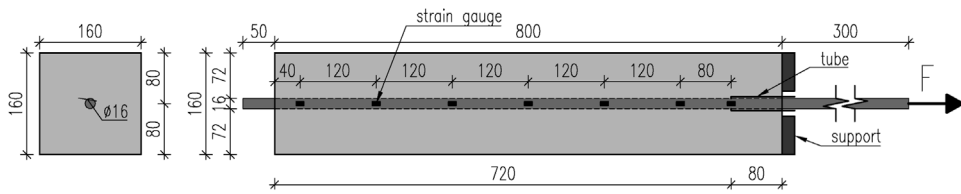


Fig. 9. Details of large specimen (description in the text). *Source:* own study

Strain gauges will be mounted on the surface of the reinforcing bar. Their spacing and other details of the large specimen are shown in Fig. 9. The relatively large spacing of strain gauges is dictated by their impact on the cooperation of concrete and the reinforcing bar. A smaller spacing would interfere too much with the analysed bond phenomenon. Fig. 10 shows the formwork for large specimens.

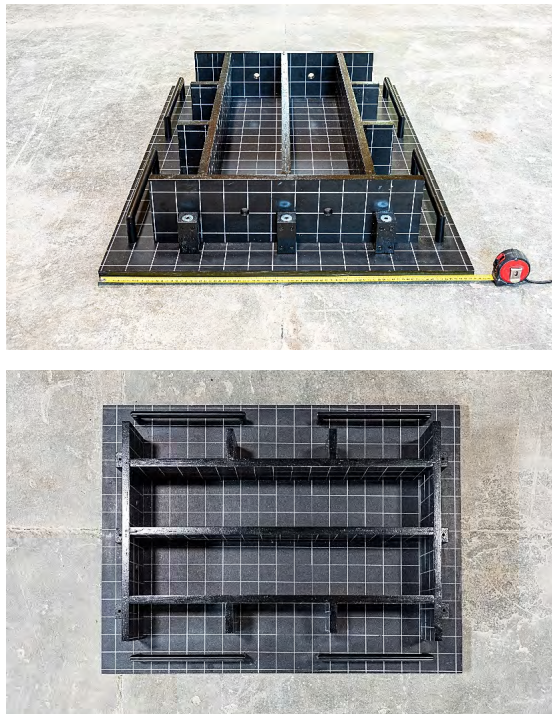


Fig. 10. Large specimens formwork. *Source:* own study

3.3. Test stand

Fig. 11a shows a schematic view of the test stand for *pull-out tests*. It is a metal cage in which the test specimen is located. The reinforcing bar anchored in the concrete block is clamped by the lower grips of the testing machine. In fact, the concrete block is pulling out from the reinforcing bar. The displacement of the unloaded bar end is measured relative to the upper surface of the concrete block. The described cage is adapted for testing both short and large specimens. Fig. 11b shows the cage that the authors of the article use during research in the laboratory.

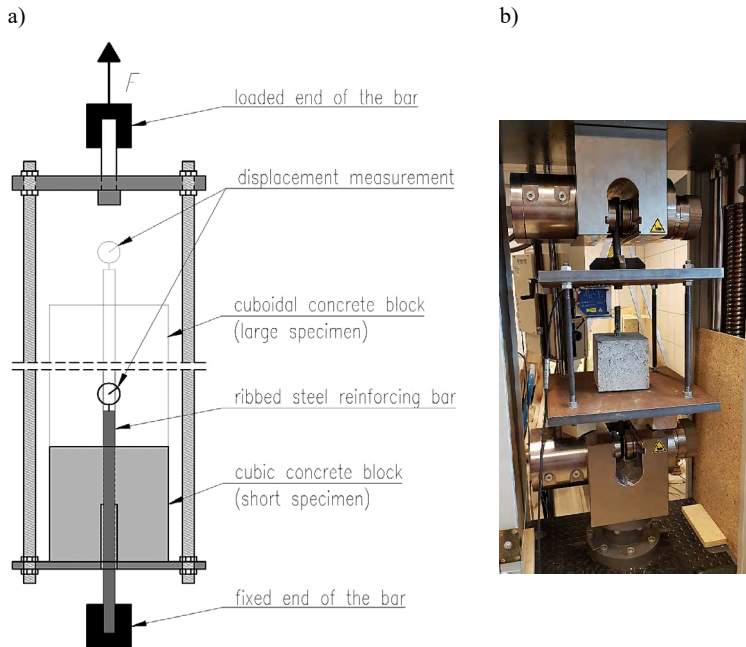


Fig. 11. a) Schematic view of the test stand, b) The actual view of the test stand. *Source:* own study

3.4. Expected test results

Pull-out tests on short specimens are typical bond tests at the rib scale (see section 2.2). The result of this type of testing will primarily be the bond-slip curve ($\tau - s$). Thanks to the different locations of the bar in the concrete block (different bar cover thickness), it will be possible to observe the effect of the position of the pulling out bar on the said curve and on the manner of bond destruction in the specimen (splitting or pull-out failure) [31].

Pull-out tests on large specimens are tests at the bar scale (see section 2.2). This level of bond observation requires strain measurements in the reinforcing bar. It has been assumed that strain gauges will be located on the bar surface. Their spacing and other details of the large specimen are shown in Fig. 9. The results of the *pull-out test* for a large specimen are the determination of the bond stress distribution along the bar axis based on the measured strains, in accordance with Eq. 9. In addition, it is possible to observe the crack pattern of the concrete specimen and possibly compare the values and bond stress distribution in the face of a large specimen and in the short specimen.

4. Summary

The analysis of the bond phenomenon in reinforced concrete structures is complicated. It results, among others, from the difficulties of conducting experimental studies or advanced computer simulations, as well as often mathematical descriptions are difficult. In addition, the bond is affected by many factors that decide about the cooperation of concrete and reinforcing bars.

This article proposes the authors' own experimental studies program for concrete and reinforcement interaction. Creating our own research program will allow for a better understanding of the effect of the bond in reinforced concrete structures and may help to systematize the conduct of experiments. It should be noted that creating such a concept is a process. In the future, this concept will be developed by carrying out tests on various types of specimens and their modifications.

The cooperation of concrete and rebars in reinforced concrete elements is tested using three types of analysis: theoretical, experimental, and numerical. These types of analyses are not independent of each other. This observation is particularly important when creating own concept of experimental studies because its main goal is to collect the necessary results and information for validation of the numerical model, which will allow for satisfactorily accurate simulation and consideration of the bond phenomenon in selected reinforced concrete elements.

References

- [1] Pędziwiatr J., *Podstawowe zagadnienia przyczepności stali i betonów w elementach żelbetowych*. Oficyna Wydawnicza Politechniki Wrocławskiej, Wrocław 2007.
- [2] Grabiec K., *Projektowanie przekrojów w konstrukcjach z betonu*. Arkady, Warszawa 1982.
- [3] Sulaiman M.F. et al., "A Review on Bond and Anchorage of Confined High-strength Concrete", *Structures*, 2017 (11), pp. 97-109. <https://doi.org/10.1016/j.istruc.2017.04.004>
- [4] EN 1992-1-1, Eurocode 2: *Design of Concrete Structures – Part 1-1: General Rules and Rules for Buildings*, 2004.
- [5] *CEB-FIP Model Code*, First Draft, Committee Euro-International du Beton, Bulletin d'information, no. 195, 196, Mars 1990.
- [6] *fib Model Code for Concrete Structures 2010*.
- [7] Mirza S., Houde J., "Study of Bond Stress-Slip Relationships in Reinforced Concrete", *ACI Journal*, vol. 76, no. 1, Symposium Paper, January 1979, pp. 19-46.
- [8] Kankam Ch., "Relationship of Bond Stress, Steel Stress, and Slip in Reinforced Concrete", *Journal of Structural Engineering*, 1997, vol. 123, no. 1, pp. 79-85.
- [9] Jiang D., Shah S., Andonian A., "Study of the Transfer of Tensile Forces by Bond", *Journal of the American Concrete Institute*, May-Jun 1984, 81(3), pp. 251-259.
- [10] Pędziwiatr J., "The new model for cracking analysis of tension reinforced concrete members based on the bond-slip relationships", *Arch. Viv. Eng.*, 1996, vol. 42, no. 1, pp. 47-64.
- [11] Cox J., Herrmann L., "Development of a plasticity bond model for steel reinforcement", *Mech. Cohesive-Frict. Mater.*, 1998, vol. 3, pp. 155-180. [https://doi.org/10.1002/\(SICI\)1099-1484\(199804\)3:2<155::AID-CFM45>3.0.CO;2-S](https://doi.org/10.1002/(SICI)1099-1484(199804)3:2<155::AID-CFM45>3.0.CO;2-S)
- [12] Zhao J., Cai G., Yang J., "Bond-slip behavior and embedment length of reinforcement in high volume fly ash concrete", *Materials and Structures*, 2016, vol. 49, pp. 2065-2082. <https://doi.org/10.1617/s11527-015-0634-2>
- [13] Li X., Zhang J., Liu J., Cao W., "Bond Behavior of Spiral Ribbed Ultra-high Strength Steel Rebar Embedded in Plain and Steel Fiber Reinforced High-Strength Concrete", *KSCE Journal of Civil Engineering*, 2019, vol. 23, no. 10, pp. 4417-4430. <https://doi.org/10.1007/s12205-019-2449-0>
- [14] Deshpande A.A., Kumar D., Ranade R., "Temperature effects on the bond behavior between deformed steel reinforcing bars and hybrid fiber-reinforced strain-hardening cementitious composite", *Construction and Building Materials*, 2020, vol. 233. <https://doi.org/10.1016/j.conbuildmat.2019.117337>
- [15] RILEM/CEB/FIP, *Recommendations on reinforcement steel for reinforced concrete*, Revised edition of RC6 Bond test for reinforcement steel: (2). *Pull-out test*, CEB News, May 1983, no. 73.

- [16] *PN-EN 10080 – Stal do zbrojenia betonu – Spajalna stal zbrojeniowa – Postanowienia ogólne*, 2007.
- [17] Ganesan N., Indira P.V., Sabeena M.V., “Bond stress slip response of bars embedded in hybrid fibre reinforced high performance concrete”, *Construction and Building Materials*, 2014, vol. 50, pp. 108-115. <https://doi.org/10.1016/j.conbuildmat.2013.09.032>
- [18] Solyom S., Di Benedetti M., Guadagnini M., Balázs G.L., “Effect of temperature on the bond behaviour of GFRP bars in concrete”, *Composites Part B: Engineering*, 2020, vol. 183. <https://doi.org/10.1016/j.compositesb.2019.107602>
- [19] Chen J., Zhang B., Yang O., Long S., Xu F., Yang C., “Impact of anchorage length on bond performance between corroded reinforcing steel bars and concrete”, *Materials Reports*, 2019, vol. 33, pp. 3744-3751. <https://doi.org/10.11896/cldb.18110090>
- [20] Bednarek Z., Ogrodnik P., Kamocka-Bronisz R., Bronisz S., „Badanie wpływu temperatur występujących w czasie pożaru oraz szokowego chłodzenia na przyczepność stali B500SP i BST500S do betonu”, *Safety & Fire Technique / Bezpieczeństwo i Technika Pożarnicza*, 2013, vol. 29, no. 1, pp. 67-73.
- [21] Liu K., Yan J., Zou C., Meng X., “Bond behavior between deformed steel bars and recycled aggregate concrete after freeze-thaw cycles”, *Construction and Building Materials*, 2020, vol. 232. <https://doi.org/10.1016/j.conbuildmat.2019.117236>
- [22] Base G., “Bond and Control of Cracking in Reinforced Concrete”, in *International Conference Bond in Concrete*, Applied Science Publishers, London 1982, pp. 446-447.
- [23] Drobiec Ł., Jasiński R., Piekarczyk A., *Diagnostyka konstrukcji żelbetowych. T.1, Metodologia, badania polowe, badania laboratoryjne betonu i stali*. Wydawnictwo Naukowe PWN, Warszawa 2010.
- [24] Lackner R., Mang H.A., “Scale Transition in Steel-Concrete Interaction. I: Model”, *Journal of Engineering Mechanics*, 2003, vol. 129, no. 4, pp. 393-402. [https://doi.org/10.1061/\(ASCE\)0733-9399\(2003\)129:4\(393\)](https://doi.org/10.1061/(ASCE)0733-9399(2003)129:4(393))
- [25] Lackner R., Mang H.A., “Scale Transition in Steel-Concrete Interaction. II: Applications”, *Journal of Engineering Mechanics*, 2003, vol. 129, no. 4, pp. 403-413. [https://doi.org/10.1061/\(ASCE\)0733-9399\(2003\)129:4\(403\)](https://doi.org/10.1061/(ASCE)0733-9399(2003)129:4(403))
- [26] Ngo D., Scordelis A., “Finite element analysis of reinforced concrete beams”, *ACI Journal*, 1967, vol. 64, no. 3, pp. 152-163.
- [27] Hameed R., Sellier A., Turatsinze A., Duprat F., “Simplified approach to model steel rebar-concrete interface in reinforced concrete”, *KSCE Journal of Civil Engineering*, 2017, vol. 21, no. 4, pp.1291-1298. <https://doi.org/10.1007/s12205-016-1397-1>
- [28] Ueda T., Sato Y., Tadokoro T., “Prediction of Tension Behavior of Reinforced Concrete Members with Bond Model”, in *Bond in Concrete – from research to standards*. Budapest, 2002, pp. 293-299.
- [29] Suchorzewski J., Korol E., Tejchman J., Mroz Z., “Experimental study of shear strength and failure mechanisms in RC beams scaled along height or length”, *Engineering Structures*, 2018, vol. 157, pp. 203-223. <https://doi.org/10.1016/j.engstruct.2017.12.003>
- [30] Suchorzewski J., Marzec I., Korol E., Tejchman J., “Investigations on strength and fracture in RC beams scaled along height or length, Meschke G., Pichler B., Rots J.G.”, in *Conference on Computational Modelling of Concrete and Concrete Structures (EURO-C)*. Bad Hofgastein 2018, pp. 651-661. <https://doi.org/10.1201/9781315182964>
- [31] Den Uijl J.A., Bigaj, A.J., “A bond model for ribbed bars based on concrete confinement”, *Heron*, 1996, vol. 41, no. 3, pp. 201-226.


Studies on the effects of superficial strengthening with FRCC system on compressive strength of AAC masonry

Lukasz Drobiec¹, Wojciech Mazur², Remigiusz Jokiel³

¹ Department of Building Structures; Faculty of Civil Engineering; Silesian University of Technology; Akademicka 2 St., 44-100 Gliwice, Poland;

lukasz.drobiec@polsl.pl  0000-0001-9825-6343

² Department of Building Structures; Faculty of Civil Engineering; Silesian University of Technology; Niedobczycka 2 St., 44-100 Gliwice, Poland;

wojciech.mazur@polsl.pl  0000-0001-6382-1496

³ BUDINŻ PB Sp. z o.o. Sp.k.; Niedobczycka 2 St., 44-290 Jejkowice, Poland; remigiusz.jokiel@gmail.com

Abstract: This paper describes results from studies on the effects of superficial strengthening with FRCC system on compressive strength of autoclaved aerated concrete (AAC) masonry. Tests were carried out on models without any strengthening, strengthened at one or both sides. Two-side strengthened masonry demonstrated an increased compressive strength and deformability. Increased deformability was observed for one-side strengthened masonry when compared to tests on masonry without any strengthening.

Keywords: AAC blocks, compressive strength, FRCC system, superficial strengthening

1. Introduction

Repairs of cracked masonry walls are increasingly made using superficial strengthening [1] especially FRCC [2]–[5]. This repair system consists of high-performance mortar from cement binders and various additives, and grid made of carbon, glass, basalt, aramid, or other fibres. Factory-made mortar is physically and chemically compatible with the wall, especially the brick wall. There are no design guidelines consistent with Eurocodes. Thus, material tests must be performed in accordance with European standards, to develop suitable guidelines verified on big models under complex stress states.

It is apparent that the most effective use of superficial strengthening is observed for tensile forces which can be successfully verified by conducting tests on tensile strength of the wall by subjecting it to diagonal compression in accordance with the standard [6]. Such tests on evaluating the effects of superficial strengthening on tensile strength of AAC walls under diagonal compression have been already performed in the laboratory of the Faculty of Civil Engineering at the Silesian University of Technology [7]–[9]. However, it is important that

not only vertical compressive stresses occur under axial compression, but horizontal tensile stresses are observed as well.

Currently, new tests are performed to determine the effect of superficial strengthening with FRCM system on compressive strength of AAC masonry with one-side and two-side strengthening. The research programme includes tests on compressive strength of masonry walls in accordance with the standard [10], their tensile strength under compression by the standard [6] and their shear strength [11]. Additionally, tests are planned to evaluate the effect of superficial strengthening on compressive strength of walls with a vertical crack and strengthened in four sides, and walls with additional mechanical anchorage of superficial strengthening.

2. Research tests

2.1. Aim and scope of tests

The aim of tests described in this paper was to determine the effects of superficial strengthening with FRCM system on compressive strength of AAC masonry. Observation of behaviour, cracking pattern and failure of test elements was the intermediate purpose of the tests. The scope of performed tests included masonry walls without any strengthening, strengthened at one side or both sides. Compressive strength of the masonry was performed in accordance with [10] PN-EN 1052-1.

2.2. Research models

The masonry was made of SOLBET OPTIMAL blocks with dimensions $l \times t \times h = 590 \times 180 \times 240$ mm, density class of 600 and normalized compressive stress f_b equal to 4.0 N/mm^2 [12]. White cement-based mortar for thin joints from SOLBET company – identified by the symbol 0.1, nominal class M5, compressive strength f_m equal to 6.1 N/mm^2 [12] was used in test models.

Dimensions of test specimens were determined in accordance with [10]. The width of test specimens was equal to two masonry units, and their height corresponded to 5 masonry units. Dimensions of test specimens are shown in Fig. 1a. Figure 1b illustrates some tested units.

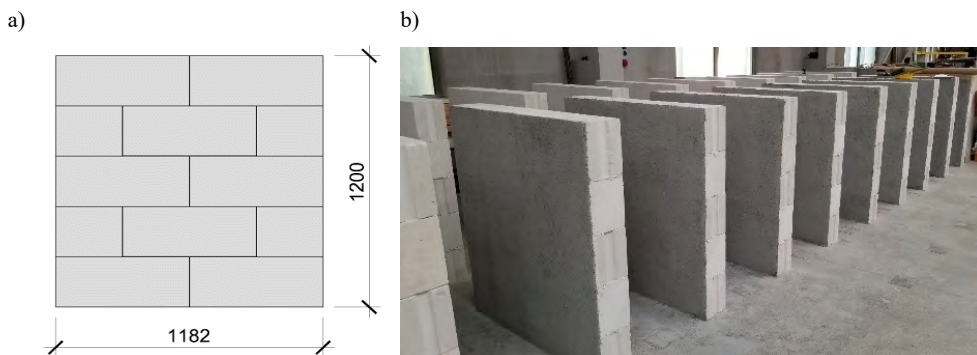


Fig. 1. Test specimens: a) arrangement of masonry units in the research model and its dimensions, b) strengthened test specimens of S1F1 and S1F2 series. *Source:* own study

Test specimens were prepared on the flat surface of the strong floor in the Laboratory of the Civil Engineering Faculty, Silesian University of Technology, built on a thin sand bed. After applying a course of masonry units, bed surfaces were smoothed with planes to level minor irregularities of the surface, and then cleaned with a brush. Mortar was placed only on the bed surface with a special trowel 180 mm wide (head joints were unfilled). Test specimens were covered with 0.2 mm thick PE foil for the first three days to protect them against excessive drying. After that time, test specimens were stored under dry air conditions in the laboratory, at temperature $\geq 15^\circ$ and humidity $\leq 65\%$ until they were subjected to tests.

After 28 days, lateral surfaces of strengthened models were coated with ready-mixed mortar PBO-MX GOLD MURATURA, and the grid PBO-MESH GOLD 70/18 was laid in it. Then, the surface layer of ready-mixed mortar PBO-MX GOLD MURATURA was placed.

The testing programme involved 18 test models (Table 1). The first series included six reference models marked as S1N. The second series marked as N1F1 included six models strengthened on one side, and the one marked as S1NF2 embraced other six models strengthened on both sides.

Table 1. Marking of test series. *Source:* own study

Series	Number of test specimens
S1N Unstrengthened test specimens	6
S1F1 One-side strengthened test specimens	6
S1F2 Two-side strengthened test specimens	6
TOTAL	18

2.3. Testing technique

Tests were performed on test specimens after at least 28 days from finishing works. Tests were conducted in a hydraulic press with the compressive force of 200 T. Test specimens were placed between platens of the hydraulic press, in the central position, without providing eccentricity. There was a full contact between the top and bottom surface of test specimens and platens of the universal testing machine.

During tests, a dynamometer measured compressive force with the accuracy of 0.001 kN, and inductive sensors measured horizontal and vertical displacements with the accuracy of 0.002 mm. Additionally, displacements were measured with a non-contact optical system Aramis. For that purpose, surfaces of test specimens required painting in irregular designs and sticking points of measurements on the lateral surface of the test specimen. Dimensions of a measurement reference base for wall displacement were specified in accordance with [10]. That standard defines the base height equal to 1/3 of the test specimen height and the width equal to 1/2 of the test specimen width. For the arrangement of test specimens shown in Fig. 1, 1/2 of its length is located on vertical joints. Previous experience of the authors showed that such a system could disturb the measurements.

Therefore, a decision was made to expand the horizontal base by 20 mm with reference to the base specified in the standard. The measurement reference base and the inductive sensor are illustrated in Fig. 2.

Vertical strains were measured to determine vertical stress σ_y – vertical strain ε_y relationship. And horizontal strains were used to determine Poisson's ratio ν of the masonry.

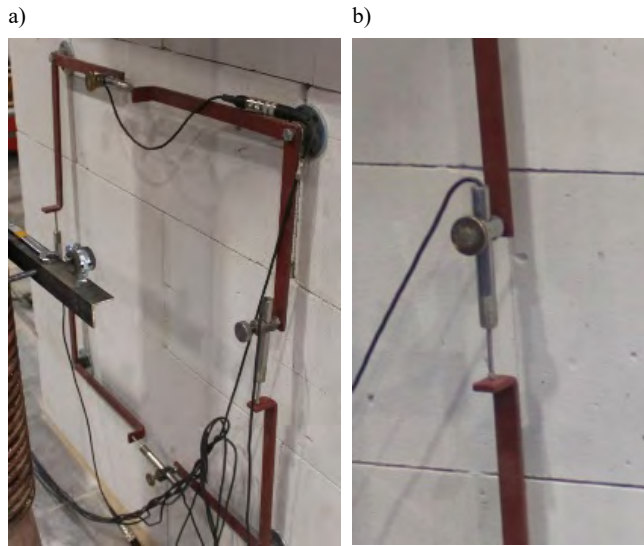


Fig. 2. The reference base for measuring displacement: a) view of the steel frame, b) inductive sensor. *Source: own study*

Prior to tests, each test specimen was carefully inspected for any possible damage. Then, each test specimen was measured with an accuracy to ± 1 mm. All outer edges of test specimens were measured. Figure 3 presents one test specimen from each series in the test stand prior to tests. Photos illustrate frames for measuring displacements and irregular painting pattern for tactile measurement.

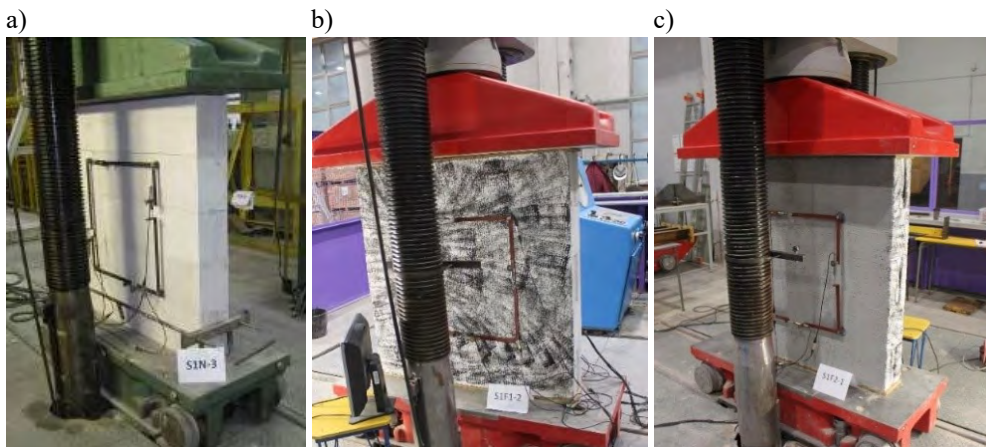


Fig. 3. Test specimens of each series prior to tests. *Source: own study*

Tests were conducted using an automated measuring stand. Displacements and compressive force were measured every 0.5 s. The loading rate was applied in accordance with [10] to achieve the maximum force after 15-30 minutes from the commencement of loading. The force, at which the first visible crack occurred in the test specimen, was also recorded during tests.

3. Test results

To determine values of cracking and failure stress, the force was divided by the measured cross-section area of the test specimen. Modulus of elasticity and Poisson's ratio were determined as a secant from the average value of deformations measured with sensors at stress equal to 1/3 of maximum stress.

Table 2 presents values of stress, at which cracks were observed in test specimens, compressive strength, modulus of elasticity, and Poisson's ratio.

Table 2. Averaged test results for each series. *Source:* own study

No. of series		Cracking stress, N/mm ²	Maximum stress, N/mm ²	Modulus of elasticity, N/mm ²	Poisson's ratio
Unstrengthened test specimens	S1N-1	2.35	2.95	1799	0.15
	S1N-2	2.40	2.58	1766	0.19
	S1N-3	2.28	2.86	2143	0.19
	S1N-4	2.25	2.56	2106	0.20
	S1N-5	2.42	3.58	2346	0.20
	S1N-6	2.40	3.29	2083	0.14
	Mean value	2.35	2.97	2041	0.18
	Standard deviation	0.07	0.40	221	0.03
	Coefficient of variation	3%	14%	11%	15%
One-side strengthened test specimens	S1F1-1	2.45	2.74	2105	0.41
	S1F1-2	2.70	3.09	2218	0.38
	S1F1-3	2.50	2.79	1955	0.28
	S1F1-4	2.75	3.08	2125	0.42
	S1F1-5	2.80	3.15	1995	0.37
	S1F1-6	2.50	2.89	2269	0.46
	Mean value	2.62	2.96	2111	0.39
	Standard deviation	0.15	0.17	122	0.06
	Coefficient of variation	6%	6%	6%	16%
Two-side strengthened test specimens	S2F1-1	2.75	3.13	2254	0.35
	S2F1-2	2.70	3.09	2265	0.38
	S2F1-3	2.85	3.36	2410	0.33
	S2F1-4	2.65	2.94	2257	0.46
	S2F1-5	2.75	3.15	1993	0.37
	S2F1-6	2.75	3.18	2144	0.23
	Mean value	2.74	3.14	2221	0.35
	Standard deviation	0.07	0.14	140	0.08
	Coefficient of variation	2%	4%	6%	21%

The course of failure was various for test specimens. In most test specimens, first cracks were observed before the failure of those test specimens (see Table 2). Cracks ran through

joints and masonry units. Loosening of face parts of the masonry was also observed. Figures 4÷6 present all lateral faces of destroyed elements.

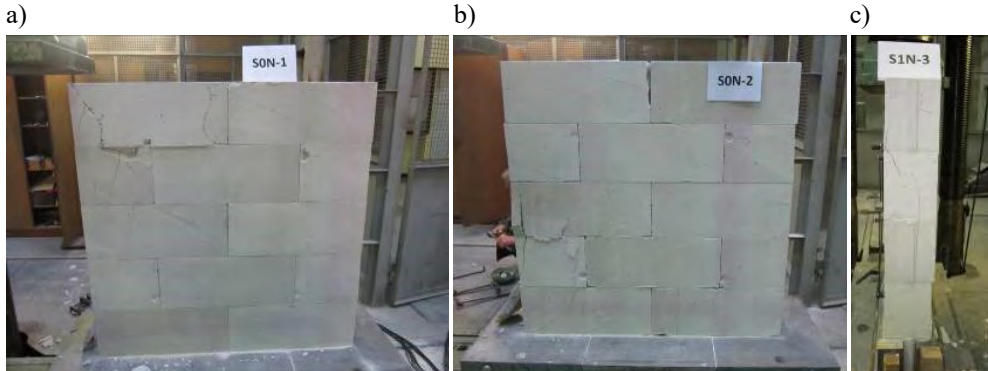


Fig. 4. Test specimens S1N after tests: a) S1N-1, b) S1N-2, c) S1N-3. *Source: own study*

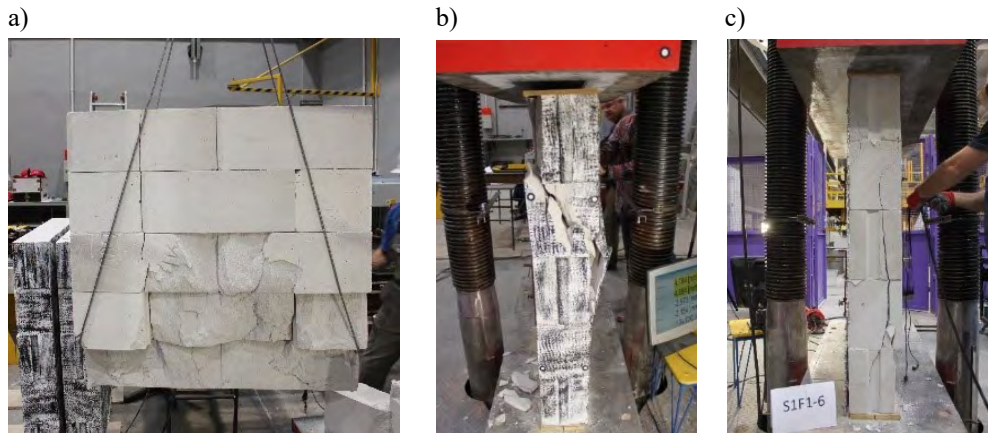


Fig. 5. Test specimens S1F1 after tests: a) S1F1-1, b) S1F1-5, c) S1F1-6. *Source: own study*

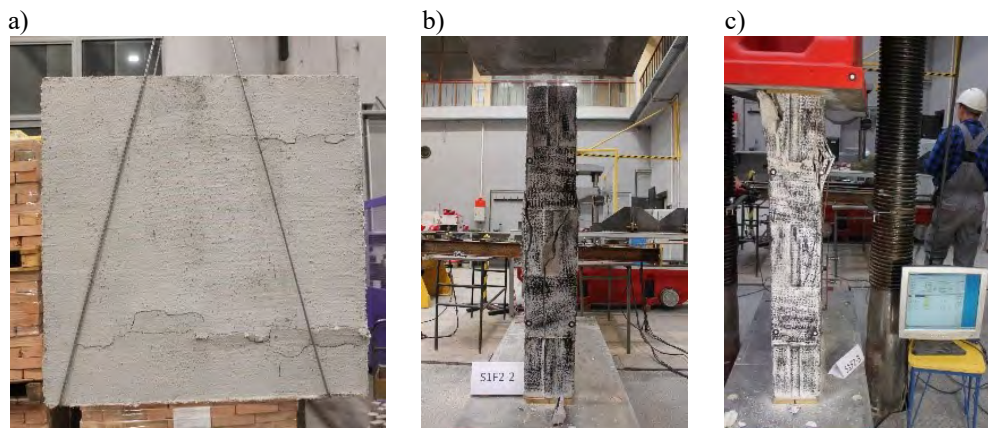


Fig. 6. Test specimens S1F2 after tests: a) S1F2-1, b) S1F2-2, c) S1F2-3. *Source: own study*

Figure 7 shows the comparison of stress σ_y – vertical deformation ε_y and horizontal deformation ε_x , relationships averaged for each series. Letter y in the description of diagrams in Fig. 7 denotes the vertical direction measurements, and the letter x denotes the horizontal one.

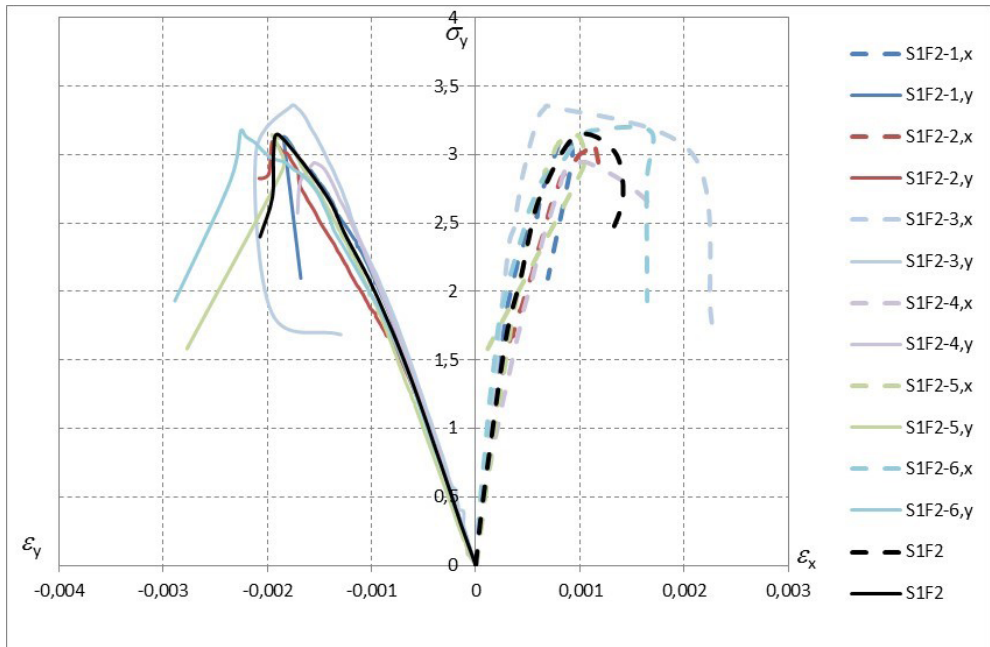


Fig. 7. Stress σ_y – vertical strain ε_y and vertical strain ε_x relationships averaged for each series. *Source:* own study

3.1. Characteristic compressive strength of masonry acc. to [10] PN-EN 1052-1

Characteristic compressive strength of masonry was determined within each series. That procedure was performed in accordance with [10] PN-EN 1052-1. The standard assumes that characteristic compressive strength of the masonry is a lower value of the averaged strength for a series divided by 1.2 or the minimum strength from a given series:

$$f_k = \min \begin{cases} \frac{f}{1.2} \\ f_{i,\min} \end{cases} \quad (1)$$

where:

f – average compressive strength of the masonry for a given series (Table 2, Column 4);

$f_{i,\min}$ – minimum compressive strength of a test specimen from a given series (Table 2, Column 4).

Determined values of characteristic compressive strength for each series are presented in Table 3. First condition of Equation 1 was crucial for each series which shows a great homogeneity of tested walls.

Table 3. Characteristic compressive strength of masonry acc to [10]. *Source:* own study

No. of series	$f_{k, test}$ N/mm ²
S1N Unstrengthened test specimens	2.48
S1F1 One-side strengthened test specimens	2.47
S1F2 Two-side strengthened test specimens	2.62

3.2. Characteristic compressive strength of masonry acc. to [13] PN-EN 1990

Characteristic compressive strength of masonry was determined within each series. That procedure was performed in accordance with [13] PN-EN 1990. Determined values of characteristic compressive strength for each series are presented in Table 4.

Table 4. Characteristic compressive strength of masonry acc to [13]. *Source:* own study

No. of series	$f_{k, test}$ N/mm ²
S1N Unstrengthened test specimens	2.20
S1F1 One-side strengthened test specimens	2.29
S1F2 Two-side strengthened test specimens	2.60

4. Analysis of test results

First cracks in test specimens of S1N series (unstrengthened) were observed at stress of 2.35 N/mm² which represented ca. 79.1% of maximum failure stress equal to 2.97 N/mm². Test specimens were cracked and destroyed due to internal cracks.

In test specimens of S1F1 series (one-side strengthened), first cracks developed at stress equal to 2.62 N/mm² which represented 88.5% of maximum failure stress (2.96 N/mm²). Cracking stresses were greater by 10.3% compared to unstrengthened test specimens. Failure stresses were nearly the same.

Recorded cracking stress for test specimens of S1F2 series (two-side strengthened) was 2.74 N/mm², which represented 87.3% of failure stress (3.14 N/mm²) and was greater by 14.2% and 4.4% compared to values for S1N and S1F1 series respectively. Failure stress of two-side strengthened test specimens was greater by ca. 5.4% and 5.8% compared to unstrengthened and one-side strengthened test specimens, respectively.

Strengthening caused an increase in modulus of elasticity by 3.4% for one-side strengthened test specimens, and by 8.1% for two-side strengthened test specimens, and in Poisson's ratio by 53.8% and 48.6% respectively.

Characteristic compressive strength values of the walls of series S1N, S1F1, and S1F2 which were determined in accordance with the standard [10] were equal to 2.48 N/mm², 2.46 N/mm² and 2.62 N/mm² respectively. Characteristic strength of the walls strengthened in one side was lower by 1% when compared to the walls without any strengthening. In the case of the walls with two-side strengthening, their characteristic strength was greater by 6% when compared to the walls without any strengthening. Different results were obtained for character-

istic strength determined in accordance with the standard [13]. Strength values of 2.20 N/mm², 2.29 N/mm² and 2.60 N/mm² for the specimens of series S1N, S1F1, and S1F2 respectively were lower than the values determined under the standard [10] by ca. 11% for S1N, 7% for S1F1 and 1% for S1F2. Characteristic strength of the walls strengthened in one side, and two sides was greater by 4% and 18% respectively when compared to the unstrengthened walls.

No cracks on the strengthened surface were observed while analyzing results for strengthened models, measured with Aramis system based on digital image correlation. The analysis of displacement towards Z-axis, perpendicular to the strengthened surface of the masonry showed an increase in displacements in the bottom part of the test specimen which indicates the loosening of the strengthening from masonry units (Fig. 8).

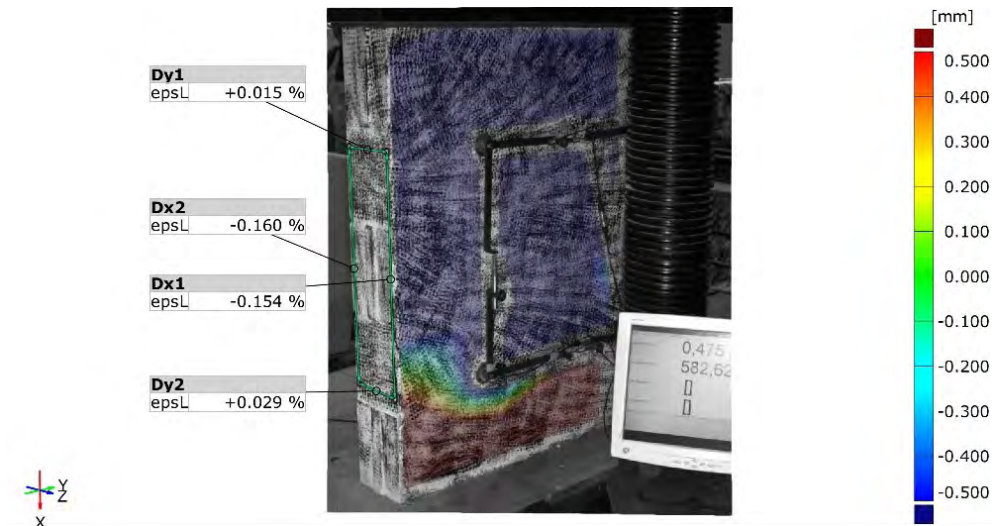


Fig. 8. Surface displacement on Z-axis in obtained from Aramis system for S1F1 1 test specimen. *Source:* own study

Inspections of damaged bottom areas of test specimens revealed failure occurred as the loosening of the strengthening with a part of masonry units.

5. Conclusions

One-side strengthening did not affect the load capacity of the masonry, and its increase by 6% was observed in the case of two-side strengthening test specimens. Characteristic compressive strength of the walls strengthened in one side was which determined in accordance with the standard [10] was lower by 1% when compared to the walls without any strengthening. In the case of the standard [13], the determined value was greater by 4% when compared to the walls without any strengthening. Characteristic strength values of the walls strengthened in two sides, determined with both methods were greater by 6% and 18% respectively for the standard [10] and [13] as compared to the unstrengthened walls. Considerable impact of the strengthening was found for cracking stresses. Crack resistance was improved by more than 10% in one-side strengthened test specimens, and by 17% in two-side strengthened test specimens. Strengthening did not significantly affect the modulus of elasticity but caused an increase in horizontal deformations of the masonry by ca. 50%. The in-depth diagnosis of the effect exerted by applied strengthening on AAC masonry requires further studies. Therefore,


the next stage of studies will include tests on one-side and two-side strengthened masonry for diagonal compression in accordance with the standard [6] and shearing in accordance with the standard [11].

References

- [1] Babaeidarabad S., Arboleda D., Loreto G., Nanni A., “Shear strengthening of unreinforced concrete masonry walls with fabric-reinforced-cementitious-matrix”, *Construction and Building Materials*, vol. 65, 2014, pp. 243-253.
- [2] Ceroni F., Salzano P., “Design provisions for FRCC systems bonded to concrete and masonry elements”, *Composites Part B: Engineering*, vol. 143, 2018, pp. 230-242. <https://doi.org/10.1016/j.compositesb.2018.01.033>
- [3] Bilotta A., Ceroni F., Nigro E., Pecce M., “Experimental tests on FRCC strengthening systems for tuff masonry elements”, *Composites Part B: Engineering*, vol. 129, 2017, pp. 251-270. <https://doi.org/10.1016/j.combuildmat.2017.01.124>
- [4] Carozzi F.G. et al., “Experimental investigation of tensile and bond properties of Carbon-FRCC composites for strengthening masonry elements”, *Composites Part B*, vol. 128, 2017, pp. 100-119.
- [5] Jokiel R., Drobiec Ł., “Projektowanie wzmocnień konstrukcji murowych systemami FRCC w świetle badań i zaleceń normowych”, *Izolacje*, vol. 3, 2019, pp. 90, 92-94.
- [6] ASTM E519-81 Standard Test Method for Diagonal Tension (Shear) of Masonry Assemblages.
- [7] Kubica J., Kałuża M., “Diagonally compressed AAC Block’s masonry – effectiveness of strengthening using CRFP and GRFP laminates”, in *Proceedings 8th International Masonry Conference, Masonry (11)*. Ed. by W. Jäger, B. Haseltine & A. Fried, Dresden 2010, pp. 419-428.
- [8] Kałuża M., Kubica J., “Behaviour of unreinforced and reinforced masonry wallettes made of ACC blocks subjected to diagonal compression”, *Technical Transactions – Civil Engineering 1-B/2013* (2013), pp. 79-94.
- [9] Kałuża M., Galman I., Kubica J., Agneloni C., “Diagonal Tensile Strength of AAC Blocks Masonry with Thin Joints Superficially Strengthened by Reinforced Using GFRP Net Plastering”, *Key Engineering Materials*, vol. 624, 2015, pp. 363-370. <https://doi.org/10.4028/www.scientific.net/KEM.624.363>
- [10] PN-EN 1052-1:2000 Methods of test for masonry – Part 1: Determination of compressive strength.
- [11] PN-EN 1052-3:2004 Methods of test for masonry – Part 3: Determination of initial shear strength.
- [12] Jasiński R., Drobiec Ł., “Study of Autoclaved Aerated Concrete Masonry Walls with Horizontal Reinforcement under Compression and Shear”, *Procedia Engineering*, vol. 161, 2016, pp. 918–924. <https://doi.org/10.1016/j.proeng.2016.08.758>
- [13] PN-EN 1990:2004 Eurocode – Basis of structural design.

Digital fabrication in the process of creation of the parametric concrete fencings

Marcin Giedrowicz

*Institute of Architecture and Spatial Planning; Poznan University of Technology,
2 Jacka Rychlewskiego Street, 61-131 Poznan, Poland;
marcin.giedrowicz@put.poznan.pl  0000-0002-3055-9222*

Abstract: This paper is a summary of the research on parametric design methods and digital fabrication in architecture and industrial design. Through the author's projects, he presents how effective parametric designing process can be in contemporary architecture. This publication is a testimony of a long and full production process of a set of concrete fencings – from design part, through prototyping, digital fabrication, post-production, concrete fabrication and selling process. The design part of this research pertains to algorithmic design methods in Grasshopper software as well as presents a broad range of various technological aspects involved in the fabrication process. In the conclusion part of this paper, the author discloses his expectations towards the future of concrete fencing in Poland and describes a set of appropriate rules that foster a further development of this technology.

Keywords: parametric design, digital fabrication, concrete fencing, prefabrication, Rhinoceros, Grasshopper, CNC, detail

1. Introduction

Nowadays, concrete is no longer a mix of volcanic dust and sand. Since the end of ancient times, concrete has undergone an extensive technological evolution and has reached an exceptional level of quality. Its mechanical characteristics allow a wide range of flexibility and versatility, while components mixed into concrete, such as glass fibre, aggregates and chemical admixtures, additionally enhance its aesthetic qualities which are increasingly appreciated by architects. The fourth industrial revolution, driven by the correlation between the Internet, CNC machines, NURBS software, 3D printers and a building site, puts concrete in a particularly strong position. In regard to the development of contemporary architecture, concrete [1] has an opportunity to become a bridge between the traditional, economic and durable building engineering and the progressive parametric architecture. Therefore, the use of concrete as an execution tool in the technological process has the potential to revolutionise the contemporary building engineering. This article is a summary of the study conducted on the use of digital

methods of fabrication, intended for the construction of precast concrete elements of fences as well as for the professional use of this technology in the process of developing a unique style.

2. Research

2.1. Current situation

Concrete fencing in Poland is continuously very popular and attracts an ever-growing interest since the 90s of the last century, providing a more affordable alternative to fences made of steel, timber and brickwork. Among many advantages of precast concrete fencing is their durability, easy and quick production, short time of the execution of a purchase order and its low price. Not without reason, concrete fences quickly became a budget substitute for the fencing commonly used in Poland which in general, directly refers in its form to its more noble archetypes. Consequently, the aesthetics of concrete fences is disputable, to say the least, and is often criticised among architects. Amidst many critical opinions aimed at them, the most important ones seem to concern the degradation of aesthetics in public areas as well as a gradual rejection of the use of traditional solutions in Polish villages. The authorities of towns and villages are also aware of these problems, which often leads to implementing the spatial regulations (Local development plan / Outline planning decision) which forbid the use of concrete fences and fence walls. Despite those regulations, concrete fences are still being built in the rural areas of Poland, revealing the ineffectiveness of the law enforcement and execution, but also the lack of proper aesthetic awareness and difficult financial situation of people living in rural areas.

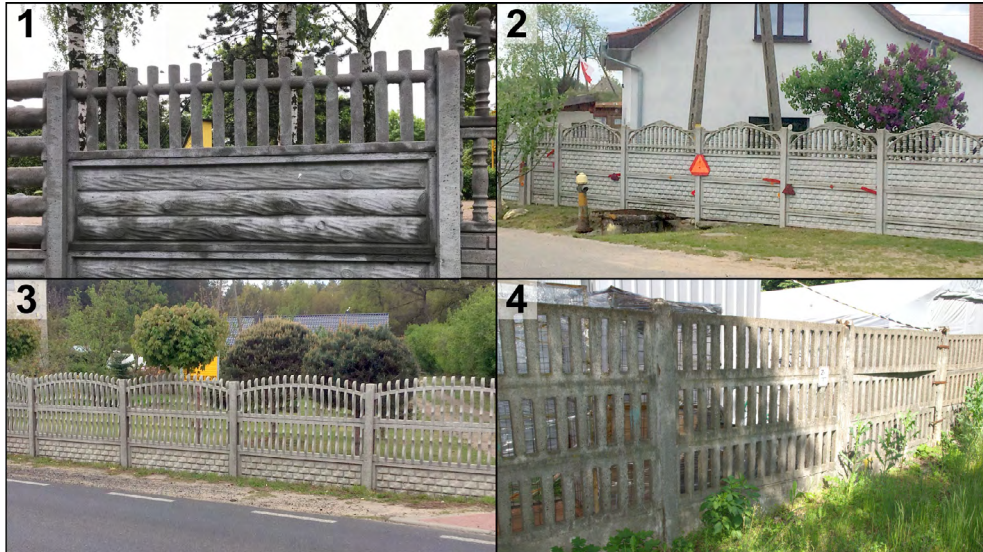


Fig. 1. Four groups of concrete fences in Poland – 1: timber imitation type in Chyby village, 2: brick imitation type in Karsko village, 3: steel imitation type in Lubianka village, 4: “socialist Poland” type in Przeclaw village. *Source:* [Marcin Giedrowicz]

Most of the concrete fences offered on the Polish market can be divided into four groups. The first one which is most frequently seen is the imitation of fences made from timber – full

of details and quotes derived from woodworking technology and the decorative folk art. The second group of designs, encountered equally often as the first one, are copies of the solutions derived from masonry – those designs are drawing on different brickwork motifs, stone walls, traditional solutions characteristic of the rural and vernacular architecture. The third group of fenceings includes imitation of the solutions typically used in the production of steel fencing – in the composition of which vertical and skew directions dominate, accented by slim elements that refer to steel bars. In this group of designs, we can equally often find framework compositions and openwork screens, falling into repeatable patterns. The fourth and the least developed group of designs are those that are deprived of direct aesthetic connections and references to traditional archetypes, constituting independent creation within the field of industrial design. These designs, having no complexes about the past, intentionally take advantage of such material as raw as concrete, creating design solutions that highlight the industrial nature of that building material. Few examples of that group of designs include the design of the railway fence developed at the times of the socialist Poland. A simple, orthogonal pattern with rhythmical, slim slots in the ABAB arrangement that had been used for many years for fencing of the railway areas, track superstructures, and farmsteads. That design has a very well-balanced proportions and ability to be connected into interesting arrangements when mixing it with a robust monolithic fencing design. However, due to its inferior quality of workmanship (use of very coarse aggregate fraction and concrete of poor quality), low durability and numerous associations with the communist period in Poland, this pattern has been perceived negatively [2].

2.2. The task

The primary research and design objective was to develop a catalogue of concrete fencing designs, which would be included in the commercial offer of the Poznań-based producer of precast concrete products.

The job entrusted was complex, which included [3]:

- expansion and development of the catalogue of concrete fencing patterns in the form of digital models,
- preparation of the fence mockups in scale 1:25 using 3D printing,
- making the fence prototypes in scale 1:1, with the assistance of CNC technology,
- making the casting moulds based on the wooden prototypes,
- implementation of concrete positives with the use of casting moulds.

The task aimed to create modern designs for concrete fences that break away from the current, negatively perceived market trends. The design of the developed collection, was supposed to be characterised by a fresh take on the material such as concrete and the most up-to-date design methods, assisted by CNC technology and parametric designing. The investor's concept was a new collection of fences to be supplied to more demanding customers, who will not only appreciate the design of the fence but will also place it in the appropriate area. This conceptual thinking that concerns new designs was based on the idea that the new product should find its place only in the urban or suburban areas, where it would complement the modern architecture.

2.3. Methods

The first stage of the design process consisted of creating an extensive collection of fence designs, according to the investor's guidelines, relating to technological limitations and costs of production.

- in the topology, using a pattern of right, obtuse and negative angles,
- using too small openings (not possible to be precisely cast from concrete).

In the result of the analysis carried out, five fencing designs were singled out with the following trade names:

NEO PRL – single-element design that is the modern interpretation of the railway fencing from the era of socialist Poland;

STRIPE – simple, minimalistic, single-element design with horizontal stripes, easily adaptable to the contemporary residential and service housing;

ATTRACTOR [4] – a complicated four-component design developed in the Grasshopper program, using the “Attractor” type algorithm;

WAVE – two-element design developed in the Grasshopper program, using the “Tween Curve” type algorithm;

LARSSEN – simple, minimalistic, single-element design with vertical stripes, inspired by Larssen steel profiles. These fences can create three different patterns by the use of just one single element.

The second stage of the work consisted of precise development of the geometry of individual fences, and then producing their trial mockups in scale 1:25 – for this purpose 3D printing technology was applied, in type FDM and the Zortrax M200 printer. The produced patterns did not prompt any fears or objections of the investor, who permitted to continue the work.

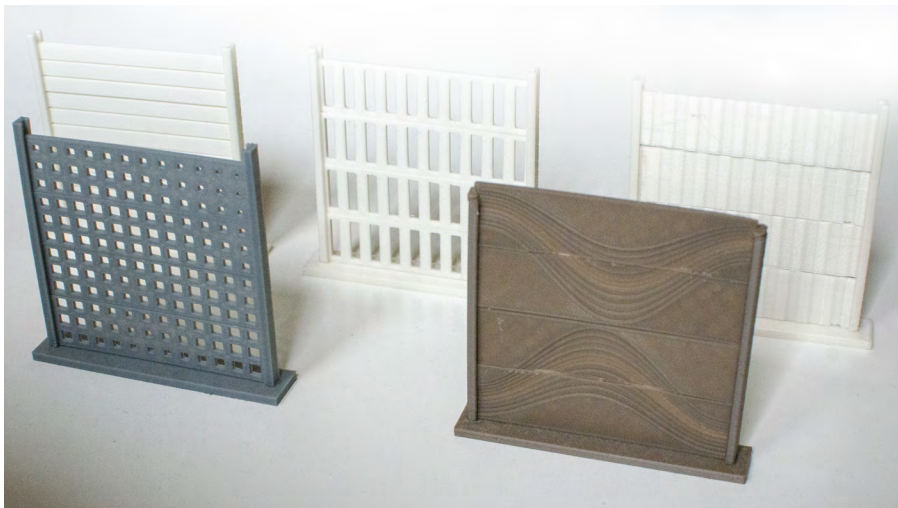


Fig. 3. Concrete fencing plastic models – effect of 3D printing process. First row from left: “ATTRACTOR” and “WAVE”. Second row from left: “STRIPE”, “NEO PRL” and “LARSSEN”. Source: [Marcin Giedrowicz]

The third and the most complicated stage of the work was the production of fence prototypes – it was decided that a subtractive fabrication and wood-like material in the form of MDF boards would be used. The produced prototype fences were intended to serve at the later stage of the process as the positives to produce casting moulds from fibreglass and steel. The first two fence designs (NEO PRL and STRIPE) did not cause any significant technological problems – they were produced by means of the two and a half axis CNC mill planer. In both

cases the double MDF board was used, with dimensions of 200x50x2.2, placed one upon the other and integrated with wood screws. The entire working path of the mill was developed sequentially in Rhinoceros / Grasshopper, CorelDraw and ArtCAM programs. The ATTRACTOR [5] design of the fence, generated in the Grasshopper program consisted of as many as 4 individual elements with dimensions of 200x50x4.4, which together contained in itself 124 unique openings [6]. The next significant technological limitation was a relatively small size of the openings – causing the wet concrete in the casting mould to turn into both, narrow and longitudinal shape. In consequence, a small mass of concrete placed in the narrow space could not be removed from the mould undamaged. This issue was solved by making holes; the angle of inclination of their internal wall was within the span of 80 to 85 degrees. Despite many attempts and many ideas of how to make cuts at such a small inclination angle and the 2,5-axis mill, it appeared to be impossible, or too time-consuming. In result, the decision was made to engage the 6-axis KUKA KR 60 HA robot arm, controlled by the library of Grasshopper – KUKA prc v2 program. The robot performed 124 openings in 4 subsequent stages of work – the MDF boards were mounted onto the provisional bench using clamps.



Fig. 4. 6-axis KUKA KR 60 HA robot arm during the milling process. *Source:* [Marcin Giedrowicz]



Fig. 5. The “Attractor” fencings realisation at the construction site. *Source:* [Marcin Giedrowicz]

The fourth two-element “WAVE” [7] design was made using the 2.5 axis mill – even though the operation also required cutting out of internal walls with the inclination angle not smaller than 80 degrees. However, specific topology of that design enabled correct cutting to be made using two milling cutter types – the first cut using the flat mill and the second cut using the angular mill with the cutting plane equal to 45 degrees.

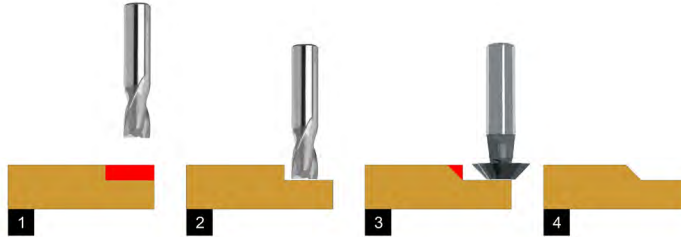


Fig. 6. The “Wave” subtractive digital fabrication process scheme. A standard flat drill conducted the first part of milling. Second part of milling required 45-degree drill. *Source:* [Marcin Giedrowicz]



Fig. 7. The “WAVE” wooden positive just after the CNC milling process. *Source:* [Marcin Giedrowicz]

The same technology with drill changing was used to fabricate the last type of precast, which name is “LARSEN”.

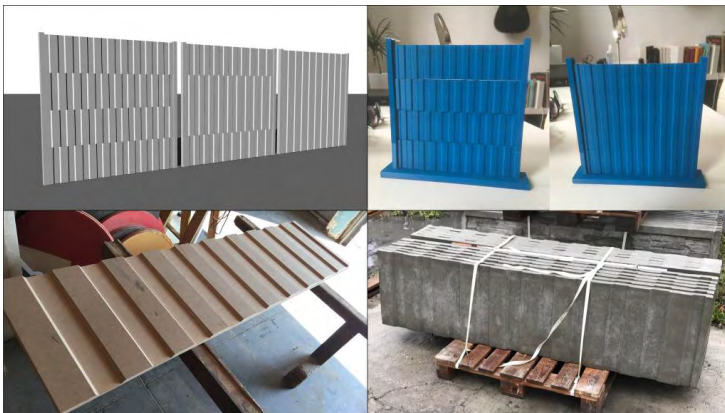


Fig. 8. The “Larsen” fenceing development process – from the 3D model and plastic mockup, to positive wooden model and final product. *Source:* [Marcin Giedrowicz]

The last stage of work was to create pouring moulds using the produced positives – the moulds were made from steel bearings equipped with four handles, filled with the impression made from fibreglass.

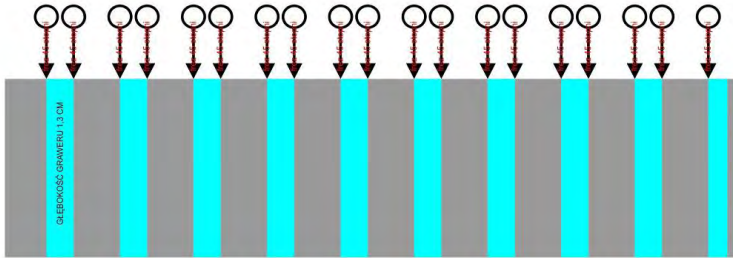


Fig. 9. 2D CorelDraw file with instructions to a CNC milling machine [8] how to create “Larsen” precast by a subtractive digital fabrication process. *Source:* [Marcin Giedrowicz]



Fig. 10. Fibreglass mould [9] of “Wave” – a negative form before concrete filling process. *Source:* [Marcin Giedrowicz]

2.4. Results

The developed casting moulds were supplied to the investor who implemented them in the production line. In order to facilitate the separation of concrete from mould, the moulds were covered with an oily substance before filling them with C30. The process of mould filling and concrete surface levelling on the vibration table took about 60 seconds for a single element. After that time, the solidifying concrete element was separated from its mould and transferred to the drying area – the process of independent drying takes about 24 hours. In consequence, the trial castings of all the developed fence designs were produced to the satisfaction of the investor. The obtained moulds had no errors or geometric deformations. Shortly after that, mass production of the developed designs was started, where current statistics demonstrate very high sales of the “STRIPE” design, moderate sales of the “LARSSEN”, “ATTRACTOR” and “WAVE” designs, and low sales of “NEO PRL” design.



Fig. 11. Finished products – from left side: “Stripe”, “Attractor”, “Neo PRL”. Source: [Marcin Giedrowicz]

3. Conclusions

At present, the fencing market requires a revision of the current standards, adjusting the offer to the expectations of the more demanding customer and the higher aesthetic values. Concrete fencing can constitute an excellent addition to the contemporary urban and suburban architecture – however, under a few conditions, which include:

- use of concrete designs that do not imitate any other material or style,
- conscious application of CNC technology in order to develop precise and economical designs,
- treating concrete as an inspiring material, beautiful in itself,
- seeking for modern solutions, driven by technological progress [10].

Besides, the author represents the opinion that the ban on using concrete fenceings in rural areas should be maintained, while demanding that traditional solutions are applied.


References


- [1] Akos G., Parsons R., *Foundations. The Grasshopper Primer Third Edition*, digital publication, 2014, https://modelab.gitbooks.io/grasshopper-primer/appendix/A-3/0_about-this-primer.html.
- [2] Asanowicz A., “Parametric Design – Tool, Medium or New Paradigm?”, eCAADe 2017 SHoCK!, Volume 2, Edited by Antonio Fioravanti, Stefano Cursi, Salma Elahmar, Silvia Gargaro Gianluigi Loffreda, Gabriele Novembri and Armando Trento, 2019 Roma, pp. 379-386.
- [3] Bonenberg W., Giedrowicz M., Radziszewski K., *Współczesne projektowanie parametryczne w architekturze*. Wydawnictwo Politechniki Poznańskiej, Poznań 2019.
- [4] Cichocka J., Globa A., *Attractors in architecture: attractor-based optimisation and design solutions for dynamical systems in architecture*. Code of Space, 2016. <http://hdl.handle.net/10536/DRO/DU:30090743>
- [5] Helenowska-Peschke M., *Parametryczno-algorytmiczne projektowanie architektury*. Wydawnictwo Politechniki Gdańskiej, Gdańsk 2014.
- [6] Januszkiewicz K., Giedrowicz M., “Concrete as component of the non-linear shaped structural “skin” in current architecture”, in *8th International Conference AMCM 2014 Analytical Models and New Concepts in Concrete and Masonry Structures*, Wrocław 2014.
- [7] Kozina I., *Polski Design*. Wydawnictwo SBM, Warszawa 2015.

- [8] Natividade V., “Digital Design and Fabrication of Freeform Concrete Blocks”, in *Computing for a better tomorrow*. Łódź 2018, vol. 1, pp. 743-752.
- [9] Paixao J., Fend F., “Break It Till You Make It”, in *Computing for a better tomorrow*. Łódź 2018, vol. 1, pp. 753-762.
- [10] Tedeschi A., *AAD Algorithms-aided Design: Parametric Strategies Using Grasshopper*. Le Penseur Publisher, Brienza 2014.

Effect of load level of corner columns on punching shear resistance of flat slabs

Michał Goldyn¹, Tadeusz Urban²

¹ Department of Concrete Structures; Faculty of Civil Engineering, Architecture and Environmental Engineering; Lodz University of Technology, 6 Politechniki Avenue, 90-924 Łódź, Poland; michal.goldyn@p.lodz.pl  0000-0002-7791-1940

² Department of Concrete Structures; Faculty of Civil Engineering, Architecture and Environmental Engineering; Lodz University of Technology, 6 Politechniki Avenue, 90-924 Łódź, Poland; tadeusz.urban@p.lodz.pl  0000-0001-7494-3747

Abstract: The problem related to the effect of the corner column load on the punching shear resistance of the slab was presented. Existing experimental studies on internal columns demonstrated that the column pressure could lead to an increase in the punching shear resistance. Because of different confinement conditions of corner column-slab connection joints, it is unclear if such an effect exists for corner columns. New experimental investigations were initiated to clarify this issue. They covered a total of three corner column-slab connection specimens – slabs with a thickness of 140 mm and a longitudinal reinforcement ratio $\rho_1 = 1.09\%$ connected with columns of a cross-section of 200×200 mm. The only variable parameter was the column load equal to 500, 1000 and 1500 kN.

A reduction of the slab load-carrying capacity of about 9% due to a three-fold increase in the column load was noted. Therefore, the effect of the column load turned out to be opposite to that observed for most previous tests on internal column-slab connections, which could have a result of a limited capacity of the slab reinforcement due to additional tensile forces from the lateral expansion of joint concrete.

Comparison in the light of test results demonstrated, that EN 1992-1-1 procedure allowed for safe, yet conservative estimation of the punching shear resistance. An average ratio of experimental to theoretical load of 1.82 was obtained.

Keywords: column-slab connections, punching shear, lateral expansion, membrane action, normal stress

1. Introduction

Column-slab structural systems owe their popularity to the freedom they give by arranging the space inside buildings. They also do not impose limitations on the usable height of the story,

as is the case of slab-beam ceilings. A crucial area in column-slab systems is usually a support zone in which the slab, due to the concentration of internal forces, is exposed to failure due to punching. In real structures, the effects acting within support zones result not only from the load applied on the floor slab but also from the transmission of forces between the columns of subsequent floors. Therefore, the interaction of both raises a justified question about the effect on the load carrying capacity of columns and slabs of multi-storey buildings.

For economic reasons, as a rule, different classes of concrete for slabs and columns are used. Due to the different nature of the load, columns are usually made from concrete of a higher strength. The problem of load-carrying capacity of reinforced concrete columns intersected by weaker concrete slabs was the subject of relatively few works. Previous experimental investigations conducted at the Department of Concrete Structures of the Lodz University of Technology (including [1], [2]), regarding the connection of high-strength concrete columns with ordinary or lightweight aggregate concrete slabs demonstrated a significant effect of the intersection on the ultimate columns loads. The destructive forces turned out, however higher than the theoretical load-carrying capacities resulting from uniaxial compressive strength of slab concrete. This was a consequence of the limitation of lateral expansion of joint concrete by the surrounding slab (confining action), what resulted in an increase in the effective strength of slab concrete by up to 200÷300% compared to the uniaxial compressive strength. It should be emphasized that the beneficial effect of the confining action was also observed in the case of the external joints (edge and corner). Similar conclusions resulted from studies of Guidotti et al. [3], regarding internal column-slab connection joints. Depending on the slab longitudinal reinforcement ratio, the effective strength of the joint concrete was over 70÷180% higher than uniaxial one.

However, considering column-slab connections, the effect of column pressure on the load-carrying capacity of the slab cannot be ignored. On the one hand, lateral expansion of joint concrete leads to the formation of normal (compressive) stresses in the cross-section of the slab. On the other hand, it causes additional tensile forces in the longitudinal reinforcement, which yield at a lower load level. The effect of the internal column pressure on the load capacity of the slab is schematically shown in Fig. 1, including suggestions of Muttoni et al. [4].

If the load capacity of the slab is dependent on punching mechanism, then the column pressure N_{Ed} , inducing stress σ_c exceeding uniaxial compressive strength f_{cd} , results in lateral expansion of joint concrete and corresponding lateral stress σ_2 . As a result of these deformations, compressive stress σ_{cp} appears in the slab. An increase in normal stress leads to an increase in the punching shear resistance $V_{Rd,c}(N_{Ed})$ as is observed in case of post-tensioned slabs, which was proved by research, among others [5], [6].

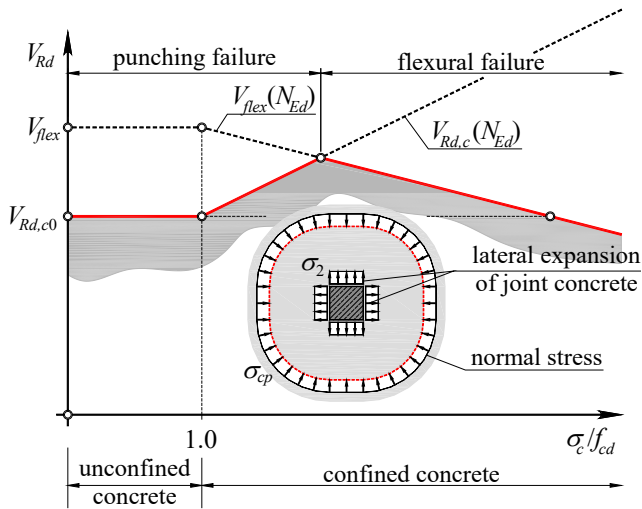


Fig. 1. Effect of column pressure on ultimate slab load. *Source:* own study

However, due to the lateral expansion of joint concrete in the longitudinal slab reinforcement, additional tensile forces arise. If column loads N_{Ed} generates stress exceeding uniaxial compressive strength of the slab concrete ($\sigma_c > f_{cd}$), then limited flexural resistance $V_{flex}(N_{Ed})$ should be expected. Depending on the intensity of the reinforcement as well as the σ_c/f_{cd} ratio, it may turn out that the flexural mechanism is decisive and the column pressure reduces the resistance of the slab due to the significant limitation of the load-carrying capacity of longitudinal reinforcement.

The issue of the interaction of column and slab load on the punching shear resistance has been so far considered only in works [3], [4]. Tests on the specimens made in real scale, characterized by longitudinal reinforcement ratios, equal to approximately $\rho_l = 0.80 \div 1.60\%$, demonstrated an increase in punching shear resistance reaching even over 30%. This effect was dependent mainly from the ratio of stress within the column base to the uniaxial compressive strength of slab concrete. It was also found that lateral expansion of joint concrete contributed to the decrease in flexural capacity due to the increase in strains of longitudinal reinforcement, which was manifested by a significant increase in slab rotation ψ (representing deflections). In the case of one of the specimens, the failure was a consequence of the flexural mechanism. However, the stress at the column base was almost three times the uniaxial compressive strength of slab concrete.

While in the case of internal connections a favourable effect of column pressure on the punching shear resistance, similar to the effect of a membrane action, can be expected, a justified question arises about external connection joints. The slab surrounds edge or corner column only from 2 or 3 sides. As a result, joint concrete is less confined, which makes it impossible to induce normal compressive stress σ_{cp} as high as in case of internal columns. Despite the great practical significance, this issue has not yet been fully explained, which was the premise for undertaking the experimental investigations at the Department of Concrete Structures of the Lodz University of Technology.

2. Experimental investigations

2.1. Test specimens

The tests included a total of three identical models – see Fig. 2. A 140 mm thick slab was connected with a column of 200×200 mm rectangular cross-section and a total height of 1340 mm. The main reinforcement of the slab consisted in ribbed bars $\phi 10$ at 60 mm in both directions (mean longitudinal reinforcement ratio $\rho_1 = 1.09\%$). The anchorage was carried out from the free edge using a loop. The other end of the bar was anchored by welding with perpendicular reinforcement. The nominal cover of the reinforcement resulted from the bond conditions and was $c_{\text{nom}} = 10$ mm, which allowed to obtain the average effective depth $d = 120$ mm. No punching shear reinforcement was placed in the slabs. Longitudinal reinforcement of the column consisted of 4 bars $\phi 20$ and stirrups $\phi 8$ at nominal spacing every 100 mm, reduced to 50 mm at both ends of the column.

The models were intended to reflect column-slab connections corresponding to real structures. Therefore, they were made in three stages, consisting of casting the bottom column at the beginning, then the slab and the top column at the end. Two different concrete mixes were used. The columns were made of a concrete mix produced on-site with the designed compressive strength class C40/50, while slabs of ready-mixed concrete with the designed compressive strength class C25/30. At a given stage, individual parts of the specimens (columns and slabs) were made of concrete from a single batch.

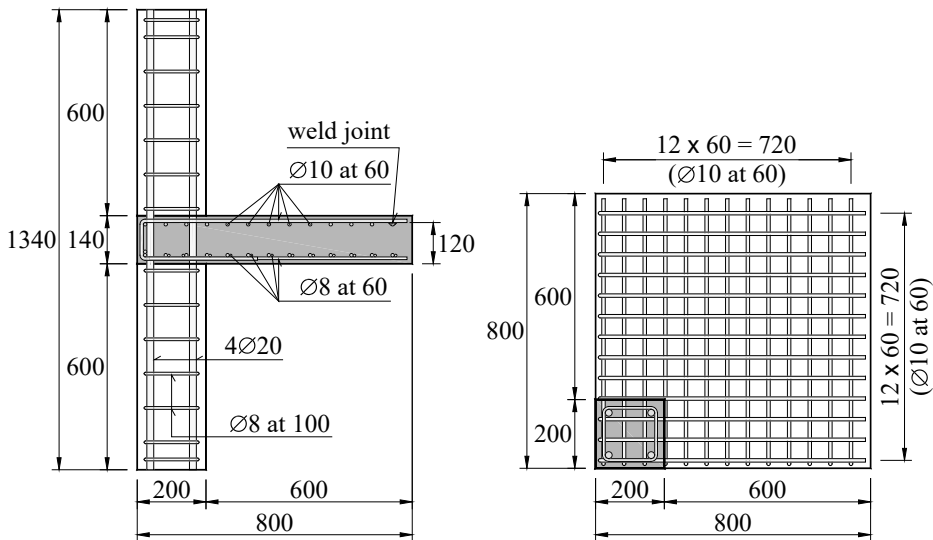


Fig. 2. View of the reinforcement of the test specimens. *Source:* own study

Concrete properties were determined at the day of testing of main specimens. Due to the long time that elapsed from a casting of the elements no significant differences in strength of concrete were found (coefficient of variation below 5%), therefore, mean values were assumed for the further analysis. The compressive strengths, determined on cylindrical samples with diameter $\phi 150$ mm and height of 300 mm, were equal to $f_{\text{cm}} = 28.9$ MPa (slab), $f_{\text{cm}} = 55.0$ MPa (upper

column), $f_{cm} = 45.5$ MPa (bottom column). The secant moduli of elasticity were: $E_{cm} = 23.6$ GPa (slab), $E_{cm} = 34.7$ MPa (bottom column).

Reinforcement was made of steel grade B500 with a ductility class C. The strength parameters were determined on three samples taken randomly from bars of each diameter. The average yield strengths were: $f_{ym} = 562.9$ MPa ($\phi 10$ bars) and $f_{ym} = 546.3$ MPa ($\phi 20$ bars).

2.2. Test setup and testing procedure

The way of loading of the corner connections results in acting of the unbalanced bending moment, transmitted from the slab to the column. To balance the horizontal forces resulting from the action of the unbalanced moment, an additional reinforced concrete element connected with the tested specimen employing a steel ties, located in the upper part of the column, was used – see Fig 3a. The test setup enabled applying load on columns and slab independently. The tests were conducted in a universal testing machine with a maximum pressure of 6000 kN. The load was transferred on the columns of both elements utilizing a steel plate girder. The test was started with applying load on the column only. The total load was dependent on the assumed level of utilization of the column resistance and equal to 500 kN (MN/1.25/L), 1000 kN (MN/1.25/M) or 1500 kN (MN/1.25/H). Including the contribution of the longitudinal reinforcement, it corresponded to stress at the column base of about 0.40, 0.76 and 1.14 f_{cm} (where f_{cm} is the average uniaxial compressive strength of the slab concrete).

The load was applied on the column gradually, with an increase of 100 or 150 kN at every step. While increasing the load, deformation on the column surface was controlled and, if necessary, a slight adjustment of the hinge position was made to achieve a nearly axially load transmission. After reaching the assumed load level, the second phase of the test began. In this phase, only the slab load was increased while the load applied on column remained unchanged. The tests were carried out under load control. The slab was loaded using a hydraulic jack with a maximum pressure of 200 kN. The actuator was connected to the traverse, which allowed to apply the load at two-point distant of 100 mm from the free edges of the slab. The location of the actuator enabled to obtain a relative load eccentricity e/c equal to about 1.25 (where e is the distance between the axis of the column and the actuator while c is the column width). The slab load was applied gradually, at 5 kN in each step (loading rate was limited at the end of the test).

a)



b)

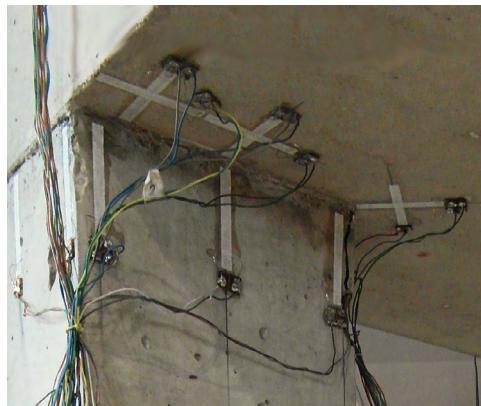


Fig. 3. The test setup and location of strain gauges. *Source:* own study

After each increase in load, cracks on the upper surface of the slab were stock taken, and widths of selected cracks were measured. During the test, strains of the longitudinal slab reinforcement, as well as strains of the slab (on the bottom side only) and column surface, were also recorded – see Fig. 3b. Strain gauges were used for this purpose.

2.3. Test results

2.3.1. Strains of the slab reinforcement

During the tests, strains of the longitudinal reinforcement at the column edge were measured. Figure 4 shows the development of the strains ε_s as a function of slab load V_{slab} . In the initial phase of the test, the slab remained unloaded ($V_{slab} = 0$). However, an increase in deformations was observed, which resulted only from increasing of column load. The average strains of the longitudinal reinforcement noted at the end of the first phase of the test was $\varepsilon_{s,init} = -0.01, 0.08$ and 0.26% , for MN/1.25/L, MN/1.25/M and MN/1.25/H specimens respectively. A clear relationship between the column load level and initial strains in the longitudinal reinforcement was therefore visible. Although in the study corner columns, surrounded by the slab only from two sides, were considered, lateral expansion of joint concrete was stated, what was in line with the results of previous investigations concerning corner and edge columns intersected by weaker slab concrete [1]. By increasing the slab load in the next phase of the test, a further, more pronounced increase in strains was stated. In all specimens, failure was preceded by yielding of the reinforcement at the column edge. Due to initial deformation $\varepsilon_{s,init}$, loads, at which the average strains reached yield strain $\varepsilon_{ym} = 2.80\%$, were varied and amounted to about $100 \div 115$ kN ($80 \div 90\%$ of the destructive forces V_{exp}). As it comes to MN/1.25/L specimen, yielding of the reinforcement occurred at the latest, which resulted from the lack of the initial deformations due to the column load – $\varepsilon_{s,init} \approx 0$.

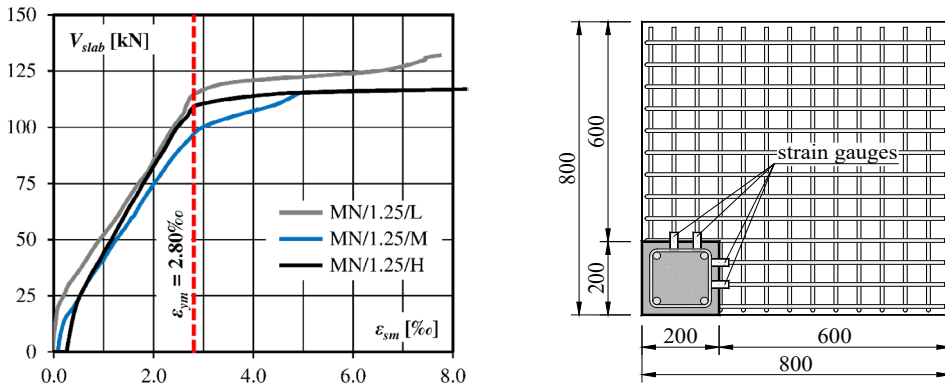


Fig. 4. Strains of the slab longitudinal reinforcement and location of the strain gauges (dashed line corresponds to yield strain). *Source:* own study

2.3.2. Strains on the slab surface

In Figure 5, the results of the strain measurements on the bottom side of the slab were presented. The deformations in the radial direction indicated tension at the initial phase of the test, what can be identified with the lateral expansion of joint concrete due

to the column pressure. These strains depended on the column load level and were about $\varepsilon_{c,init} = 0.05 \div 0.37\%$. Higher strains were recorded in the vicinity of the free edges of the slab (see strain gauges marked in black and the corresponding dashed lines in Fig. 5), which indicated higher deformations of the joint concrete in this area (and therefore less confinement). The increase in the slab load led to a change in the nature of the strains at a load of approximately $0.1 \div 0.4 V_{exp}$, depending on the column load level. Compression resulting from bending of the slab was recorded on the bottom surface for most of the second phase of the test.

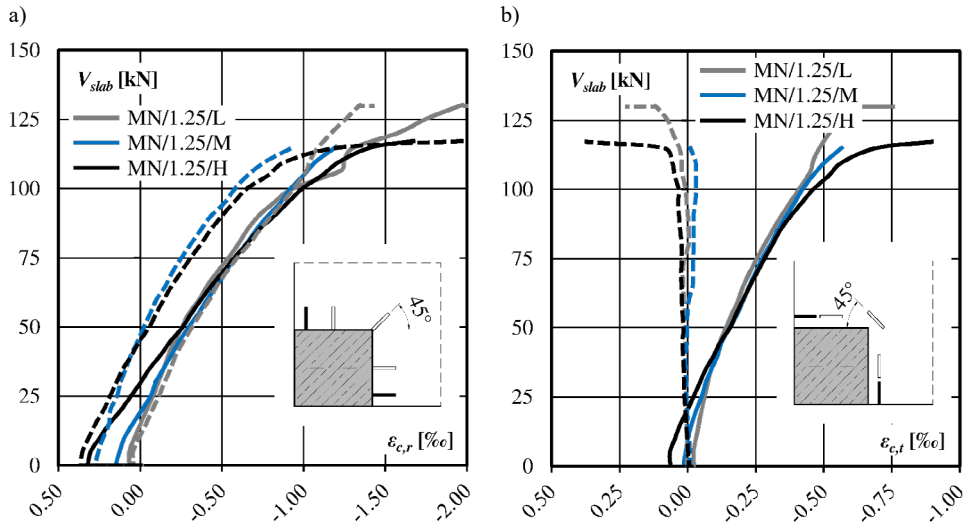


Fig. 5. Concrete strains on the compressed side of the slab: a) radial direction, b) tangential direction; (dashed lines correspond to external strain gauges marked with black). *Source:* own study

Comparing the strain development in the tangential direction, one can notice its different intensity in the vicinity of the inner corner of the column and the free edges of the slab. In the first location, a uniform increase in deformation was observed from the beginning of the second phase of the test. However, in the vicinity of the free edge, they remained almost unchanged. Only in the final phase of the test, preceding failure, a significant increase in these strains, indicating tensile stress, was observed. The above may indicate the degradation of the slab stiffness associated with the formation of diagonal shear cracks and the resulting reduction in the confining action.

In Figure 6, deformations measured on the surface of the bottom and upper columns in the vicinity of the inner (dashed lines) and outer corner (solid lines) were presented. Increasing the column load led to an increase in strains. The values measured after the end of the first phase of the test were proportional to the load applied on the column and equal on average $\varepsilon_c = -0.29, -0.60$ and -0.90% , for MN/1.25/L, MN/1.25/M and MN/1.25/H models respectively. Increase in slab load resulted in a change in recorded strains. In the case of MN/1.25/L and MN/1.25/M specimens, an even change in their nature was observed. Shortly before failure tensile stresses were measured, which could have resulted from the spalling of concrete cover.

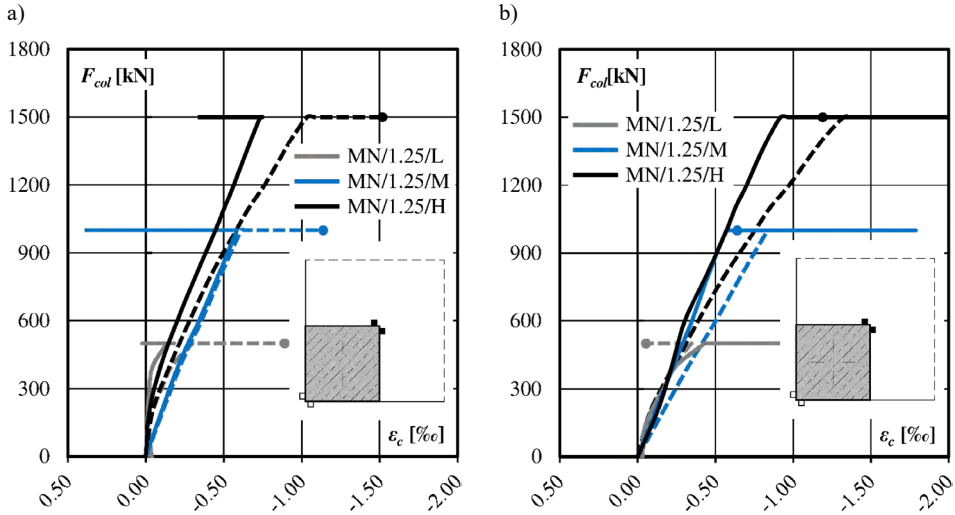


Fig. 6. Concrete strains on column surface close to corner: a) upper column, b) bottom column; (dashed lines correspond to strain gauges on the internal corner, marked with black). *Source:* own study

2.3.3. Crack pattern

Figure 7 shows the crack pattern on the upper surface of the MN/1.25/L and MN/1.25/H specimens at the same load level, equal to $V_{\text{slab}} = 100$ kN. Diagonal cracks, typical for external column-slab connections and resulting bending moment in the direction inclined at an angle of 45° to the free edge, were visible. More intense cracking was observed in case of the M/1.25/H specimen, which can be attributed to higher lateral expansion of joint concrete due to column pressure.

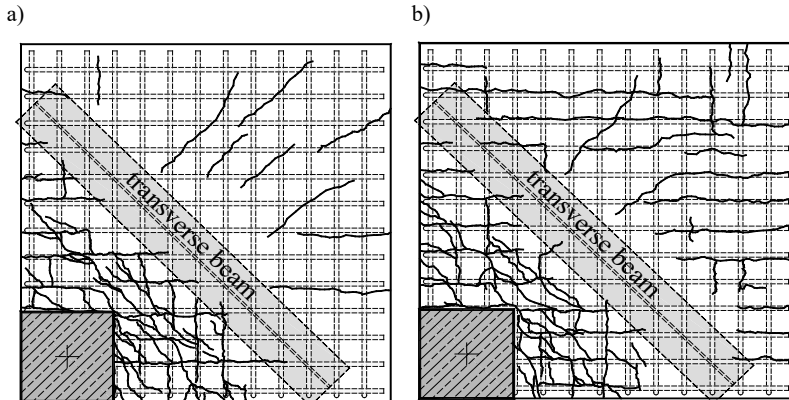


Fig. 7. Crack pattern on upper slab surface at a load of 100 kN: a) M/1.25/L, b) M/1.25/H. *Source:* own study

2.3.4. Load-carrying capacities

The failure of all the specimens was violent, characteristic for punching shear. However, it was preceded by a noticeable slab deflections and intense cracking of the upper slab surface. This indicates that failure was a result of the combined shear and bending mechanism, which is also consistent with the assumptions of *Urban's* theory [7] because the mechanical reinforce-

ment ratio was equal to $\omega = 0.21 < 0.30$. In Figure 8, the test results in the form of a relationship between experimental load V_{exp} and applied column load F_{col} were presented. Besides, the horizontal axis includes the relative stress σ_c/f_{cm} resulting from column pressure. The total load applied on the specimens resulted in stress σ_c equal to $0.52, 0.86$ and $1.24f_{cm}$, for MN/1.25/L, MN/1.25/M and MN/1.25/H specimens respectively.

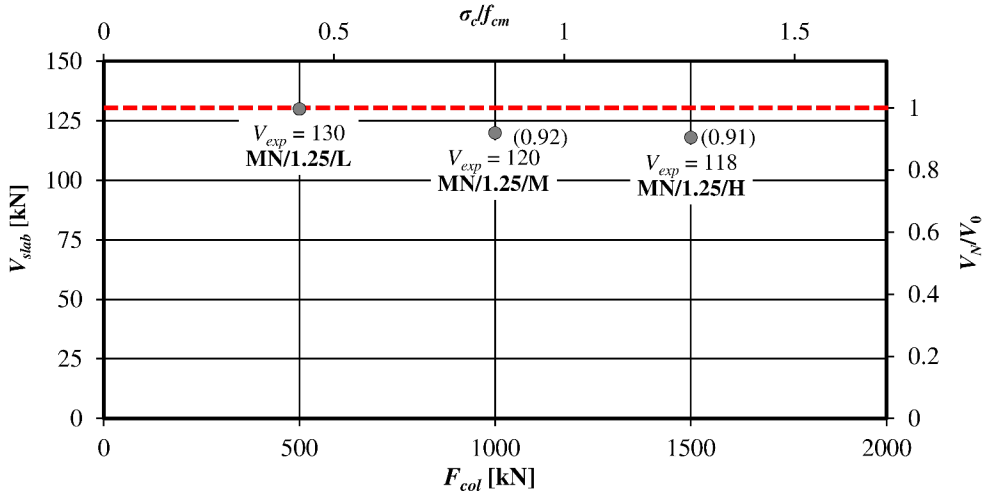


Fig. 8. Experimental loads V_{exp} with respect to column load level F_{col} . Source: own study

Assuming that the experimental load capacity of the MN/1.25/L specimen as a benchmark, it can be seen that an increase in the column load by 500 and 1000 kN, resulted in a reduction of the experimental loads by 7.7 and 9.2%, respectively. Thus, the effect of the column load on the punching shear resistance was noticeable, although relatively small.

3. Results of the tests in the light of Eurocode 2 provisions

The verification of the punching shear resistance according to EN 1992-1-1 [8] consists in comparing the ultimate stress $v_{Rd,c}$ (expressing the load capacity) and shear stress v_{Ed} (representing the effects of actions). The punching shear resistance is described by eq. (1)

$$v_{Rd,c} = C_{Rd,c} k^3 \sqrt{100 \rho_l f_{ck}} + k_1 \sigma_{cp}, \quad (1)$$

where:

$C_{Rd,c}$ – empirical factor, equal to $0.18/\gamma_c$,

γ_c – partial safety factor corresponding to concrete,

k – size effect factor, $k = \min[1 + (200/d)^{0.5}; 2.0]$ (d in mm),

ρ_l – mean longitudinal reinforcement ratio, $\rho_l \leq 0.02$,

f_{ck} – concrete compressive strength,

k_1 – factor equal to 0.10,

σ_{cp} – mean stress normal to the cross-section of the slab,

d – mean effective depth of the slab.

Shear stress in the basic control section located at a distance of $2d$ from the column face are determined according to the relationship (2). The β coefficient expresses the effect of the unbalanced bending moment transmitted from the slab to the column on the distribution of shear stress along the control section (plastic shear stress distribution is assumed). It can be determined in a general way or by one of two simplified methods, which were discussed in more detail in [9]. Stress v_{Ed} is given as follows

$$v_{Rd,c} = \frac{\beta \cdot V_{ED}}{u_1 \cdot d}, \quad (2)$$

where:

- V_{Ed} – shear force,
- β – increasing factor,
- u_1 – length of the basic control perimeter,
- d – mean effective depth of the slab.

The theoretical punching shear resistances were calculated by transforming the equation (2) and substituting the ultimate shear stress, determined according to the equation (1). In the calculations, the average strength of slab concrete (f_{cm}) and partial safety factor $\gamma_c = 1$ were considered. Due to the constant load eccentricity $e = 354$ mm, the coefficients β were the same for all of the specimens and equal to $\beta = 1.57, 1.34$ and 1.5 , for the general method, method of reduced control perimeters and method of constant β factors respectively. The β value resulting from the general method was adopted for further analysis.

The results of the calculations were presented in Table 1. As the comparison of the obtained results was made, it can be stated that the procedure of EN 1992-1-1 [8] allowed to determine the punching shear resistances in a safe but very conservative manner. Although the load capacity dropped as the column load increased, in no case did the experimental to theoretical load ratio V_{exp}/V_{calc} reach below 1.75. This observation is consistent with the results of previous analyses presented in [9] and may indicate the conservativeness of the EN 1992-1-1 [8] procedure with respect to corner column- slab connections.

Table 1. Results of the calculations, according to EN 1992-1-1 [8] provisions. *Source:* own study

Specimen	f_{cm} [MPa]	d [mm]	ρ_1 [%]	u_1 [mm]	u_{1*} [mm]	V_{exp} [kN]	V_{calc} [kN]	$\frac{V_{exp}}{V_{calc}}$
MN/1.25/L						130		1.93
MN/1.25/M	28.9	120	1.09	777	577	120	67.4	1.78
MN/1.25/H						118		1.75

4. Conclusions

The presented experimental investigations demonstrated that the load of corner columns might affect the punching shear resistance of the slabs. However, the change in the slab load-carrying capacity resulting from a three-fold increase in the column load turned out to be low and did not exceed 10%. It is worth mentioning here that the load applied on the column had an opposite effect to that observed in case of previous studies concerning internal column-slab connection joints, when an increase in the punching shear resistance was stated. In case of MN/1.25/H specimen, the stress at the column base exceeded by 25% uniaxial compressive

strength of the slab concrete, however, the beneficial effects resulting from the lateral stress due to expansion of joint concrete were not observed, as suggested by the considerations presented in Fig. 1. Measurements of the strains of longitudinal slab reinforcement indicated that additional tensile forces, which arose from the expansion of joint concrete, could prove crucial. This resulted in yielding of the reinforcement at lower load levels and thus limited flexural capacity, which turned out to be decisive in the case of failure associated with the combined shear and bending mechanism.


The analysis carried out in the light of the recommendations of EN 1992-1-1 [8] showed that the standard procedure allowed for safe but conservative estimation of the load-carrying capacities of all of the considered models. Depending on the column load level, the ratio of experimental to theoretical load $V_{\text{exp}}/V_{\text{calc}}$ equal to $1.75 \div 1.93$ was obtained. These results turned out to be similar to the findings of previous analyses presented in [9]. This may indicate a certain conservativity of the EN 1992-1-1 [8] procedure concerning corner column-slab connections. However, due to a relatively low number of tested elements, general recommendations cannot be formulated and further investigations, including among others edge connections, are needed.


References

- [1] Urban T. S. and Gołdyn M.M., “Behaviour of eccentrically loaded high-strength concrete columns intersected by lower-strength concrete slabs,” *Structural Concrete*, vol. 16, no. 4, (Dec. 2015), pp. 480–495. <https://doi.org/10.1002/suco.201400114>
- [2] Gołdyn M. et al., “Carrying Capacity of Axially Loaded HSC Columns Intersected by NSC Slab,” *Architecture • Civil Engineering • Environment – ACEE*, vol. 8, no. 3, (2015), pp. 51–60.
- [3] Guidotti R. et al., “Crushing and flexural strength of slab-column joints,” *Engineering Structures*, vol. 33, no. 3, (Mar. 2011), pp. 855–867. <https://doi.org/10.1016/j.engstruct.2010.12.007>
- [4] Guidotti R. et al., “Durchstanzen von Flachdecken bei hohen Stützenlasten,” *Beton- und Stahlbetonbau*, vol. 105, no. 1, (Jan. 2010), pp. 19–26. <https://doi.org/10.1002/best.200900066>
- [5] Clément T. et al., “Influence of prestressing on the punching strength of post-tensioned slabs,” *Engineering Structures*, vol. 72, (Aug. 2014), pp. 56–69. <https://doi.org/10.1016/j.engstruct.2014.04.034>
- [6] Ramos A. P. et al., “The effect of the vertical component of prestress forces on the punching strength of flat slabs,” *Engineering Structures*, vol. 76, (Oct. 2014), pp. 90–98. <https://doi.org/10.1016/j.engstruct.2014.06.039>
- [7] Urban T., *Przebiecie w żelbecie: wybrane zagadnienia*. Łódź: Zeszyty Naukowe. Rozprawy Naukowe / Politechnika Łódzka, 2005.
- [8] EN 1992-1-1: *Eurocode 2: Design of concrete structures – Part 1-1: General rules and rules for buildings*, Brussels: European Committee for Standardisation, 2004.
- [9] Gołdyn M. and Urban T., “Komentarz do zasad obliczania płyt na przebiecie w strefie słupów narożnych według Eurokodu 2,” *Journal of Civil Engineering, Environment and Architecture*, vol. 64, no. 3, (2017), pp. 235–245. <https://doi.org/10.7862/rb.2017.118>

Simulation of four-point beam bending test using the X-FEM method

Jakub Gontarz¹, Jerzy Podgórski²

¹ Department of Structural Mechanics; Faculty of Civil Engineering;
Lublin University of Technology; 40 Nadbystrzycka Street, 20-618 Lublin, Poland;
j.gontarz@pollub.pl  0000-0002-6900-6158

² Department of Structural Mechanics; Faculty of Civil Engineering;
Lublin University of Technology; 40 Nadbystrzycka Street, 20-618 Lublin, Poland;
j.podgorski@pollub.pl  0000-0003-4745-7705

Funding: This research was financed by the Lublin University of Technology Science Financing Subsidy FN16/ILT/2020.

Abstract: This article presents the results of the computer simulations of a four-point bending test of a concrete single-edge notched beam. In this publication, the authors compared the X-FEM method of simulating the crack in the Abaqus FEA system. The paper also contains the results obtained with the Abaqus subroutine recently developed by the authors, used for defining the direction of the crack and the failure criterion. The publication explains the way of working of this algorithm. The described calculations show that computer analysis gives unrealistic results in terms of the destructive force. SEN-beam is an interesting laboratory test in which a lot of factors influence the results. It is especially important to study what phenomena occur in the final phase of the study, when the crack tip is near the opposite side.

Keywords: SEN-beam, X-FEM, Fracture Mechanics, Abaqus user subroutine

1. Introduction

This article presents an attempt to simulate a four-point bending test on a concrete single-edge notched beam (SEN-beam) in the Abaqus FEA system using different material damage methods, especially the X-FEM method with its own damage criteria. The aim of this article is to verify how the X-FEM method behaves when simulating the SEN-beam, and check the Abaqus User Subroutines developed by the authors. The SEN-beam test is an interesting topic, but there are not many publications about it. It was first described by Carpinteri et al. [1]. The paper [2] describes different tests including the SEN-beam bending test. It uses the cohe-

sive-zone damage model with different approaches to implement this method in numerical calculations. The publication described here, however, does not focus on concrete, but only on the cohesive-zone method for any brittle material. Another work [3] describes different fracture modelling approaches to gravity dam failure. Various models are described, including a concrete SEN-beam. This paper is a good data source. The paper gives, for example, crack paths for various numerical methods as well as for laboratory tests of the described beam. The paper [4] by Tabatabaee et al. includes, among others, a comparison of the SEN-beam test with other similar tests.

2. Description of the model

Dimensions and loads of the test are taken from Schalangen's paper [5] and are shown in Fig. 1. Lengths are indicated in mm.

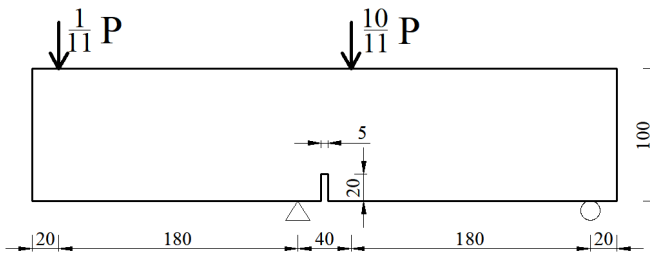


Fig. 1. The geometry of SEN-beam. *Source:* the authors' own study based on [5]

The external dimensions of the beam are 440x100x100 mm. In the centre of the bottom edge, there is a 20mm deep notch, from which the crack should start. The simulations were performed in the Abaqus FEA system. The load was modelled as displacement at two points, which increased linearly to the value of 0.909 mm at the right point and to the value of 0.091 mm at the left point. The load was applied cyclically (the model was loaded and unloaded 5 times during calculations), because the task has a certain characteristic – the force in the supports increases proportionally to the given displacement, even after the failure of the element. During the tests, it turned out that the crack length increases even when the force stays the same or decreases. Therefore, it is not appropriate to inflict a constantly increasing load in such a task, because the crack cannot keep up with the load, hence the need for cyclic unloading.

The model mesh is shown in Fig. 2. The mesh size is about 15 mm, while in the area where the crack is predicted, the mesh has been compacted to 1.5 mm. The taken material is concrete C35/45 with the following parameters:

- Young's modulus – $E = 34$ GPa;
- Poisson's ratio – $\nu = 0.2$;
- Compressive strength – $f_{ck,cube} = 45$ MPa;
- Tensile strength – $f_{ctm} = 3.2$ MPa;
- Critical strain energy release rate – $G_{Ic} = 0.1$ N/mm.

These parameters were taken from the papers [6] and [7].

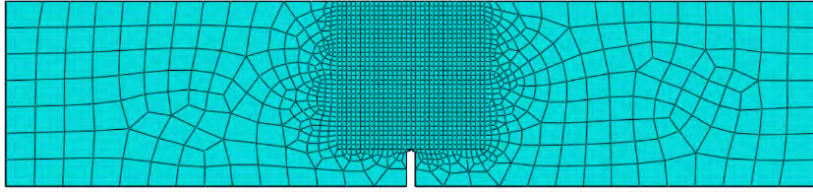


Fig. 2. Mesh of the described model. *Source:* the authors' own study

3. Results from Abaqus

3.1. Explanation of the X-FEM method

X-FEM (extended Finite Element Method) is a method of simulating the fracture regardless of the finite element mesh. In each increment, the program leads the crack to the next element, modifying the displacements in the element nodes with an appropriate shape function. The advantage of this method, for example, over the methods which use smeared crack or element deletion is a short calculation time (the longest calculations used in this test lasted 15 minutes), high accuracy in predicting the crack path regardless of the finite element mesh. This method requires little data to calculate the simplest maximum principal stresses criterion. The disadvantage of this method is that it is limited to one crack. What is more, it works best only for static calculations.

The authors attempted to simulate the fracture of the SEN-beam. The criterion of the maximum principal stress was chosen for the initiation and propagation of the crack [8]. The direction of the crack is the direction of rotation of the stress in the element to the principal stresses. When the load grows, the stress in the model increases, and the material effort increases with them. Material effort (μ) is a quantity described by Podgórski in [9]. If the effort exceeds 1, then the crack goes through the next finite element. The calculated material effort depends on the chosen element type. For X-FEM in Abaqus, only four-node elements are available. When the reduced integration is chosen, then the material effort is calculated as the ratio of the maximum principal stresses in the centre of the element to the tensile strength. When no reduced integration is selected, the program calculates this effort for four integration points of the element and then determines the arithmetic mean. The same goes for determination of the direction of the crack. This is not an ideal approach, because the most correct would be to take stresses from the point of the crack tip instead of from the centre of the element. In this way more force is needed to destroy the element. It also depends on the size of the mesh. The larger the finite element, the further away from the crack tip are the integration points, and hence the smaller stresses in them. This means that for correct calculations a dense mesh is needed.

3.2. Results of the crack path and maximum force

In previous works, the authors described that the path calculated in Abaqus using XFEM is unrealistic [10]. However, in the case of the SEN-beam test, the crack path results are satisfactory, and the only drawback is that the crack cannot pass through the last finite element. The Fig. 3a presented below is the picture from the program and the Fig. 3b is the comparison with the results of laboratory tests obtained by de Borst [2] and Pan et al. [3].

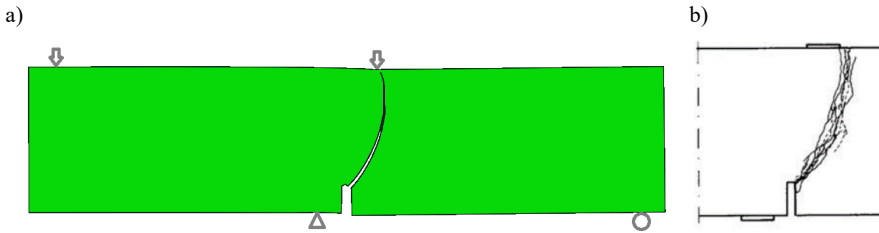


Fig. 3. The crack path for SEN-beam. a) Results from Abaqus. *Source:* the authors' own study, b) the results from laboratory tests. *Source:* [3]

However, the obtained maximum force is very different from the similar tests presented in the source literature [3], [5]. The maximum force in the simulation is 110.1 kN, and for laboratory tests, the force is about 40 kN.

4. Abaqus user subroutine developed by the authors

4.1. The main algorithm

Abaqus allows implementation of the custom crack propagation criterion with the use of user subroutines. The authors prepared several subroutines in Fortran. These are two algorithms, the first concerns the own approach to the criterion of maximum principal stresses, the second is the implementation of the Ottosen-Podgórski criterion [9]. The main simplified algorithm of Abaqus operation with the use of subroutines used by the authors is shown in Fig. 4.

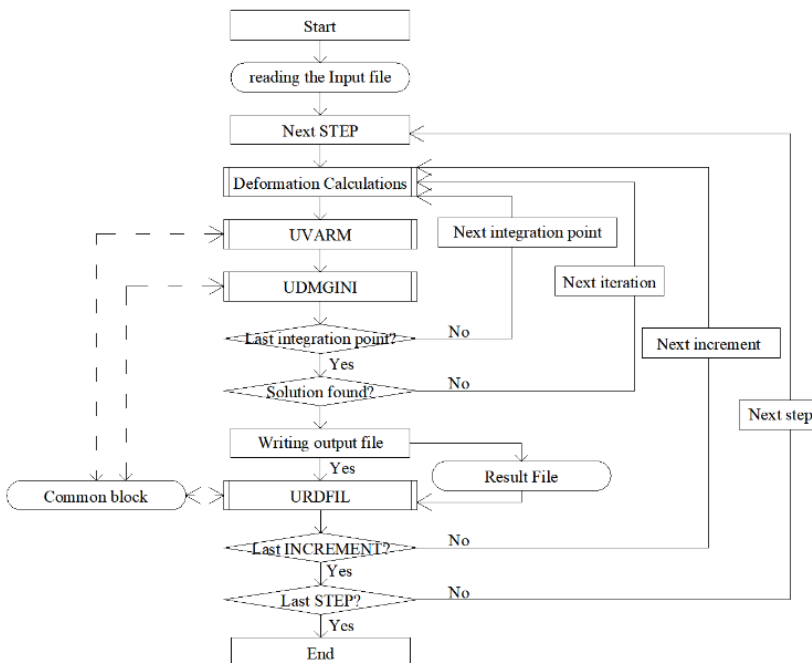


Fig. 4. Simplified Abaqus FEM algorithm containing needed subroutines. *Source:* the authors' own study

First, Abaqus calculates the model and then uses the UVARM subroutine, and then the UDMGINI subroutine separately for every integration point and every iteration. The UVARM subroutine is needed only to read the stresses in every integration point and transfer them by “Fortran Common block” to the UDMGINI subroutine. This subroutine determines the crack direction and the value of the searched criterion. When it decides to lead the crack to the next element (solution found), it writes the results in the Result File. When the URDFIL subroutine reads the Result File and all calculations for determining the crack are performed in this subroutine, it transfers the obtained crack propagation angle to the next increment with the Common block [8]. The reason that all calculations for determining the crack angle are made in URDFIL subroutine, not in UDMGINI is that the URDFIL subroutine is performed only every increment which is dozens of times less than UDMGINI subroutine, which is performed for every integration point and during several iteration for one analysed finite element. Also, the URDFIL subroutine is performed once for the whole model, not for enriched finite elements. This procedure is possible because within one increment the stresses change in relation to each other, and the angle is determined by proportions of the stresses in the model, not by their values, which is explained below.

As mentioned earlier in the case of four integration points in the element, the criterion is averaged from these four points. In the described method, in the first three integration points Abaqus only reads the data in the UVARM subroutine needed for calculations, and in the UDMGINI subroutine the effort is set to 0. However, all calculations are made only at the fourth integration point, and then the most efforted integration point is selected and the effort value is set 4 times bigger; therefore, after calculating the average by Abaqus, the effort value obtains the desired value. This can be illustrated by the example of the following formula:

$$\mu = \frac{0+0+0+4 \cdot \mu_{max}}{4} \quad (1)$$

The same thing applies to determination of the angle of the crack. There is no simpler solution, because Abaqus does not allow to modify its built-in algorithm of separate calculation for all integration points. The method described above is not ideal because it takes stress at integration points. Ideally, stress should be applied exactly at the crack tip.

4.2. Determining the crack angle

To determine the direction of the crack, the authors used Griffith’s crack and Westergaard solution [11]. Griffith’s crack is shown in Fig. 5.

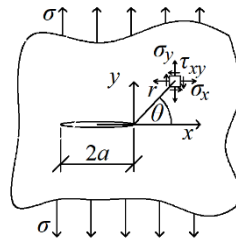


Fig. 5. Griffith’s crack. Source: [11]

Stresses around the crack tip depend on material parameters, angle θ (from -180° to 180°), distance from the crack tip r , and can be simplified to:

$$\begin{aligned}
 \sigma_x(r, \theta) &= \frac{1}{\sqrt{r}} \cdot \cos\left(\frac{\theta}{2}\right) \cdot \left[1 - \sin\left(\frac{\theta}{2}\right) \cdot \sin\left(\frac{3\theta}{2}\right)\right], \\
 \sigma_y(r, \theta) &= \frac{1}{\sqrt{r}} \cdot \cos\left(\frac{\theta}{2}\right) \cdot \left[1 + \sin\left(\frac{\theta}{2}\right) \cdot \sin\left(\frac{3\theta}{2}\right)\right], \\
 \tau_{xy}(r, \theta) &= \frac{1}{\sqrt{r}} \cdot \sin\left(\frac{\theta}{2}\right) \cdot \cos\left(\frac{\theta}{2}\right) \cdot \cos\left(\frac{3\theta}{2}\right)
 \end{aligned} \tag{2}$$

After calculating the material effort for principal stress criterion and the Ottosen-Podgórski criterion [9] for $r = 1$, the graph is obtained (shown in Fig. 6). As it is a symmetrical task, it can be concluded that the crack will be led at an angle where the minimum material effort value is obtained.

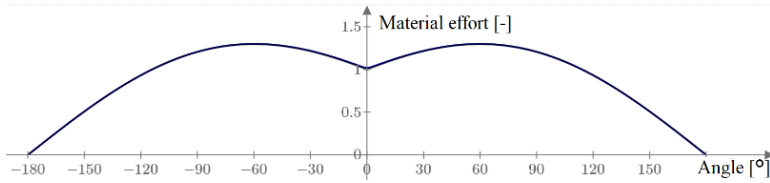


Fig. 6. Relation between the material effort for both criteria and angle relative to the crack. *Source:* the authors' own study based on [9]

In Abaqus, it is not possible to read the crack tip coordinates directly from the Results file. Therefore, before the presentation of the operation of the crack propagation algorithm, the data from Abaqus PHILSM should be explained. PHILSM is a result that occurs only on cracked finite elements. It has positive values on the one side of the crack and negative on the other. With a linear fit, the crack is where the PHILSM takes the value 0. Knowing the PHILSM values in the nodes and their coordinates, the algorithm determines the coordinates of the crack tip.

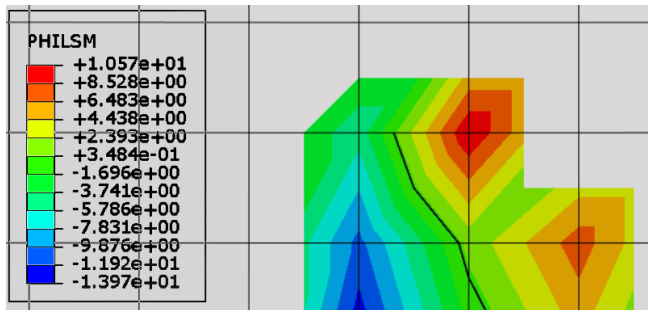


Fig. 7. Explanation of the PHILSM values. *Source:* the authors' own study

As it was said before, the crack angle is calculated in UVARM subroutine. The outline of its process is as follows:

- Reading the “Result file” for the previous increment for the whole model – coordinates and stresses in integration points, PHILSM, and coordinates for nodes;

- Calculating the material effort for all integration points. Material effort formulas depend on the chosen destruction criterion. The value of material effort depends only on stress;
- Calculating the crack tip coordinates from the PHILSM values;
- Reducing material effort values only to about 30 nearest integration points around the crack tip;
- Bringing material effort values to the radius = 1, knowing that:

$$\sigma = \frac{1}{\sqrt{r}} \cdot f(\theta) \quad (3)$$

to get the result for radius $r = 1$ material effort is multiplied by \sqrt{r} ,

- Some values on the obtained graph are shifted 360 degrees to the left or right so that the angle from the previous increment is 0;
- Fitting the 6th-degree polynomial to points using the method of least squares;
- Finding the minimum value nearest to the angle from the previous increment by the bisection method.

The new angle of the crack tip is the x value where this minimum was found. The last four points listed above are illustrated on exemplary values in Fig. 8.

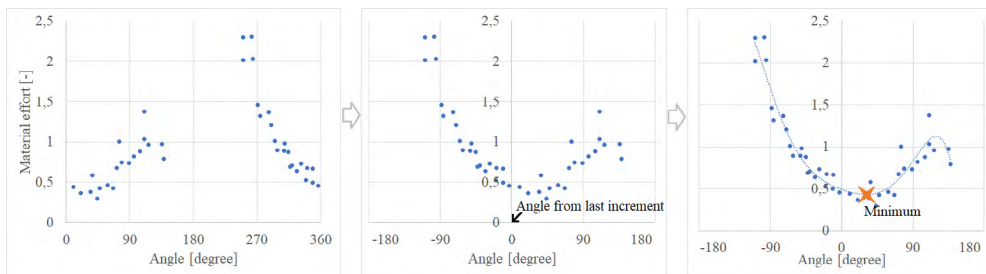


Fig. 8. Calculating the new crack angle from material efforts around the crack tip. *Source:* the authors' own study

5. Results for the authors' own subroutine

The above subroutine was submitted to the same simulation as in chapter 3.2. For the same criterion (maximum principal stress), the destructive force is 108.7 kN, and for the Ottosen-Podgórski criterion, the force is 104.9 kN. For both criteria, the crack paths almost do not differ from each other (Fig. 9a). The Fig. 9b shows the differences between crack path for default Abaqus criterion, for the result with using subroutines, and for laboratory tests.

The obtained results are visibly similar, but the simulation with user subroutine gives outputs more similar to laboratory tests. In addition, some correlation was also noticed – the further to the right the crack reaches, the more strength is needed to destroy the model. If the crack obtained by the default Abaqus method were closer to the laboratory results (more to the right), the value of 110.1 kN would be even greater, and thus even further away from laboratory tests. This means that the results obtained with the use of the subroutine are closer to reality both in terms of the crack path and the maximum force obtained.

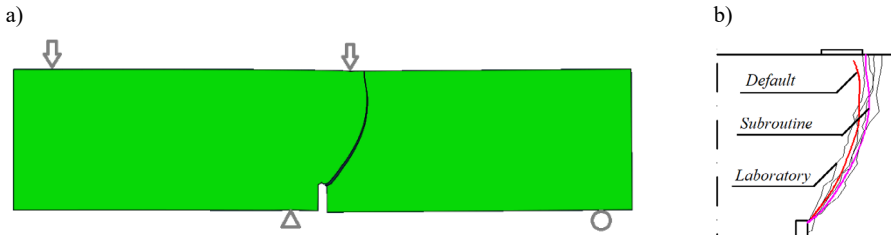


Fig. 9. a) A crack path for SEN-beam obtained with the use of the subroutine. *Source:* the authors' own study, b) The comparison of all crack paths: *Source:* the authors' own study based on [3]

Despite the above conclusions, the obtained force results are not satisfactory. Although they are better than the results for the default method, they are definitely different from the laboratory results.

However, it is worth paying attention to the diagram in Fig. 10. It presents the relation between the degree of cracking and strength during calculations. The crack length is expressed as a percentage ratio of the current crack length to the final length (total failure). This figure shows the cyclical increase in force and crack as well as the decrease in strength and stop of the increase in crack length. It should be noted, however, that at the end of the second increase in force, when the force was about 55 kN (close to the force from laboratory tests), the crack reached 90% of its final length, which is almost full destruction. Then, with each large increase in strength, the crack almost did not grow. The final part that should break is the area where very low tensile forces act on the crack, and compressive forces dominate, which are not taken into account in the discussed failure criteria. Another reason for this phenomenon may be a different type of support in comparison with the performed laboratory tests. Perhaps it might be influenced by the ability of the lower supports to move vertically. In the future, the authors plan to change the boundary conditions and replace them with additional elements in the model, that allows all movements occurring in the laboratory test.

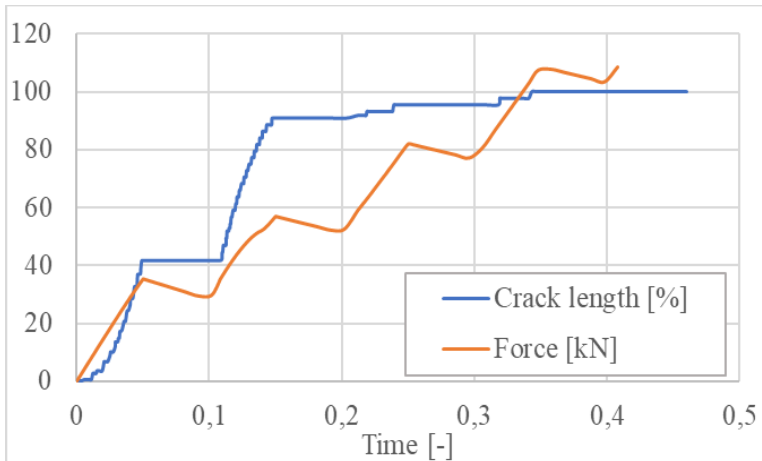


Fig. 10. The relation between the crack length and force during the simulation. *Source:* the authors' own study

6. Summary

The described calculations show that computer analysis gives results that are far from reality in terms of destructive force. SEN-beam is an interesting laboratory test in which many factors influence the results. It is particularly important to examine what phenomena occur in the final phase of the test when the crack is near the opposite side. For this particular test, the results obtained from tests made with user subroutine are slightly better than the ones with the use of the default maximal principal stress criterion.

It is also interesting that for this particular experiment the results obtained by default in the Abaqus program are very similar to those obtained with the subroutine. Usually, the calculations using this subroutine give much better results. For example, in a simple three-point bending test of a notched beam shown in Fig. 11, it is clearly visible that the results obtained from default in-build Abaqus criterion (a) are completely unrealistic, and the results from the simulation using the subroutine (b) are very good.

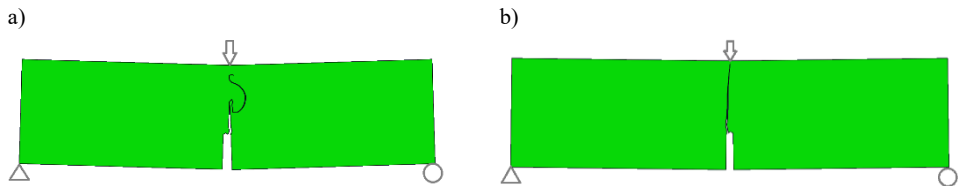


Fig. 11. The crack path for a three-point bending test on notched beam, a) the results obtained with the use of in-build Abaqus criterion, b) the results obtained with a simulation with the authors' subroutine. *Source:* the authors' own study

Moreover, for the above example, the force obtained with the authors' subroutine is very close to real value in comparison with the default Abaqus criterion. But this is the topic for future papers.

References


- [1] Carpinteri A. et al., "Single edge notched specimen subjected to four point shear: an experimental investigation," in *Fracture of Concrete and Rock -Recent Developments*, Shah S. P. et al. Eds. London/New York: Elsevier Applied Science Publishers, 1989, pp. 605–614.
- [2] de Borst R., "Numerical aspects of cohesive-zone models," *Engineering Fracture Mechanics*, vol. 70, (2003), pp. 1743–1757. [https://doi.org/10.1016/S0013-7944\(03\)00122-X](https://doi.org/10.1016/S0013-7944(03)00122-X)
- [3] Pan J. et al., "Comparison of different fracture modelling approaches to gravity dam failure," *Engineering Computations (Swansea, Wales)*, vol. 31, no. 1, (2014), pp. 18–32. <https://doi.org/10.1108/EC-04-2012-0091>
- [4] Tabatabaee H. A. et al., *Investigation of Low Temperature Cracking in Asphalt Pavements National Pooled Fund Study – Phase II*, no. January. University of Wisconsin-Madison, 2012.
- [5] Schlangen E., "Experimental and numerical analysis of fracture process in concrete", *Heron*, vol. 38, no. 2, 1993. <http://resolver.tudelft.nl/uuid:086bbfba-699b-43fd-a9c6-b0f2bed3e5af>
- [6] *PN-EN 1992-1-1*, 2004. Eurokod 2: Projektowanie konstrukcji z betonu – Część 1-1: Reguły ogólne i reguły dla budynków.
- [7] van Mier J.G.M., *Fracture processes of concrete*. CRC Press, 1996.
- [8] "Abaqus V 6.14.2 Users Manual," Available: <https://www.sharcnet.ca/Software/Abaqus/6.14.2/v6.14/books/usb/default.htm?startat=pt04ch10s07at36.html>

- [9] Podgórski J., “The criterion for determining the direction of crack propagation in a random pattern composites,” *Meccanica*, vol. 52, no. 8, (2017), pp. 1923–1934. <https://doi.org/10.1007/s11012-016-0523-y>
- [10] Gontarz J. et al., “Comparison between numerical analysis and actual results for a pull-out test,” *Engineering Transactions*, vol. 67, no. 3, (2019), pp. 311–331. <https://doi.org/10.24423/EngTrans.1005.20190815>
- [11] Westergaard H.M., “Bearing Pressure and Cracks”, *J. Appl. Mech.*, vol. 61, (1939), pp. A49–A53.

Influence of the interface reinforcement on static performance of concrete composite T-shaped beams

Łukasz Jabłoński¹, Anna Halicka²

¹ Faculty of Civil Engineering and Architecture; Lublin University of Technology;
40 Nadbystrzycka Street, 20-618 Lublin, Poland;
l.jablonski@pollub.pl  0000-0002-9221-8335

² Faculty of Civil Engineering and Architecture; Lublin University of Technology;
40 Nadbystrzycka Street, 20-618 Lublin, Poland;
a.halicka@pollub.pl  0000-0001-5526-8862

Abstract: The tests results of composite reinforced concrete T-shaped beams with an interface between the web and the flange are presented. The interface in the beams differed in the degree of the adhesion activity and the joining reinforcement ratio. Five series of beams were tested for deflection, displacement of composite parts in relation to each other, strain of main and transverse reinforcement, and crack pattern. The results were compared with the theoretical forces at which interface cracks and achieves the bearing capacity, calculated in accordance with *fib* Model Code 2010.

Keywords: concrete composite beam, interface reinforcement, T-shaped beams

1. Introduction

The aim of joining two concrete elements into a one structure is to obtain the quasi-monolithic structure with a load bearing capacity greater than a sum of load capacities of the components. The consideration of such a structure as a quasi-monolithic one is allowed only if the interface between joined elements is correctly arranged. Structural connection provides technological advantages, e.g., enables partial prefabrication or stage production and determines the effectiveness of repairs or enhancements of existing structures. Therefore, it is important to identify the interface stress-strain characteristics, including ultimate load and stress, which causes the interface crack. The influence of these parameters on the static performance of the composite element has already been repeatedly described by researchers in relation to rectangular reinforced concrete elements [1]–[4]; in the rare cases – T-shaped beams [5]–[7].

The authors of this paper have already conducted research on T-shaped composite beams, in which they analysed the influence of the interface location [8], [9] and the influence of variously arranged interface parameters on the static performance of such beams [10]–[13].

This paper describes the development of the previous investigations with the (S2) beams with interface adhesion broken by use of PVE membrane. Two subseries A and B of the S2 series with various interface reinforcement ratios were tested.

The results of the new subseries investigations have been incorporated into a joint analysis, which is presented below. The reported results include: damage mechanism, crack and failure loads, deflections and displacements of components at the end of the element in relation to each other, strain of the main and transverse reinforcement. In addition, the work compares the obtained results with the theoretical values computed in accordance with the guidelines contained in *fib* Model Code 2010.

2. Elements investigated and tests

The T-shaped composite beams with the variously arranged interface, located between the web and flange were tested. Their dimensions were: 1800 mm in span length, 640 x 50 mm flange cross-section, and 80 x 150 mm web cross-section (Fig. 1). The beams were designed to be damaged in the support zones. The procedure of a beam production was divided into two stages. First, the concrete mix forming the web was placed in the mould. After compacting the concrete mix, the contact surface was left in its natural state. The average value of roughness depth was about 4 mm (height from peak to valley) therefore the surface of the interface was classified as “rough”. Next, after 14 days of concrete moisturizing and preparing an “old” concrete surface (by wire brushes to delete the cement milk) the mould was completed with a layer of a “new” concrete. The longitudinal reinforcement consisted of two Ø14 mm bars (the longitudinal reinforcement ratio was 2.21%), while the upper reinforcement consisted of two Ø8 mm bars. Stirrups made of Ø4 mm wires were used.

Five series of beams were performed with the interface arranged as follows:

- BZ/P+S – reinforced interface ($\rho_i=0.21\%$) with adhesion,
- BZ/P – non-reinforced interface with adhesion,
- BZ/S1 – reinforced interface ($\rho_i=0.21\%$) with the surface of the „old” concrete treated using a chemical agent in order to limit the adhesion,
- BZ/S2 – reinforced interface (BZ/S2/A subseries – $\rho_i=0.21\%$, BZ/S2/B subseries – $\rho_i=0.42\%$) with adhesion broken by use of the PVE membrane.

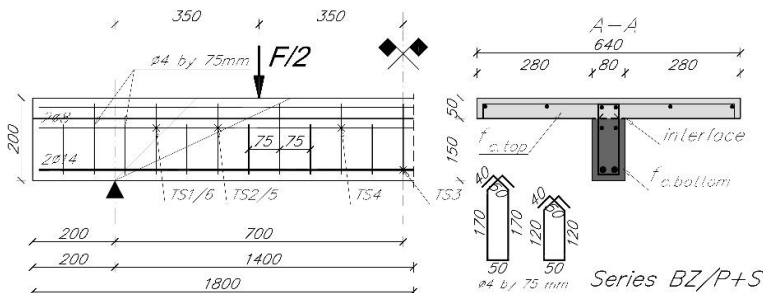


Fig. 1. Details of beams tested: a) longitudinal section, b) cross-sections; TS1/6, TS2/5, TS4 – strain gauges on the stirrups, TS3 – strain gauges on the main bar. *Source:* own study

The beams were tested as simply supported ones in the four-point bending test. In order to ensure stability, the beams were inverted upside down and the load was applied using a rigid traverse (Fig. 2).

In each series, three beams were tested. The load of one beam in each series was constantly increased with 0.5 kN/min rate. For the other beams in the series, the load was stopped at intervals of 10 kN to register the width and pattern of cracks. Deflection and strain of bars were measured automatically by LVTD and strain gauges.

The steel and the concrete parameters of the “bottom” and the “top” layer were conducted using standard laboratory testing methods on reference specimens for each series. Average values of material parameters are listed in Table 1.

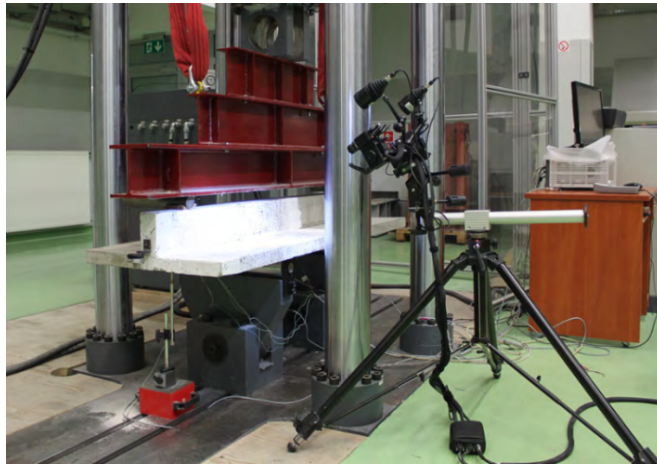


Fig. 2. A view of the beam prepared for the test. *Source:* own study

Table 1. Average values of material parameters. *Source:* own study

	Compressive Strength f_{cm} [MPa]	Tensile Strength f_{ctm} [MPa]	Modulus of Elasticity E_{cm} [GPa]
BZ/P+S			
Bottom	47.01	3.57	35.00
Top	44.37	3.36	34.40
BZ/P			
Bottom	48.87	3.43	35.41
Top	41.54	3.18	33.73
BZ/S1			
Bottom	45.55	3.04	34.67
Top	42.76	3.06	34.02
BZ/S2/A and BZ/S2/B			
Bottom	57.25	3.56	37.13
Top	54.72	3.49	36.63
Stirrups yield stress f_{ywm} [MPa]			340
Longitudinal reinforcement yield stress f_{ym} [MPa]			545
Modulus of elasticity of reinforcement E_s [GPa]			200

3. Test results

3.1. Crack pattern and failure mechanism

The cracks morphology was investigated by documenting the cracks appearance on two beams of each series. Each of them was described and measured by the Brinell microscope. Measurements were made at each load step. Characteristic crack patterns for representative beams from various series after failure were shown in Fig. 3 and 4.

The cracking process, in all beams, began from vertical cracks, which appeared in the web. The first ones were located under the applied load, the next ones appeared in the zone of a constant moment. As the load increased, the diagonal cracks appeared, and they began to dominate the cracking process.

The largest widths were reached by the first diagonal cracks. Until the diagonal crack reached the interface (the load was about 70 kN) the crack pattern in all series looked similar.

Later, in the BZ/P+S series a local crack in the interface was observed, which propagated into the flange towards the support next. Beams of BZ/P series (without reinforcement) were characterized by violent delamination along the whole interface, after a diagonal crack reached it. At the point of load application in the flange, a vertical crack was formed which increased with the diagonal crack, despite the force drop below the value causing the interface crack.

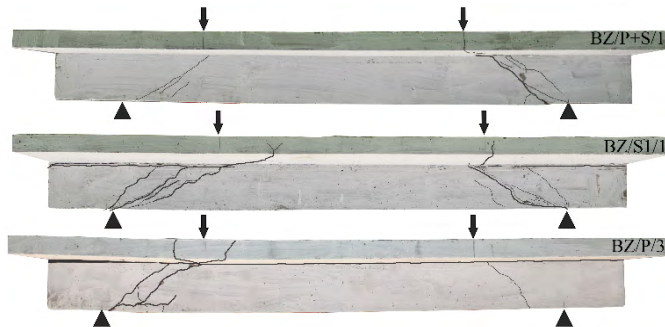


Fig. 3. Crack pattern of representative beams of the BZ/P+S, BZ/S1, and BZ/P series after failure. *Source:* own study

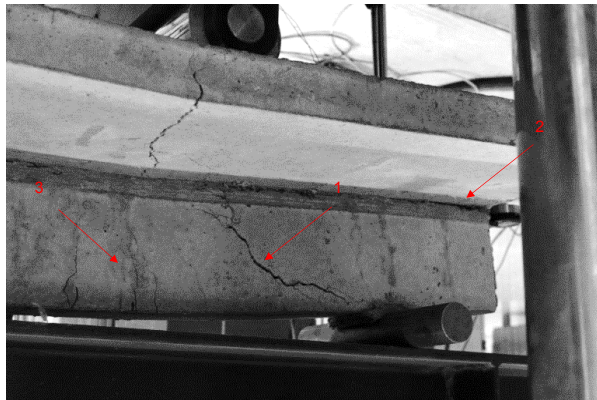


Fig. 4. Crack pattern of BZ/S2/B series with $\rho_i=0.42\%$: 1 – diagonal crack, 2 – interface crack at the end of the beam, 3 – perpendicular cracks at the place of load application. *Source:* own study

In the BZ/S1, BZ/S2/A, and BZ/S2/B series, where adhesion was limited or broken, the interface crack occurred just in the beginning of loading process and developed from the ends of the beams to the supports, joining the diagonal cracks upon reaching the interface. The static performance of the S1 and S2 series was very similar, however, due to the mechanical adhesion, the S1 series was characterized by higher values of the failure loads. In beams with broken adhesion, and with a higher joining reinforcement ratio (BZ/S2/B series), there were significantly more vertical cracks under the load locations and in the constant moment zone. These cracks as well as the diagonal cracks propagated and increased their width throughout the test to create a mixed failure mode – bending with shearing (Fig. 4).

In BZ/P, BZ/S1 and BZ/S2 series of beams displacement of the flange and the web in relation to each other took place. It was measured using manual gauges with accuracy up to 0.01 mm located at the ends of the beam. Fig. 5 shows the relationship between the displacement and the applied load. Beams with adhesion and without joining reinforcement (BZ/P series) were characterized by a rapid increase of displacement at the moment of the interface crack and its intense growth with a slight increase of load. In series with joining reinforcement, but without adhesion (BZ/S1 and BZ/S2 series), the displacement of the components occurred, practically from the beginning of the loading process until the beam failure has been observed. Larger displacements usually occurred on the failure side of the beam. In the BZ/S1 series (with limited adhesion) at the load of approximately 80 kN, and in the BZ/S2 series (with broken adhesion) at the load of 40 kN (displacement was greater than the sensor range) was observed. The maximum displacement in beams with limited and broken adhesion was practically the same, observed at the load about 120-130 kN, but higher joining reinforcement ratio of the B-series caused that this displacement was growing up gently while on the curve corresponding to the A-series the rapid increase in displacement are visible.

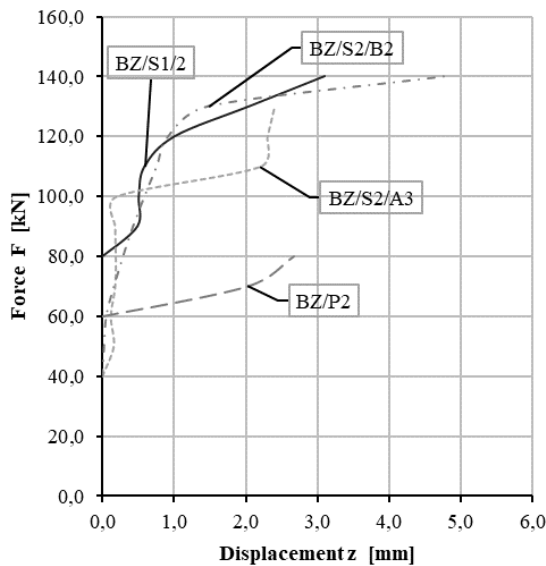


Fig. 5. Transverse displacement of the flange and the web in relation to each other on the beam end (a larger one from left and right side of the beam). Source: own study

The main reinforcement strain chart (Fig. 6) shows that only bars of the BZ/S2/B series (broken adhesion, greater joining reinforcement ratio) have reached the yield point, which has a direct effect on the mixed mode of failure (failure due to shear with bending). Under the same adhesion conditions the beams BZ/S2/A series (lower joining reinforcement ratio) the yield strength was not reached, the beam was failed by a shear. In the BZ/P+S series (adhesion with joining reinforcement) the main reinforcement strain increased linearly and reached the highest load value. Also, in the BZ/P series of beams without joining reinforcement, a linear increase in strain was observed. It took place until the interface failed and was manifested by a rapid load decrease without strain increase. Next, the temporary relaxation of steel and resumption of the main reinforcement work in a separated part of the beam were observed.

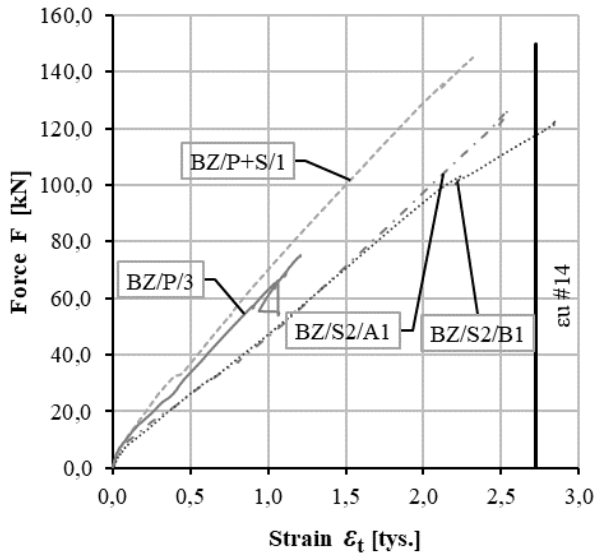


Fig. 6. Strain of the main reinforcement versus applied load, Ts3 strain gauge; ϵ_u #14 – strain value corresponding to the yield strength of the main reinforcement. *Source*: own study

3.2. Deflection

Deflection was measured using linear variable differential transformer gauges (LVTD) located in the middle of the beam span and also at the ends for calibration purpose. Fig. 7 shows a summary of deflection versus applied load curves representative for the beams of each series.

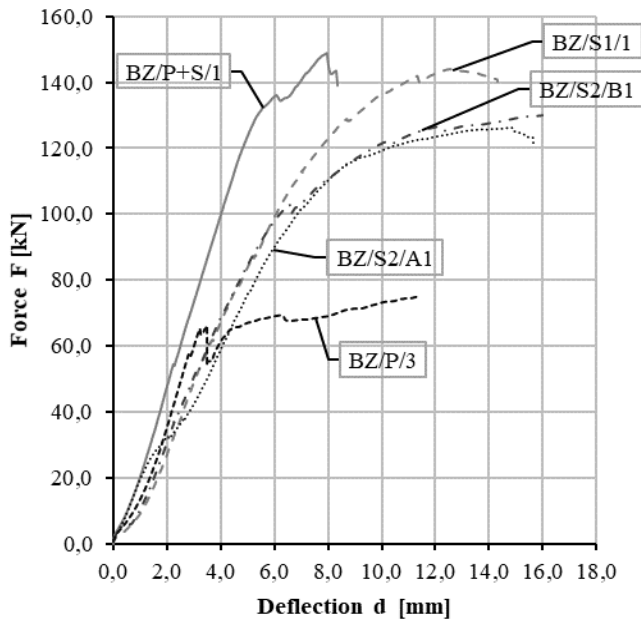


Fig. 7. Representative beams deflection from each series tested. *Source:* own study

The curve clearly shows the moment of the interface delamination of BZ/P series, manifested by a sharp drop in the load with a large increase in deflection.

In the BZ/P+S series there was also a drop of the curve but under higher load and deflection. This indicates the role of the stirrups. The “drop” was followed by enhancement – the successive activation of stirrups took place.

BZ/S1 and BZ/S2 beams reached the highest deflection. In BZ/S1 series adhesion was limited by the use of anti-adhesive agents, which did not completely remove the adhesion (this is confirmed by the analysis of deflection). On the other hand, in the BZ/S2 series, in which adhesion was broken by PVC membrane, the deflections are higher with simultaneous reduction in the failure force.

3.3. Strain of the stirrups

The stirrups strain gauges were located in the interface level on the outside of the perimeter as shown in Fig. 1.

Comparing the stirrups strains and deflections of the beams in each series (Fig. 8), it can be observed that the characteristic points on the deflection diagrams at the moment of strain increase in the stirrups correspond to each other. It is shown with arrows in Fig.8.

In the beams of BZ/P+S series, the strain increases in the stirrups (Ts2, Ts5) begins at a force of about 55 kN, at which we can also observe the drop of the deflection curve. This can be identified with local interface crack. In further stages of loading, the stirrups strain in the support zone of BZ/P+S beams increase until the yield strength is reached. It is observed that the subsequent stirrups covered by a diagonal crack are engaged and the strain increases

until the beam fails by shear. Value of the ultimate load of the beam is equal to the value of the load causing the yield of all last stirrup in the constant.

Attention should be paid to the performance of the transverse reinforcement in the support zone in the BZ/S2 series (broken adhesion), in which from the beginning of loading process there is an increase in strain noticeable. From subsequent charts it follows that as the load increases, further stirrups are activated. There is no uniform distribution of forces in the interface, so the stirrups reach the yield strength in sequence. In the BZ/S2/A and BZ/S2/B series, the first stirrup reaches the yield strength at the same load (~90 kN), then the next second one is activated, etc. Because there are more stirrups on the interface length in the BZ/S2/B series (higher reinforcement ratio) it allows beam performance at higher loads, until the yield strength of the main reinforcement is fully exploited. Characteristic for the BZ/S1 and BZ/S2 series is also activation of the stirrups (Ts4) in the constant moment zone. Stirrups in the other beams achieved low levels of strain values in this zone.

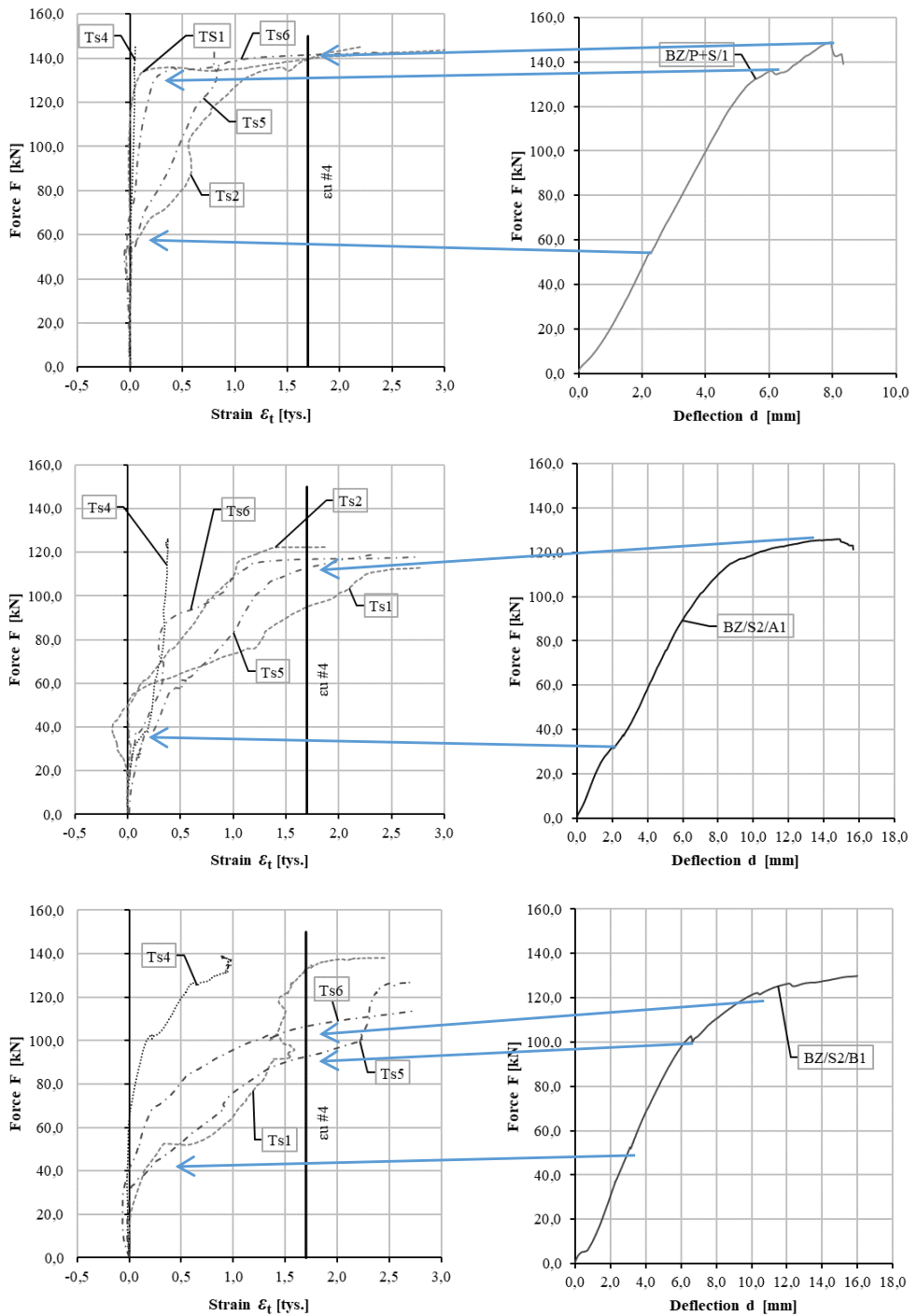


Fig. 8. Comparison of the reinforcement strain and deflection from each series tested; Ts1, Ts2 – stirrups on the left side, Ts4 – stirrup in the constant momentum zone, Ts5, Ts6 – stirrups on the right side, $\epsilon_{u\#4}$ – strain corresponding to the yield strength of stirrups. Source: own study

4. Analysis of the results

4.1. Dependence between interface crack pattern and failure mechanism of beam

The crack pattern of the beams indicates that interface cracks arise at its various places and depend on the distribution of internal forces in the interface (values of normal and tangential stresses) and on the way the interface was arranged.

In the beams of the BZ/P+S series (with guaranteed adhesion and joining reinforcement), the crack in the interface appeared on a short length, at a load value of 47–51% of the ultimate load. It was a part of the diagonal crack. Then it passed into the flange and the beam was failed by shear in the support zone.

In the BZ/S1 and BZ/S2 series (reinforced interface with limited or without adhesion), the interface cracking process was characterized by delamination at the beam ends in the initial loading stage. The observed phenomenon was caused by tensile stress, normal to the contact surface, arising at the ends of simply supported beams in the four-point bending test. By using PVE membrane, the chemical adhesion of the concrete was broken and the tensile normal stress prevented the activation of mechanical adhesion. Joining reinforcement remained the main factor resulting in the interface ultimate load. In the support zone, the distribution of interface forces (shear and compression) and the existence of the transverse reinforcement allowed the transfer of loads as a result of mechanical adhesion and the phenomena of shear friction and dowel action. Despite the delamination of the ends and cracking of the interface over a considerable length, the beams still carried loads but underwent various forms of failure. Depending on the reinforcement ratio in the support zone, in BZ/S2/A series ($\rho_i=0.21\%$), shear failure occurred and in BZ/S2/B series ($\rho_i=0.42\%$), beams were failed in a mixed way by bending combined with shear.

The BZ/P series (guaranteed adhesion, no joining reinforcement) beams behaved differently. After the cracking stress was reached, the load bearing capacity of the interface was lost on the entire length. The beams were destroyed violently by the interface delamination.

Thus, depending on how the interface was formed, the crack pattern and the static performance of the composite depends.

4.2. Ultimate load service of the interface according to fib Model-Code2010

Using the classical equations of the layered structure theory, in order to comparison with the data obtained from the tests, the transverse force corresponding to the interface crack and its bearing capacity was calculated according to formula (1):

$$V_{Rdi} = \tau_{Rdi} \cdot b_j \cdot \frac{\Delta_{11} \cdot (E_p J_p + E_n J_n)}{w_0} \quad (1)$$

$$\Delta_{11} = \frac{1}{E_p A_p} + \frac{1}{E_n A_n} + \frac{w_0^2}{E_p J_p + E_n J_n} \quad (2)$$

where: w_0 – is the distance between the centroids of connected layers, E_{cp} , A_p , J_p and E_{cn} , A_n , J_n – the modulus of elasticity, the cross-sectional area and moment of inertia of “new” and “old” concrete, respectively.

Using the methodology of the pre-standard *fib* Model Code 2010, based on the lesser of the compressive strength of the components $f_{ck,min}$ and the joining reinforcement ratio, the interface ultimate load was calculated. The interface in this standard is treated as non-rigid when the reinforcement degree $\rho_i \geq 0.05\%$. Such conditions correspond to the interface of the BZ/P+S, BZ/S1 and BZ/S2 series. Then the ultimate shear stress τ_{Rdi} is calculated according to the formula:

$$\tau_{Rdi} = c_r f_{ck}^{1/3} + \mu \sigma_N + \rho \kappa_1 f_{yd} (\mu \sin \alpha + \cos \alpha) + \kappa_2 \cdot \rho \sqrt{f_{yd} \cdot f_{cd}} \quad (3)$$

where μ – friction coefficient in the interface, α – the angle of the joining reinforcement to the surface of the interface, ρ – the joining reinforcement ratio, f_{yd} – yield strength of the joining reinforcement, f_{cd} – compressive strength of concrete under triaxial loading conditions, κ_1 and κ_2 – coefficients, which take into account the fact that the joining reinforcement is subjected to the shear and bending simultaneously, and the relation of these stresses depends on the displacement (slip) in the interface.

In the case of the rigid interface (non-reinforced or if $\rho_i \leq 0.05\%$), which corresponds to the BZ/P series, the limit shear stress τ_{Rdi} is described by the equation:

$$\tau_{Rdi} = c_a f_{ctd} + \mu \sigma_n \quad (4)$$

where c_a – coefficient dependent on the roughness of the surface, μ and σ_n – as in the formula (3).

The transverse forces corresponding to the interface ultimate load are summarized in Table 2. In order to allow the comparison of calculated and tested loads, the characteristic values of concrete compressive f_{ck} and tensile $f_{ctk,0.05}$ strength as well as steel yield f_{yk} stress, assessed on the basis of Table 1, are applied in equations (3) and (4). The characteristic value of the adhesion component $c_r f_{ck}^{1/3}$ was calculated regarding safety coefficient $\gamma_{coh} = 2,0$ according to [14].

The most reliable series in the context of interface ultimate load is BZ/P, because its ultimate load depends only on adhesion, without additional effects resulting from the use of joining reinforcement. Achievement of the interface ultimate load (interpreted as contact delamination over the entire length) is equal to the ultimate load of the entire beam.

In the other examined beams, the point of the yielding stress in stirrup as the achievement of the interface ultimate load was set.

The above observations show that the standard calculation models for the interface ultimate load are applicable to elements subjected to longitudinal shearing alone rather than beams working mainly under combination of shear and bending. The local interface ultimate load, understood as the achievement of the yielding stress in one stirrup, does not cause failure of the beam because the next stirrup (further from the support) is turned on; moreover, there is less transverse force, so it can be loading again until the yielding stress in the second stirrup will be reached.

In addition, significant discrepancies in the tested and theoretical values may result from the fact that the interface ultimate load was calculated under the standard assumptions of the values of the factors c_a and c_r , moreover, without taking into account the friction from normal stresses σ_n . This indicates the main problem in the description of the behavior of reinforced concrete composite beams and, consequently, in the design of such beams. This problem is the lack of a precise description of the stress state prevailing in the interface of elements working in different schemes and imprecise values of the coefficients. To describe the actual behavior

of the beam, it is therefore necessary to determine the appropriate values of coefficients and to know the complex stress state prevailing in the interface.

Table 2. Comparison of the forces causing failure and the standard values calculated according to *fib* Model Code 2010. *Source*: own study

Series	Interface parameters (rough surface)						Force F [kN] corresponding to:			
	c_a	γ_{coh}	c_r	μ	σ_n [MPa]	κ_1	κ_2	Interface Ultimate Load		Beam failure
								<i>fib Model Code 2010</i> *	Examined	Examined***
BZ/P	0.4	-	0.7	0.0	-	-	19,0	78.0	78.0	
								72.0	72.0	
								68.0	68.0	
BZ/P+S	-	0.2	0.7	0.0	0.5	0.9	24,0	126.0**	136.0	
								-	149.0	
								142.0**	142.0	
BZ/S1	-	0.2	0.7	0.0	0.5	0.9	23,6	91.0**	143.2	
								98.0**	137.5	
								86,0**	127.3	
BZ/S2/A	-	0.2	0.7	0.0	0.5	0.9	25,8	95,0**	126.0	
								90,0**	112.0	
								103,0**	113.0	
BZ/S2/B	-	0.2	0.7	0.0	0.5	0.9	36,2	93,0**	138.0	
								110,0**	138.0	
								108,0**	134.0	

* characteristic and design values from equations (3) and (4) assessed on the basis of Table 1

** force F corresponding to level of the yielding stress achieved locally in the stirrup of the interface

*** force F exerted by the testing machine until stop of increase was observed

5. Conclusions

Based on the studies and analyses carried out, it can be stated that:

1. Achieving the yield strength of successive stirrups in the joint may indicate that the local interface ultimate load has been reached, however, it does not determine the beam ultimate load.
2. The standard models for the interface ultimate load calculation are applicable to elements subjected to longitudinal shearing alone rather than beams working mainly under combination of shear and bending. The achievement of the yielding stress in stirrup assumed in this model as the reason of joint failure means the local failure only. Then the next stirrup is turned on and the increase of load is possible.
3. The examination of beams with limited or broken adhesion in the interface allowed to conclude that:
 - a. Joining reinforcement remained an important factor resulting in the interface ultimate load in non-rigid connection. This reinforcement allows the transfer of loads between connected parts due to the phenomena of shear friction and dowel action. Despite the delamination in the interface the beams still carried loads but underwent various forms of failure.
 - b. In beams with a higher joining reinforcement ratio (BZ/S2/B series), there were significantly more vertical cracks under the load locations and in the constant moment zone than in the BZ/S2/A beams with lower reinforcement

ratio. Increasing the joining reinforcement ratio may change the failure mode. The BZ/S2/A series beams (lower joining reinforcement ratio) failed by shear, whereas in the BZ/S2/B series the mixed mode of failure (failure due to shear with bending) was observed.

- c. Higher joining reinforcement ratio of the B-series caused that displacement of connected parts in relation to each other was growing up gently while on the curve corresponding to the A-series the rapid increase in displacement was observed.
- d. In spite of the eliminated adhesion in the interface of the BZ/S2/B series (with higher degree of the stirrups) the ultimate load was achieved similar to the level obtained by the beam with adhesion in the interface.


References


- [1] Halicka A., *Studium stanu naprężeń i odkształceń w płaszczyźnie styku i strefie przypodporowej elementów zespolonych z udziałem betonów skurczowych i ekspansywnych*. Wydawnictwo Politechniki Lubelskiej, Lublin, 2007.
- [2] Gromysz K., "Distribution of forces in composite concrete slab between the joint and the reinforcement anchored on the support", in *Concrete and Concrete Structures 2013 Conference Procedia Engineering*, 65, 2013, pp. 206-211.
- [3] Kmiecik P., Kamiński M., "Modelling of reinforced concrete structures and composite structures with concrete strength degradation taken into consideration", *Archives of Civil and Mechanical Engineering*, vol. 11, no. 3, 2011, pp. 623-636.
- [4] Sadowski G., Wiliński P., "Badanie wpływu ukształtowania styku na ugięcie żelbetowych belek zespolonych", *Inżynieria i Budownictwo*, vol. 4, 2017, pp. 206-210.
- [5] Tan K.H. et al., "Horizontal Shear Strength of Indirectly Loaded Composite Concrete Beams", *ACI Structural Journal*, 1999, pp. 533-538.
- [6] Mahmoud M.A., Elafandy T.H., Okail H.O., Abdelrahman A.A., "Interfacial shear behavior of composite flanged concrete beams", *HBRC Journal*, vol. 10, 2014, pp. 206-214. <https://doi.org/10.1016/j.hbrj.2013.11.001>
- [7] Cavaco E., Pacheco I., Camara J. "Detailing of concrete-to-concrete interfaces for improved ductility", *Engineering Structures*, vol. 156, 2018, pp. 210-223. <https://doi.org/10.1016/j.engstruct.2017.10.058>
- [8] Jabłoński Ł., "Wpływ położenia styku na wysokości żelbetowych elementów zespolonych o przekroju teowym na stan graniczny zarysowania styku", *Budownictwo i Architektura*, vol. 13, no. 3, 2014, pp. 95-102. <https://doi.org/10.35784/bud-arch.1770>
- [9] Halicka A., Jabłoński Ł., "Shear failure mechanism of composite concrete T-shaped beams", in *Proceedings of the Institution of Civil Engineers – Structures and Buildings*, vol. 169, no. 1, 2016, pp. 67-75. <https://doi.org/10.1680/stbu.14.00127>
- [10] Halicka A., Jabłoński Ł., "Styk między betonami układanymi w różnym czasie – parametry i nośność według fib Model Code 2010", *Inżynieria i Budownictwo*, vol. 7, 2015, pp. 346-350.
- [11] Jabłoński Ł., "Numerical analyses and laboratory testing of concrete composite T-shaped beams without interface adhesion", in *AIP Conference Proceedings*, 1922(1), 2018. <https://doi.org/10.1063/1.5019139>
- [12] Jabłoński Ł., "Numerical analyses of concrete composite T-shaped beams with variously arranged interface", in *Proceedings of the 12th International PhD Symposium in Civil Engineering*. Prague, Czech Republic, 2018, pp. 441-448.

- [13] Jabłoński Ł., Halicka A., “Influence of surface based cohesive parameters on static performance of concrete composite T-shaped beams”, *MATEC Web of Conferences*, vol. 262, 2019, pp. 1-7. <https://doi.org/10.1051/mateconf/201926208003>
- [14] Randl N., Wicke M., “Schubübertragung zwischen Alt- und Neubeton”, *Beton und Stahlbetonbau*, vol. 95, no. 8, 2000.

Nonlinear analysis of lightweight aggregate concrete columns

Ewelina Kołodziejczyk¹, Tomasz Waśniewski²

¹ Department of Concrete Structures; Faculty of Civil Engineering, Architecture and Environmental Engineering; Lodz University of Technology; 6 Politechnika Avenue, 90-924 Lodz, Poland; ewelina.kolodziejczyk@p.lodz.pl  0000-0002-3533-4145

² Department of Concrete Structures; Faculty of Civil Engineering, Architecture and Environmental Engineering; Lodz University of Technology; 6 Politechnika Avenue, 90-924 Lodz, Poland; tomasz.wasniewski@p.lodz.pl  0000-0001-7303-4920

Abstract: The paper presents a numerical analysis of deformability and load-bearing capacity of lightweight aggregate concrete (LWAC) elements subjected to bending with axial force. The nonlinear material model of LWAC presented in Eurocode 2 (EC2) was assumed. Several different densities and compressive strengths of concrete were taken into account. The investigations included the comparison of the sectional capacity and the behaviour of slender elements made with normal and lightweight aggregate concrete. It was observed that density-dependent mechanical properties of concrete affect the obtained values of the maximum axial force and the bending moment despite the same mean compressive strength. In every case, the capacity of the RLWAC section was lower than the one of normal weight, which was caused by a linear characteristic of the LWAC. Other important factors were the modulus of elasticity and the ultimate strain of concrete. LWAC with the higher density and the lower ultimate strain gave greater stiffness to slender columns but reduced the cross-sectional capacity. It was concluded that the elastic modulus and the peak strain of LWAC which are applied in columns calculations should be verified experimentally.

Keywords: lightweight aggregate concrete, columns, second-order effects

1. Introduction

Lightweight aggregate concrete (LWAC) in structural applications is usually identified with its brittle behaviour that is an unfavourable feature in reinforced concrete structures. It is also associated with low elastic modulus, which causes high deformations. All these parameters play an important role in the performance of slender elements subjected to bending with axial force. However, experimental data concerning the problem of second-order effects in LWAC columns is rare in literature and concerns a narrow scope of the issue. In [1] the extensive

research on the confining effect of transverse reinforcement on the behaviour of reinforced concrete columns is presented. The elements were made with 60 MPa concrete with a fresh density of 1920 kg/m^3 . Second-order effects were also analyzed, but the columns had relatively low slenderness $\lambda = 21$. Papers [2], [3] show the results of an experimental and numerical analysis of columns with slenderness $\lambda = 28$, but they were made with LWC concrete produced with polystyrene foam.

This work aimed to show the behaviour of LWAC columns (cross-section and slender elements) considering different densities and strength of the concrete, and a wide range of slenderness. Numerical analysis of deformability and load-bearing capacity of this kind of elements led in line with Eurocode 2 [EC2, 4] requirements, was presented.

2. Properties of LWAC

Lightweight aggregate (LWA) and concrete mixture additives available today enable the production of LWAC with a strength comparable to traditional concrete as well as its use in structural applications. The properties of LWAC are specified in the EC2 (section 11) [4]. The code concerns concrete strengths from 17 to 88 MPa (f_{icm}) and allows to estimate its modulus of elasticity E_{icm} and ultimate strain ε_{ic1} , which are dependent on its mean compressive strength f_{icm} and oven-dry density ρ . The density of LWAC considered in the analysis should be between 1000 and 2200 kg/m^3 . The nonlinear model of concrete presented in EC2 based on LWAC characteristic was assumed as a starting point for the considerations presented below. Three different levels of the concrete strength were taken (33 MPa, 53 MPa, and 78 MPa). It was needed to define the range of density for each type of concrete to determine the deformation characteristic of the material. There is no information about the correlation between concrete strength and its oven-dry density in EC2. However, it is known that f_{icm} tends to increase as the unit weight increases [5], [6]. The effect was presented in the Fig. 1 (on the left).

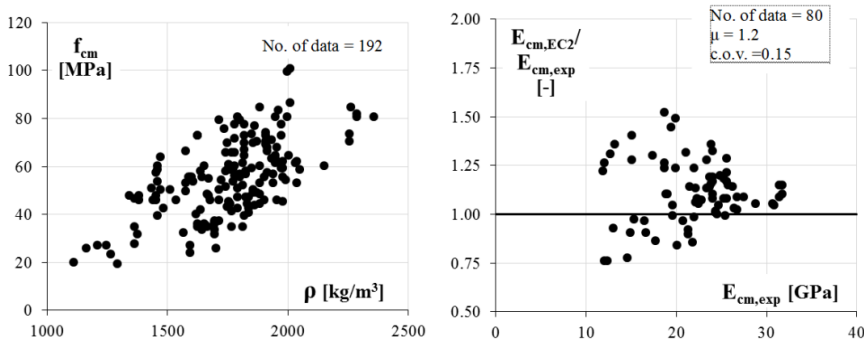


Fig. 1. Mean compressive strength vs oven-dry density of LWAC (on the left). Measured and calculated (EC2) values of modulus of elasticity (on the right). *Source:* [6]

Based on the experimental data (Fig. 1, on the left), it was determined that the minimum density for concrete with the strength f_{icm} of 33 MPa could be taken as 1200 kg/m^3 , and 1500 kg/m^3 and 1800 kg/m^3 for 53 MPa and 78 MPa respectively. Material properties of concrete with the strength and the dry concrete density varied from about 20 to 60 MPa and from 1200 to 1600 kg/m^3 , respectively are also presented in [7] and [8].

Concrete stress-strain EC2 [4] nonlinear models for different concrete strengths defined according to the above assumptions were depicted in Fig. 2. Calculated values of the modulus of elasticity and the strains at the peak stress were presented in Table 1.

Further conclusions presented in [6] indicate, however, that EC2 expressions for modulus of elasticity in most cases of the analyzed data present higher values than the experimental results (Fig. 1, on the right) The differences reach 50% and the average value is 20%. Similar conclusions can be found in [9].

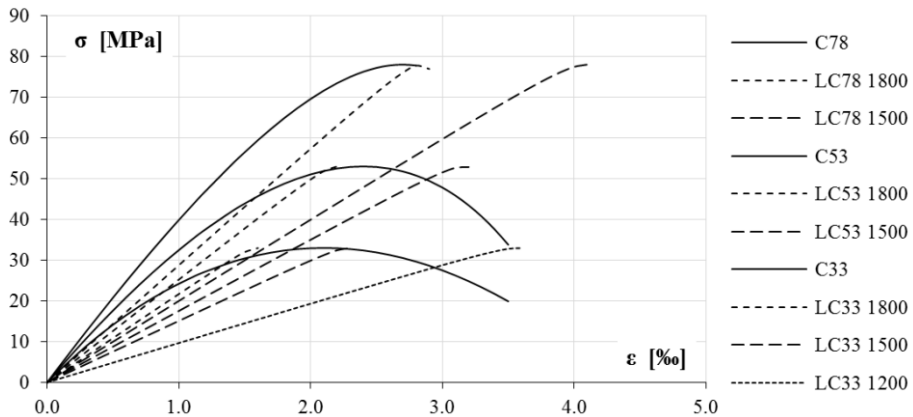


Fig. 2. Concrete stress-strain law. Source: own study

Table 1. Concrete properties

Symbol	Density	Concrete strength	Modulus of elasticity	Strain at the peak stress	Ultimate strain
	kg/m ³	MPa	GPa	%	%
C33	2400	33	31.0	2.10	3.50
LC33 1800	1800	33	20.8	1.59	1.59
LC33 1500	1500	33	14.4	2.29	2.29
LC33 1200	1200	33	9.2	3.58	3.58
C53	2400	53	36.0	2.40	3.50
LC53 2100*	2100	53	32.8	1.62	1.62
LC53 1800	1800	53	24.1	2.20	2.20
LC53 1500	1500	53	16.7	3.17	3.17
LC53 1200*	1200	53	7.2	7.39	7.39
C78	2400	78	41.0	2.70	2.80
LC78 1800	1800	78	27.5	2.84	2.84
LC78 1500	1500	78	19.1	4.09	4.09

* only in selected calculations, to show the tendency

Fig. 3 shows experimental results of high-strength lightweight concrete tests presented in [10]. It can be noticed that strain at the 90% compressive stress for concrete strength of about 80 MPa (Mix 6, 8, 9) can reach about 4%. The value corresponds to that for LC78 1500 concrete (Table 1), which was originally not to be included in the analysis (too low density for this level of strength). In the experimental research, the mentioned specimens had concrete density

1715 kg/m³, 1764 kg/m³ and 1886 kg/m³ and the modules of elasticity 21.6 GPa, 22.2 GPa, and 24.8 GPa respectively.

Due to these inconsistencies, to show the influence of providing material with the stiffness similar to the one obtained in [10], the analysis also included concrete with the strength f_{icm} of 78 MPa and the density of 1500 kg/m³. Moreover, in the selected calculations presented below to depict more general tendency also concrete with the strength f_{icm} of 53 MPa and the density of 1200 and 2100 kg/m³ were considered (Table 1).

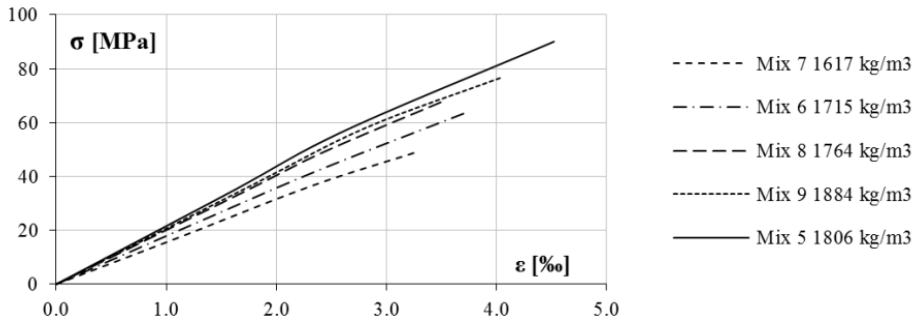


Fig. 3. Experimental stress-strain curves of LWAC at 90% of the ultimate load. Source: [10]

The presented experimental diagram (Fig. 3) confirms, however, the linear model of the LWAC concrete model established by the authors of EC2 [4]. Doubts related to the determination of the modulus of elasticity and strain at the ultimate stress calculated on its basis. For this reason, it is particularly important to verify the effect of the type of concrete on load-bearing capacity, as well as the differences between different LWAC densities to determine the sensitivity to the possible inaccuracy of the module estimation.

3. Modelling assumptions

The parametric study focused on the influence of LWAC material properties acc. to EC2 on the cross-sectional capacity and structural behaviour of reinforced concrete members considering different values of concrete strength, slenderness, and eccentricity of force.

The parametric analysis was conducted in OpenSees, an open-source finite element software for simulating the nonlinear response of structural elements.

ElasticMultiLinear material was used as the stress-strain law for concrete. The nonlinear stress-strain relationship is given by a multi-linear curve that is defined by a set of points which were calculated acc. to EC2 nonlinear model (Fig. 2) for different strengths and densities of concrete. Steel01 bilinear steel material without hardening was applied in relation to the main reinforcement. Concrete tensile strength was not included.

Square cross-section of the column was analyzed as fibre section (Fig. 4, on the left). The section height was 500 mm. It was symmetrically reinforced with 2% total reinforcement ratio (in selected cases also 0.5% and 4%). The yield strength of steel was assumed as 500 MPa ($\epsilon_y = 2.5\%$).

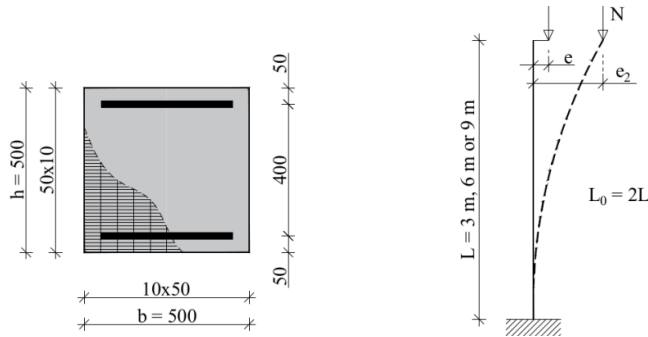


Fig. 4. Fibre cross-section of the element (on the left). Static scheme of the cantilever column (on the right). Source: own study

NonlinearBeamColumn elements modelled reinforced concrete members. Corotational coordinate transformation [11] was used to consider the geometric nonlinearity of the model. The static scheme of a cantilever column under eccentric loading was studied (Fig. 4b). The buckling length ($L_0 = 2L$) was either 6 m, 12 m or 18 m, which corresponds to three slenderness cases $\lambda = 42, 83,$ and 125 . In slender members calculations the two relative eccentricities of the force $e/h = 0.05, 0.25$ were considered.

4. Cross-sectional capacity

The first part of the analysis concerns the load-bearing capacity of the cross-section. There are relative values of axial force N/bh , and bending moment M/bh^2 presented. The results were depicted in the form of N/bh - M/bh^2 interaction diagrams in relation to different concrete strengths. The ultimate points ($M/bh^2, N/bh$) were determined as maximum values of internal forces obtained from cross-sectional capacity calculations in the range of permissible strain, for LWAC the values were always reached at ultimate strain.

The results of the analysis for the section made of concrete with the mean compressive strength of 53 MPa were presented in Fig. 5.

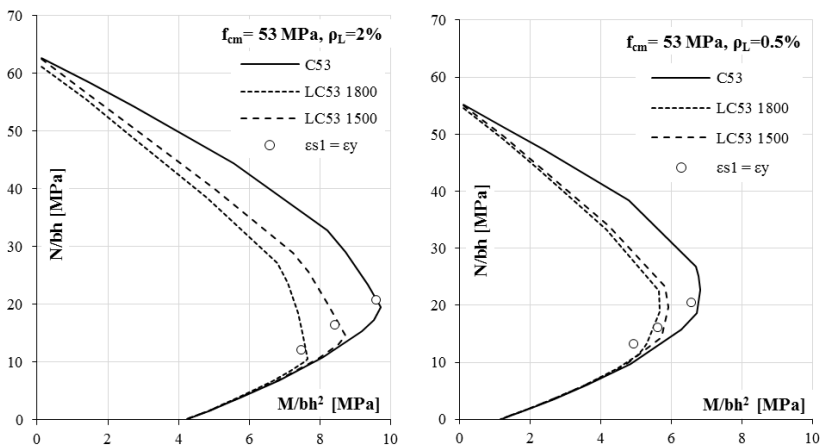


Fig. 5. Interaction diagrams for concrete sections with the strength f_{cm} of 53 MPa, different densities and total reinforcement ratio of 2% (on the left) and 0.5% (on the right). Source: own study

Two cases (Fig. 5) of total longitudinal reinforcement ratio were analyzed – 2% (on the left) and 0.5% (on the right). In each case, three different concrete densities were considered. From both interaction diagrams, we can see that concrete properties connected with its density slightly affect the capacity at axial compression. Small difference, which can be noticed in the case of LC53 1800 concrete at high reinforcement ratio, appears due to the strain achieved in the steel. LC53 1800 concrete has the ultimate strain of 2.2‰. Therefore, bars do not reach its yield strength, and the force corresponding to the reinforcement is lower than for the other types of concrete. The same situation occurs at low reinforcement ratio, but the share of the steel in the load capacity is minimal, so the effect is not visible.

Another interesting part of diagrams is at small relative axial forces (below 10 MPa) and high bending moments where all the curves in the diagrams overlap. To explain this behaviour, points corresponding to the first point where the tensile reinforcement reaches its yield strain ε_y were introduced (Fig. 5). When this point is passed for the least deformable concrete section, the type of concrete does not affect the load capacity. The same internal force values, however, do not mean in this case the same strain in the section, which is connected with different deformability of the considered concrete type.

The most significant difference in the results appears at a relatively high axial force at mid-height of the diagram. The comparison of the results for the two reinforcement ratios (Fig. 5) indicates that there is more than one reason for varying the maximum forces. The first issue is the character of the concrete model. The nonlinear ascending branch of the model, corresponding to normal weight concrete caused, higher load capacity in comparison to any LWAC concrete, which is characterized by linear behaviour. This effect is visible on both interaction diagrams. Another reason is the influence of the reinforcement. As it can be seen at the small reinforcement ratio (Fig. 5, on the right) results for the two LWAC concretes are close to each other – the steel governs slight part of the load capacity. It changes when we increase the reinforcement ratio (Fig. 5, on the left). In this case, the value of the ultimate strain of LWAC concrete decides about the result. A lower load capacity of the section made with concrete with higher density (LWAC53 1800) and the lower ultimate strain 2.2‰ than the one with the lowest density (LWAC53 1500) and the ultimate strain 3.2‰ can be observed.

The case of mean compressive strength of 33 MPa and 78 MPa was also considered to expand the scope of the observations, (Fig. 6).

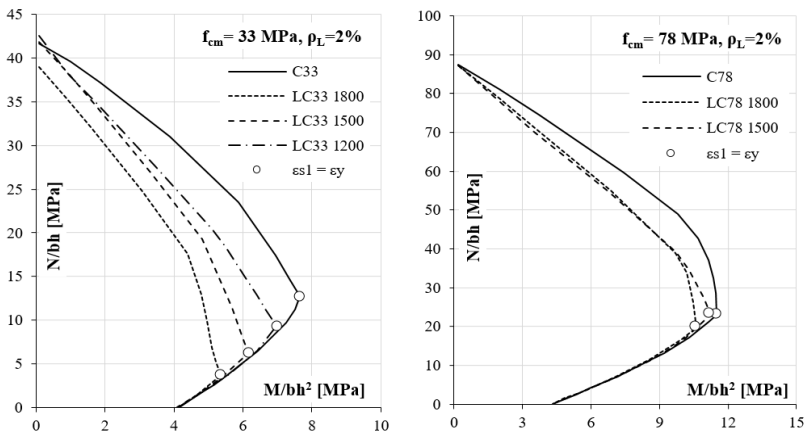


Fig. 6. Interaction diagrams for concrete sections with 2% total reinforcement ratio for different densities of concrete with the strength f_{cm} of 33 MPa (on the left) and 78 MPa (on the right). *Source:* own study

The interaction diagrams for f_{cm} of 33 MPa (Fig. 6, on the left) show a similar tendency to the previous case ($f_{cm} = 53$ MPa). The most significant reduction of load-bearing capacity comparing to normal weight concrete was obtained for LC33 1800 concrete. First of all, there is an apparent decrease in the maximum axial force. It is due to the very low ultimate strain for this kind of concrete, which is 1.6%. In this situation, the stress in the reinforcement is much lower than its yield strength, which reduces the total sectional capacity not only for axial compression but also in other cases when there is a bending moment as well. Moreover, it can be noticed that the point with maximal moment is very low. For the other LWAC types (1500 kg/m³ and 1200 kg/m³) results are more proximate to normal weight concrete as the ultimate strain increases.

In Fig. 6 (on the right), the diagrams for the highest compressive strength were presented. The calculation, the same as in the previous case, was conducted for 2% reinforcement ratio. In this case, the share of the reinforcement in the capacity is correspondingly lower, so the differences between the two LWAC concrete results are small. The other reason for this outcome is the fact that for all three cases of 78 MPa concrete, the ultimate strain exceeds the yield strain of steel. Besides, because the model of normal weight high strength concrete is closer to the linear than the lower concrete grades, the results of the interaction curves do not vary as much.

To show the more general tendency determined in the analysis, according to the results for concrete with compressive strength of 53 MPa, a diagram presented in Fig. 7 was prepared. In this case, the range of concrete density considered in the calculations was extended. The densities of 1200 kg/m³ and 2100 kg/m³ were included. Additionally, the 4% reinforcement ratio was also considered.

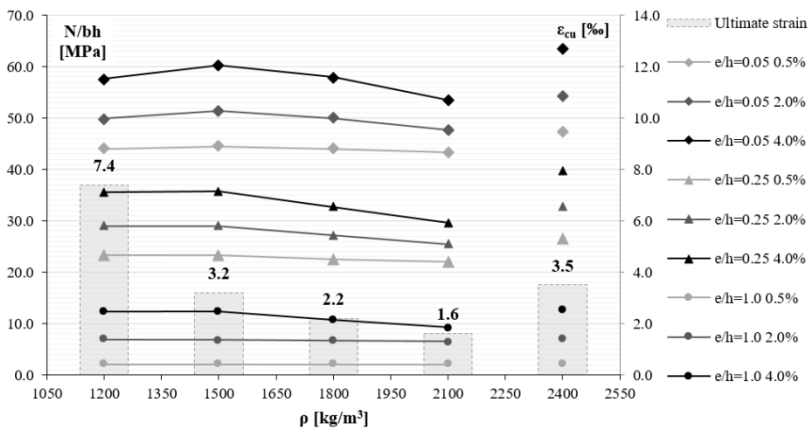


Fig. 7. The influence of concrete density on an ultimate axial force (the left axis) at different eccentricities and reinforcement ratios, the ultimate strain for concrete with the strength f_{cm} of 53 MPa for different densities (the block diagram – the right axis). *Source:* own study

The chart includes two vertical axes. The axis on the left refers to the value of the axial force in individual cases; the axis on the right represents the deformation values shown using a block diagram. Different cases of the reinforcement ratio (0.5%, 2% and 4%) and the relative eccentricity of force e/h (0.05, 0.25, 1.0) were considered. The results for normal weight concrete were given separately on the right ($\rho = 2400$ kg/m³).

The maximum forces for LWAC in all additional cases are lower than the ones obtained for C53, which confirms previous conclusions. The differences between the results for assumed

LWAC types are more significant, as the ratio of the reinforcement increases. The extension of the analysis showed another interesting conclusion. The results for the highest eccentricity of the force (close to pure bending) show that at the reinforcement ratio of 4% a reduction of the maximum axial force for concrete density below 1800 kg/m^3 should be expected, which was not observed in Fig. 5 and Fig. 6. The less ductile behaviour of the strongly reinforced section and the very low ultimate strain caused steel does not to reach the yield strain, and the force was decreased.

In Fig. 7, it can also be noticed that the ultimate strain increases faster when going towards low densities, which results from the method of determining it in EC2, and for 1200 kg/m^3 high value of 7.2‰ is obtained. At the same time, in the case of low eccentricity, a decrease in the force is observed. This effect is associated with the strain level in the section and its curvature. As a result of the analysis of the forces in the cross-section, it can be stated that the share of concrete decreases with its stiffness (E_{icm}), the simultaneous increase in strain compensates for this effect by increasing the force in steel with a surplus. This effect reaches its maximum when steel obtains the yield range and then decreases. Hence the loss of the load-bearing capacity for concrete with a density of 1200 kg/m^3 .

5. Column capacity

In the second part of the parametric study, the authors focused on the second-order response of the elements. The calculations were conducted until the concrete reached its limit strain (in one case in Fig. 8, on the right, the analysis for the highest slenderness was finished at 0.2 m). It was limited to the case of 53 MPa compressive strength.

The curves plotting normal force against total bending moment and second-order deflection for rigidly connected cantilever columns are presented below.

The two values of the relative force eccentricity e/h 0.05 and 0.25 were considered. Results for the lower force eccentricity and different cases of the column slenderness are presented in Fig. 8.

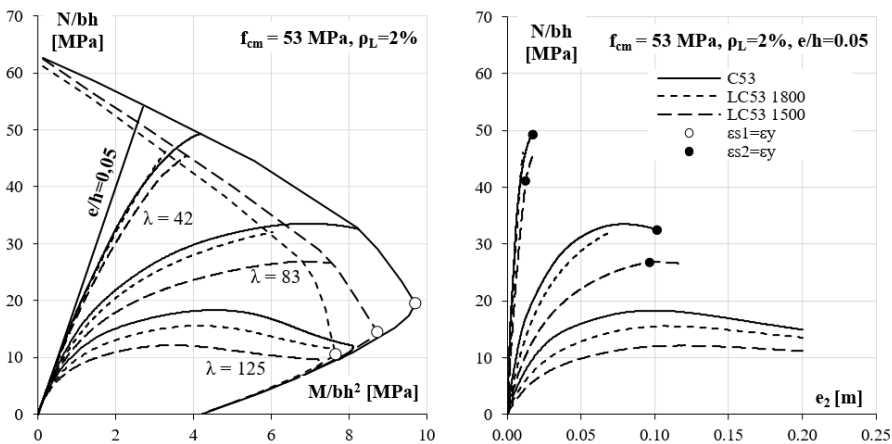


Fig. 8. N - M (on the left) and N - e_2 (on the right, e_2 – second-order deflection) relationships for columns made with concrete with the strength f_{icm} of 53 MPa at different densities with different slenderness λ (relative eccentricity – $e/h = 0.05$, 2% total reinforcement ratio). Source: own study

The diagrams (Fig. 8) show that for all concrete types, the influence of second-order effects become more significant with the increase of the slenderness. Interestingly, although in the previous part of the analysis lower density of concrete related to higher sectional capacity, second-order effects have reversed this trend for columns, which is visible in all slenderness cases. For the low slenderness $\lambda = 42$, slight values of the displacement were obtained, however still for concrete with the lowest density (LC53 1500) the lowest maximum force was recorded. The same situation was observed for columns with higher slenderness. In all cases, the column stiffness resulting from the modulus of elasticity E_{icm} determined the final load capacity. It can be seen in both $N-e_2$ diagrams (Fig. 8 and 9) that for each level of normal force the second-order deflection was the higher, the lower the modulus of elasticity of the concrete that caused the highest second-order moments and the most significant reduction of the maximum normal force in the case of LC53 1500. It is worth adding that LWAC did not exhibit significantly higher maximum deflection; in all cases, it was slightly higher for LC53 1500 and even lower for LC53 1800 comparing to C53.

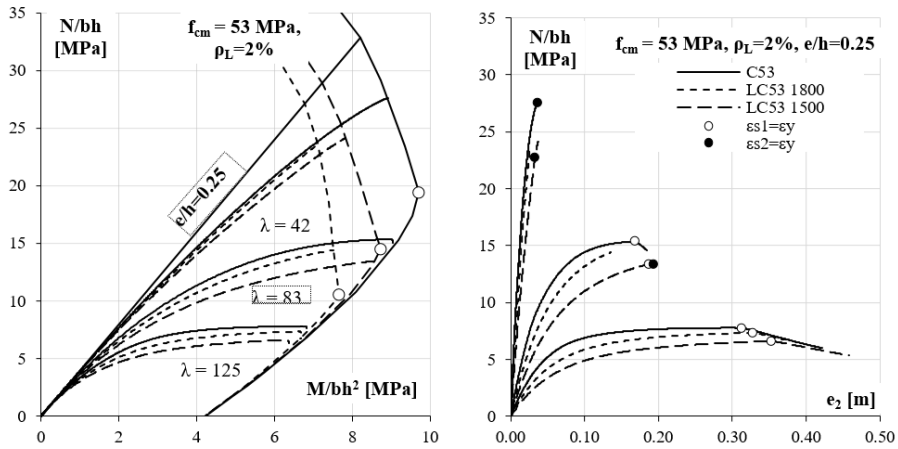


Fig. 9. $M-N$ (on the left) and $N-u$ (on the right, e_2 – second-order deflection) relationships for columns made with concrete with the strength f_{icm} of 53 MPa at different densities with different slenderness λ (relative eccentricity – $e/h = 0.25$, 2% total reinforcement ratio). Source: own study

The case of the higher eccentricity of the force is presented in Fig. 9. This time, when we consider column with the lowest slenderness ($\lambda = 42$) the ultimate normal force was still higher for LC53 1500 (than 1800) but for more slender elements the force for this concrete was the lowest.

6. Conclusions

Sensitivity analysis has been conducted to show the influence of a density-dependent mechanical properties of concrete on the load-bearing capacity of sections and slender elements subjected to bending with axial force.

It was revealed that the characteristics of LWAC concrete, its modulus of elasticity and the ultimate strain significantly affect the capacity (M, N) despite the same mean compressive strength. It was determined that lightweight concrete could not be used as a substitute for concrete with normal weight considering only its compressive strength.

The calculations of the cross-sections showed that in the case of normal weight concrete for all considered compressive strengths (33 MPa, 53 MPa, 78 MPa) higher values of the maximum axial force and bending moment were reached comparing to any analyzed LWAC type due to its nonlinear behaviour preceding the maximum stress. Differences in the results for different LWAC types were also observed. The LWAC sections with the lower density of concrete and the higher ultimate strain obtained higher curvature and strain in the reinforcement, which led to the increase in the capacity, in most cases.

The trend observed in the sectional calculations of the LWAC was reversed when geometric nonlinearity was taken into account. Columns made with concrete with the lowest modulus of elasticity (LC53 1500) reached the greatest second-order deflection, which caused the most significant reduction of the maximum normal force and as a consequence, the least result from all analyzed concrete types.

The above conclusions indicate great sensitivity of the obtained results of the load-bearing capacity of this kind of LWAC elements to the assumed density dependant material properties. Therefore, the formulas for the modulus of elasticity [4] referring to LWAC and, as a result, the peak strain, because it has almost linear behaviour, should be considered only as the first approximation, because the modulus is significantly affected by various variables, such as moisture or the type of aggregate. Slender columns should be considered as elements where deflections are of great importance, and in this case, modulus of elasticity should be determined experimentally.

References


- [1] Galeota D., Giammatteo M.M., Gregori A., “Ductility and strength in high-performance, lightweight concrete columns”, in *13th World Conference on Earthquake Engineering*, no. 3414, Vancouver, 2004.
- [2] Tawfik M., Elwan S., Seleem H., and Abdelrahman A., “Behavior of lightweight concrete under uniaxial eccentric compressive stresses”, *International Journal of Engineering Research and Development*, vol. 13, no. 9, 2017, pp. 15–27.
- [3] Tawfik M., Elwan S., Seleem H., and Abdelrahman A., “Behavior of lightweight concrete columns under eccentric loads (Parametric study)”, *Al-Azhar University Civil Engineering Research Magazine (CERM)*, vol. 40, no. 1, 2018, pp. 67–81 .
- [4] European Committee for Standardization. EN 1992-1-1, *Eurocode 2: Design of concrete structures – Part 1-1 : General rules and rules for buildings*, vol. 1. Brussels, 2004.
- [5] Lim J. C. and Ozbakkaloglu T., “Stress-strain model for normal- and lightweight concretes under uniaxial and triaxial compression”, *Construction and Building Materials*, vol. 71, 2014, pp. 492–509.
- [6] Galeota D., Giammatteo M.M., Zulli M., “Structural properties of High-Performance Lightweight Concrete”, in *The First International fib Congress, Osaka, 2002*, pp. 247–256.
- [7] Suraneni P., Bran Anleu P.C., Flatt R.J., “Factors affecting the strength of structural lightweight aggregate concrete with and without fibres in the 1,200–1,600 kg/m³ density range”, *Materials and Structures*, vol. 49, 2015, pp. 677–688. <https://doi.org/10.1617/s11527-015-0529-2>
- [8] Rossignolo A., Agnesini M. V.C., Morais J.A., “Properties of high-performance LWAC for precast structures with Brazilian lightweight aggregates”, *Cement & Concrete Composites*, vol. 25, 2003, pp. 77–82.
- [9] Costa H., Julio E., and Lourenco J., “Lightweight Aggregate Concrete – Codes Review and Needed Corrections”, in *Codes in Structural Engineering. Developments and Needs for International Practice*, Dubrovnik, 2010.

-
- [10] Zhang M.-H., Gjørsv O.E., “Mechanical Properties of High-Strength Lightweight Concrete”, *ACI Materials Journal*, no. 88, 1991, pp. 240–247.
- [11] M. D. Denavit and J. F. Hajjar, *Description of geometric nonlinearity for beam-column analysis in OpenSees*. Boston, 2013. <http://hdl.handle.net/2047/d20003280>


Analysis of precast lintel behaviour in AAC masonry walls confined by reinforced lightweight and ordinary concrete

Wojciech Mazur¹, Tomasz Rybarczyk²

¹ Department of Building Structures; Faculty of Civil Engineering; Silesian University of Technology;
Akademicka 2 Street, 44-100 Gliwice, Poland;

wojciech.mazur@polsl.pl  0000-0001-6382-1496

² SOLBET Sp. z o.o. Toruńska 71 Street, 86-050 Solec Kujawski, Poland;

tomasz.rybarczyk@solbet.pl  0000-0003-1431-9533

Abstract: This paper presents the test results of reinforced precast lintels made of autoclaved aerated concrete (AAC) used to cover window openings in walls made of AAC masonry units. Walls were confined with reinforced lightweight concrete. The two variants of wall confinement with different way of lintel support and the static diagram of a simply supported beam and a constrained beam were tested. Cracks and deformations of test models around window openings were recorded with the Aramis software for non-contact measurements of displacements. Failure of lintels caused the loss of load capacity of test models. Lintels were cracked in the same way, but the sequence of crack formation and their location were different. The test results were compared with the test made for similar walls confined with ordinary concrete. Additional tie-columns did not significantly affected the load capacity of the test models contrary to the walls confined with ordinary concrete.

Keywords: autoclaved aerated concrete (AAC), precast lintels, Digital Image Correlation (DIC), confined wall, lightweight concrete

1. Introduction

Precast lintels are additional elements in masonry walls in accordance with the standard [1]. Lintels in the wall work with members above them, i.e. masonry units and tie-beams. Reinforced concrete tie-beams can increase the lintel load capacity by about 50%. Due to their stiffness, tie-beams can transfer load from the floor and the masonry wall above, and the lintel is only used as a filler and cover for the opening. Currently, particular importance has been paid to environmentally friendly design and passive buildings with walls that are designed to have the lowest heat transfer coefficient. In extreme cases, reinforced concrete members used in masonry walls create a linear thermal bridge that significantly deteriorates thermal parameters of partition walls. Tie-beams and tie-columns made of lightweight concrete are an alternative that combines

advantages of concrete and good parameters of thermal insulation. According to the standard [2], lightweight concrete is defined as concrete with a dry density within the range of 800-2000 kg/m³. Strength characteristics of lightweight concrete are less favourable when compared to ordinary concrete; thus, lintel becomes more significant as it takes greater loads. According to the standard [3], [4], the concrete used for structural purposes should be characterized by the strength class not lower than C12/15. Lightweight concrete can replace mortar to fill toothing when tying precast walls. The effect of the change in the tie beam strength on lintels was verified during tests on full-scale walls confined with reinforced lightweight concrete. The results of this test were compared with those for walls confined with ordinary concrete.

2. Test models

Experimental tests described in this paper were performed on two types of confined models with a window opening, which were different in structural aspects (geometry, method of confinement, used concrete). The first group consisted of two series of walls confined with lightweight reinforced concrete. The walls confined along their perimeter marked as MSOL-Z1 (Confined Masonry with an Opening) belonged to the first series. The second series included walls that were confined along their perimeter and had additional tie-beams at vertical edges of a window opening. They were marked as M2SOL-Z1 (Confined Masonry with double confinement and an Opening). Two other test series of the second group included the same wall models as in the first group, in which confining elements were made of ordinary concrete. The third series was marked as MSO-Z1, and the fourth one as M2SO-Z1.

All test models of walls were built from AAC masonry units. Blocks had the width of 180 mm and the standard compressive strength f_b of 4.0 N/mm². They were bonded with ready-mixed thin-layer mortar with compressive strength f_m of 6.1 N/mm². Each block had tongues and grooves on its face, so vertical (head joints) were not filled with mortar.

Two types of concrete were used in the test walls. The first type was lightweight concrete made of foam glass-based aggregate, with the density of 900 kg/m³ (density class D 1.0 according to [2]) and the mean compressive strength $f_{c,cube}$ of 10.0 N/mm². The second type of concrete was ordinary concrete made of CEM-I 42.5 R cement, with the strength class C20/25. The cross-section of reinforced concrete elements was 180 x 180 mm, and 180 x 230 mm where toothing occurred. The longitudinal reinforcement of confining elements was composed of bars with a diameter of 10 mm, made from steel of the class A IIIIN, and the transverse reinforcement contained bars with a diameter of 8 mm. According to EC-6 [4-5], confining elements should have a cross-section of not less than 0.02 m² with the smallest dimension not smaller than 150 mm in the wall plane. And the minimum cross-section of longitudinal reinforcement should be 0.8% of the cross-section of a confining element and not smaller than 200 mm². The minimum area of the cross-section of longitudinal reinforcement and confining elements in all models was 314 mm² and 32400 mm² respectively.

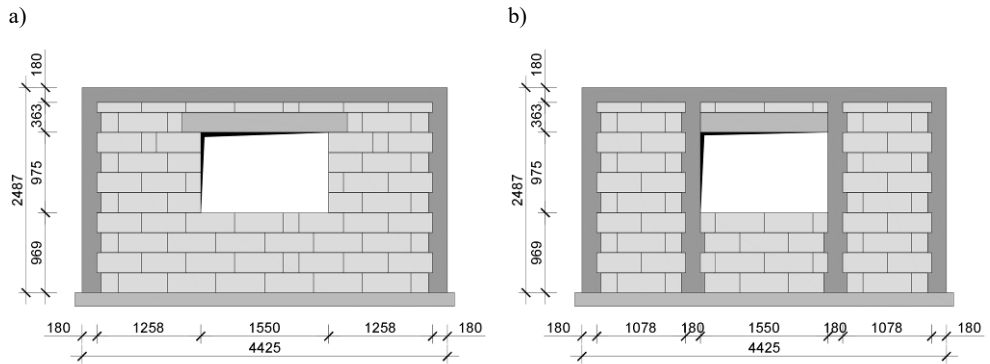


Fig. 1. Models of series: a) MSOL and MSO, b) M2SOL and M2SO. *Source:* the authors' own study

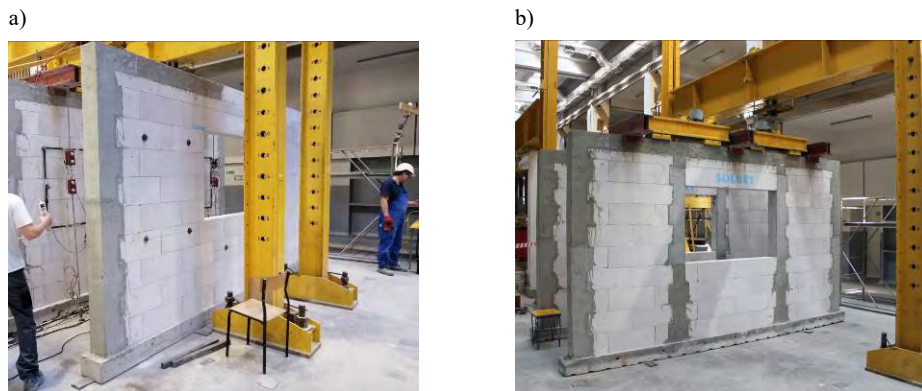


Fig. 2. Models of series: a) MSOL, b) M2SOL. *Source:* the authors' own study

A centrally placed window opening was 1550 mm wide and 975 mm high, which corresponds to the typical width of a window. Reinforced precast lintels made of AAC were used to cover openings. Longitudinal reinforcement of lintels was made of bars with a diameter of 8 mm (three bottom rebars and two top rebars) welded to open stirrups made of rebars with a diameter of 4.5 mm. Tests on lintels are described in the paper [6]. Only one course of masonry units with a height equal to half of the block height was between the lintel and the tie-beam. Dimensions of the test models are shown in Fig. 1, and their photos in Fig. 2.

3. Test stand and testing technique

All the walls were tested at the test stand described in the paper [7]. The test stand and the loading scheme are presented in Fig. 3.

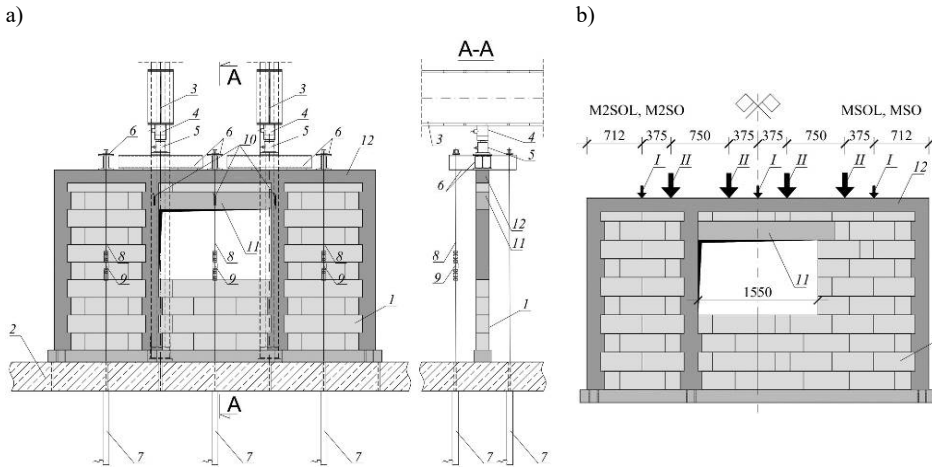


Fig. 3. a) test stand, b) loading scheme. Notations: 1 – AAC masonry units, 2 – reinforced concrete slab, 3 – steel frame, 4 – hydraulic actuator, 5 – dynamometer, 6 – crossbeams, 7 – piston jacks, 8 – steel tendon, 9 – dynamometer, 10 – LVDT, 11 – lintel, 12 – tie-beam and tie-column, *I* – force caused by piston jacks – auxiliary loading, *II* – force caused by hydraulic actuator – a half of main load. *Source:* the authors' own study

The test models were loaded using two types of loading schemes: the auxiliary and main scheme. Three auxiliary schemes were used. Each of them consisted of two actuators mounted under the floor, on which two test models were placed with two tendons and a crossbeam. The actuators mounted on the steel crossbeam, that was supported on the top surface of the tie beam, were used to apply load to the walls through the tendons. One auxiliary scheme was placed in the middle of the test model, and two others were on both sides at the distance of 1500 mm. Each scheme transferred the load of 50 kN and the minor weight of the crossbeam was neglected. The main loading was induced by two schemes, each of them consisted of a steel frame, the actuator and the crossbeam distributing the load to a pair of forces at the distance of 750 mm.

The area around the window opening in each test model was painted on one side with the irregular high-contrast pattern to record displacements with the Aramis software. Deflections in lintels and strain of the masonry wall observed in other parts of the wall and on its other side were recorded with LVDT sensors connected to the automated test stand for measurements. This paper presents the results only for lintels. The models tested at the test stand are shown in Fig. 4.

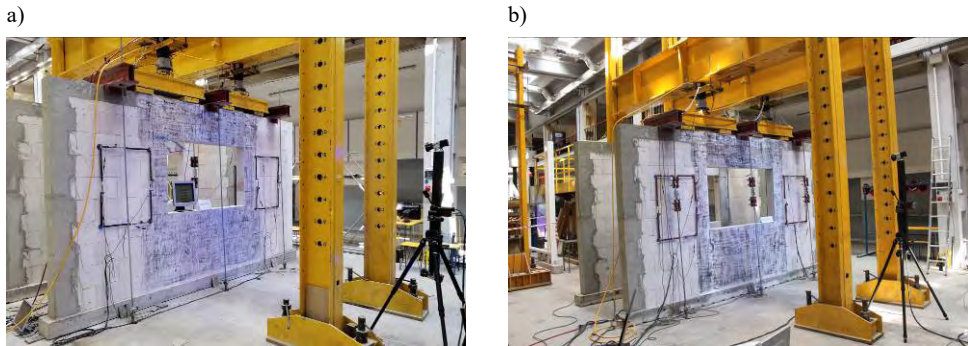


Fig. 4. Models of the following series at the test stand: a) MSOL-Z1, b) M2SOL-Z1. *Source:* the authors' own study

4. Test results

At first the test models were loaded using the auxiliary tendon schemes. Then, the main load was continuously applied until the failure of the model. Images recorded during tests with the Aramis system were processed by GOM Correlate software. Those images were used to determine the development of cracks in the wall around the window opening.

First cracks appeared in the bed joint between the lintel and the masonry units in the models of the series MSOL-Z1. That type of crack was observed in the model MSOL-Z-1-1 under the load of 18.5 kN generated by the auxiliary scheme and at the deflection in the lintel of 0.2 mm (Fig. 5a). Cracking of the bottom edge of the lintel was noticed under the load of 23.9 kN and at the deflection of 0.5 mm (Fig. 5b). A further increase in loading produced cracks propagating towards the top edge of the lintel at the support of the wall (Fig. 5c). When the maximum load transferred by the tendon scheme (load of 50 kN) was reached, deflection in the lintel achieved its limit value $l_{eff}/500$. The continuous main loading produced the maximum load of 142.3 kN acting on the lintel, and the lintel deflection of 20.2 mm (Fig. 5d).

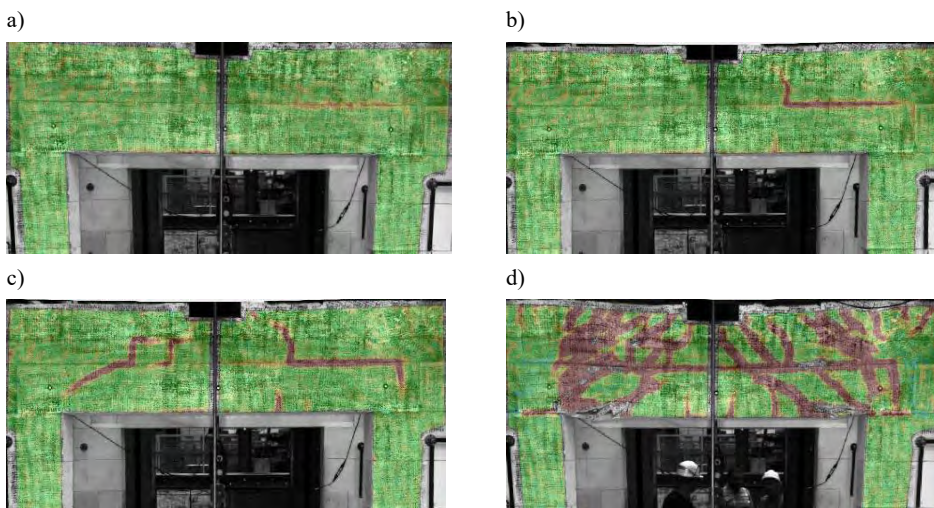


Fig. 5. Crack propagation during tests of the model MSOL-Z1-1. Description in text. *Source:* the authors' own study

As in the previous model, the first crack in the model MSOL-Z1-2 was formed in the bed joint under the load of 26.6 kN and at the deflection of 0.4 mm (Fig. 6a). At a further increase in loading up to 32.7 kN (Fig. 6b), and the corresponding lintel deflection of 0.6 mm, the crack changed into a diagonal crack running to the support edge. Cracking of the bottom edge in the central part of the span was noticed under the load of 35.3 kN and at the deflection of 0.76 mm (Fig. 6c). The limit load exerted on the lintel was reached under the load of 86.1 kN. The maximum load applied to the lintel was 140.0 kN, and the corresponding deflection was 17.0 mm (Fig. 6d).

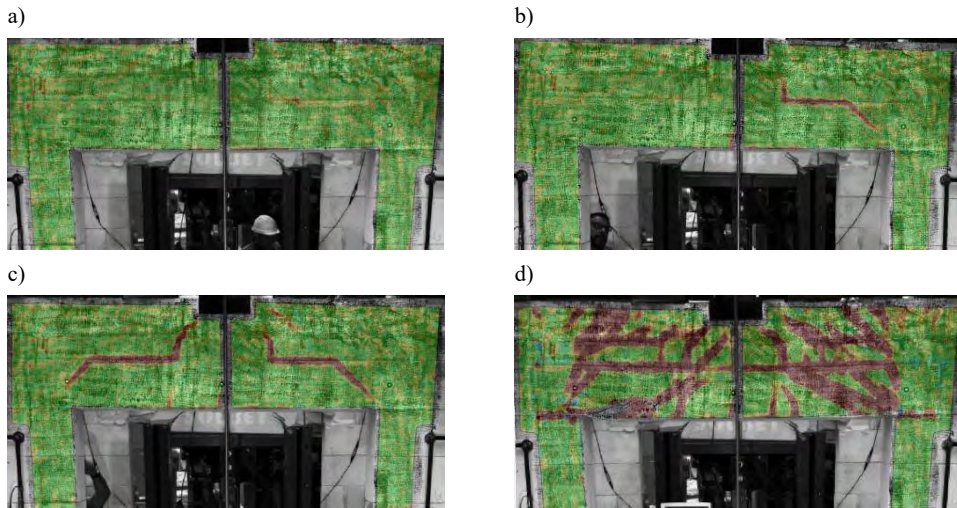


Fig. 6. Crack propagation during tests of the model MSOL-Z1-2. Description in text. *Source:* the authors' own study

As in the models of the series MSOL-Z1, first cracks in the model M2SOL-Z1-1 with additional confining elements were observed in the bed joint between the lintel and the masonry units. Cracks in the model M2SOL-Z1-1 were formed under the load of 15.9 kN and at the deflection of 0.25 mm (Fig. 7a).

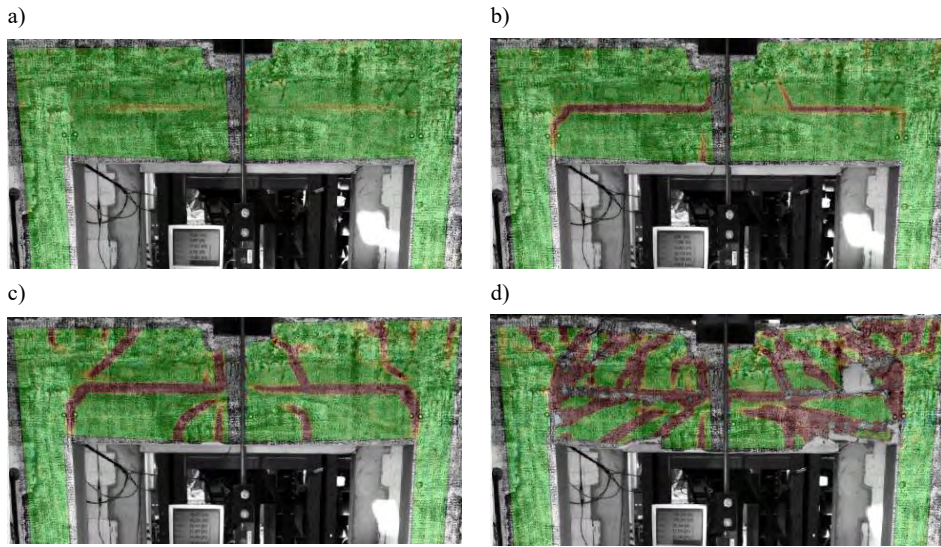


Fig. 7. Crack propagation during tests of the model MSOL-Z1-2. Description in text. *Source:* the authors' own study

Cracking in the lintel anchorage at the reinforced concrete tie-column occurred under the load increasing up to 23.0 kN and at the deflection of 0.4 mm. A crack in the bottom edge of the lintel was noticed under the load of ca. 24.4 kN and at the deflection of 0.6 mm (Fig. 7b). The limit deflection of the lintel was reached under the load of 63.1 kN (Fig. 7c). The lintel failure was observed under the load of 142.7 kN and at the deflection of 13.0 mm. A further loading of the model generated even a greater force of 146.0 kN and the lintel deflection of 27.5 mm (Fig. 7d).

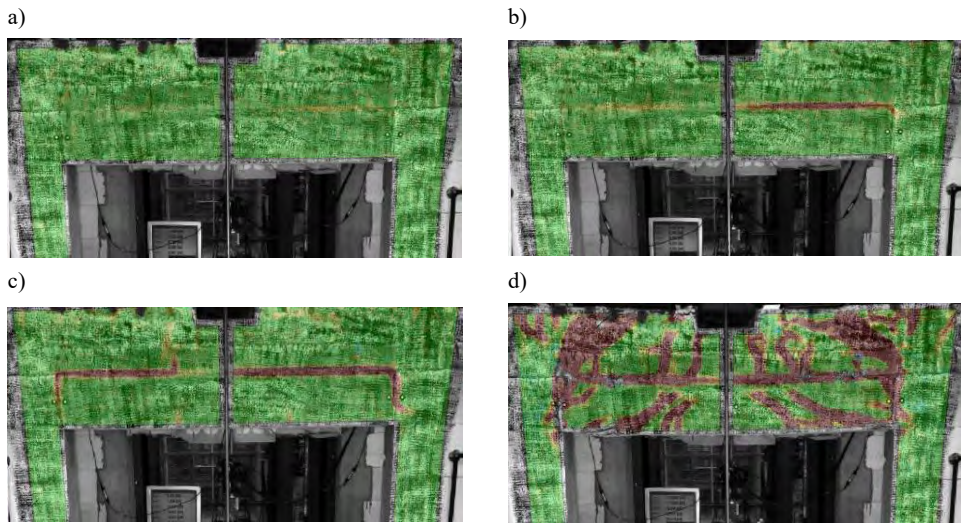


Fig. 8. Crack propagation during tests of the model MSOL-Z1-2. Description in text. *Source:* the authors' own study

The cracking scheme for the model M2SOL-Z2 was similar to the first model. Cracking of the bed joint occurred under the load of 18.0 kN, and the deflection of 0.2 mm (Fig. 8a). Cracking of the vertical edge at the junction between the lintel and the reinforced concrete tie column occurred under the load of 18.5 kN and at the deflection of 0.3 mm (Fig. 8b). The bottom edge of the lintel cracked under the load of 29.5 kN and at the deflection of 0.9 mm (Fig. 8c). The maximum load exerted on the lintel was 150.6 kN (Fig. 8d), and the corresponding deflection was 15.1 mm. The test was discontinued when the load reached 147.9 kN, and the deflection was equal to 27.1 mm.

The models cracked and were destroyed in a similar manner regardless of the type of concrete. A view of final cracks in the models of the series MSOL-Z1 are shown in Fig. 9 and the models of the series M2SOL-Z1 in Fig. 10.

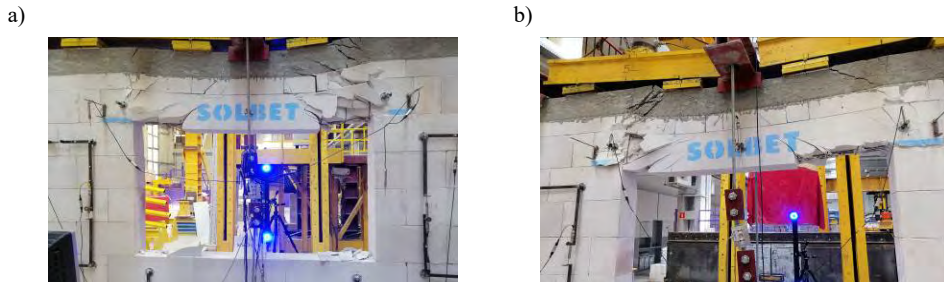


Fig. 9. The upper part of the wall around the window opening in test of the elements of the series MSO-Z1 after tests: a) model 1, b) model 2. *Source:* the authors' own study

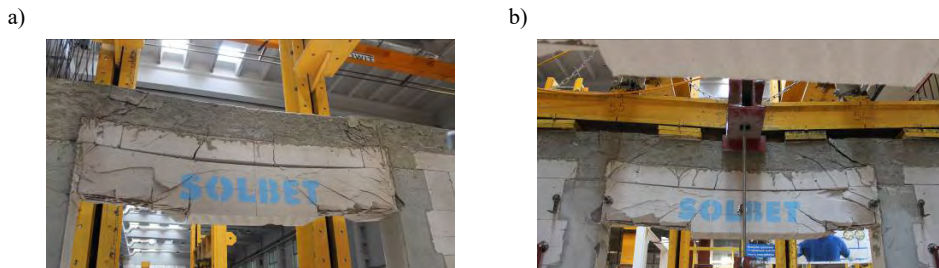


Fig. 10. The upper part of the wall around the window opening in test of elements of the series M2SOL-Z1 after tests: a) model 1, b) model 2. *Source:* the authors' own study

Table 1. Averaged test results for each series. *Source:* the authors' own study

No. of series		Lintel deflection at cracking, mm	Cracking load kN	Lintel deflection at failure, mm	Maximum loading, kN
MSOL-Z1	1	0.5	23.9	20.2	142.3
	2	0.6	32.7	17.0	142.0
M2SOL-Z1	1	0.4	23.0	13.0	142.7
	2	0.3	18.5	15.1	150.6
MSO-Z1	1	0.3	50.0	7.7	206.9
	2	0.4	50.0	18.6	222.5
M2SO-Z1	1	0.7	50.0	7.2	263.6
	2	0.5	50.0	8.7	268.1

Table 1 compares the test results for the walls confined with ordinary and lightweight concrete. There are load values resulting in cracking of the lintel, the maximum values, and the corresponding deflection in the lintel.

5. Analysis of test results

Destructive forces acting on both models of the series MSOL-Z1 were nearly the same, and the average value was 142.1 kN. For the wall models with additional confinement, the destructive forces differed by as little as 8 kN, and their average value was approx. 146.7 kN. The destructive force exerted on the models confined along their perimeter by lightweight concrete was lower by only 3% when compared to the models with additional confinement. This difference was 19% in the case of similar models confined by ordinary concrete. The failure of the models of the series MSOL-Z1 was found under the load corresponding to 66% and 54% of the failure load for the models of the series MSO-Z1 and M2SO-Z1 respectively. For the models of the series M2SOL-Z1, the failure load corresponded to 66% and 55% of the destructive force acting on the models of the series M2SO-Z1 and MSO-Z1 confined with ordinary concrete. The relation between deflection of the lintel and its loading for all experimental models is illustrated in Fig. 11.

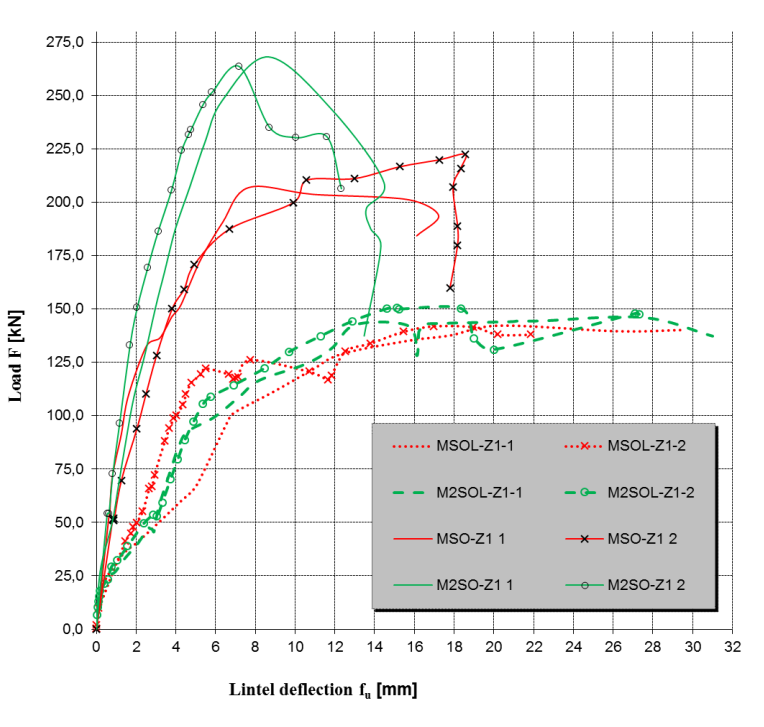


Fig. 11. Load F_y – lintel deflection f_y relationships in models with confined walls. Source: the authors' own study

The morphology of cracks in each model of walls indicated that cracks were at first developed in the bed joint between the lintel and the wall. Then, they appeared in the models of the series M2SOL-Z1 with fixed lintels, at the junction of lintels and reinforced concrete tie-columns, and then in the bottom centre of the lintel. When the bed joints were cracked in

the models MSOL-Z1, diagonal cracks running from the upper edge of the lintel were observed at first. Then cracks developed in the bottom centre of the beam. The reverse sequence of crack formation is also possible. Such scheme suggests a significant impact of the beam over the support, which is neglected in calculations of the load capacity of the lintel and in the reinforcement structure.

Assuming that the wall structure should transfer the load from one floor with the span of 6.0 m, which was represented in the tests by the tendon scheme generating the load, first cracks in the lintels were observed under the load corresponding to 37-65% of the load applied by the floor. At the time of lintel cracking, the deflections were about 10-20% of the limit deflection $l_{\text{eff}}/500$ equal to 3.3 mm.

The analysis of relations between the load and the lintel deflection in the models confined by lightweight concrete indicated there was no sudden drop in the load after reaching the maximum load in contrast to confined models of the series M2SO-Z1.

6. Conclusions

The discussed results of the tests show that, like in the performed tests [8], the most stressed zone of the lintel is its support and ends, and not the central zone which often tends to be considered as the only and most important zone for engineering calculations for lintels. The standardized test of lintels [9] in the scheme of simply supported beam does not represent the behaviour of lintels in the wall, but only during assembly.

The use of additional reinforced lightweight concrete tie-columns along the vertical edges of the window opening in the models confined by lightweight concrete caused an increase in the maximum lintel load by 3%. In the case of the similar wall models confined by ordinary concrete, the reinforced concrete tie-columns increased the load capacity of the walls by 19%. The tests should be repeated on lightweight concrete with a compressive strength of not less than 15 N/mm² to ensure that walls meet standard conditions [3], [4], [10].

References


- [1] 845-2:2013-10 PN-EN: Specification for ancillary components for masonry. Part 2: Lintels.
- [2] PN-EN 206+A1:2016-12 Concrete. Specification, performance, production and conformity.
- [3] PN-EN 1992 -1-1: Eurocode 2 – Design of concrete structures – Part 1-1: General rules and rules for buildings
- [4] PN EN 1996-1-1: Eurocode 6: Design of masonry structures – Part 1-1: General rules for reinforced and unreinforced masonry structures
- [5] Drobiec Ł., Jasiński R., Piekarczyk A., *Konstrukcje murowe według Eurokodu 6 i norm związanych*, vol. 1. Wydawnictwo PWN, Warszawa 2013.
- [6] Mazur W., Drobiec Ł., Jasiński R., “Research of Light Concrete Precast Lintels”, *Procedia Engineering*, vol. 161, 2016, pp. 611-617. <https://doi.org/10.1016/j.proeng.2016.08.711>
- [7] Drobiec Ł., Jasiński R., Mazur W., “Analysis of AAC precast lintels embedded in walls different construction”, *ce papers*. 2018;2:367–376. <https://doi.org/10.1002/cepa.830>
- [8] Mazur W., Drobiec Ł., Jasiński R., “Research and numerical investigation of masonry – AAC precast lintels interaction”, *Procedia Engineering*, vol. 193, 2017, pp. 385-392. <https://doi.org/10.1016/j.proeng.2017.06.228>

-
- [9] PN-EN 1356:1999 Performance test for prefabricated reinforced components under transversal load of autoclaved aerated concrete or lightweight aggregate concrete with open structure
- [10] Rybarczyk T., Drobiec Ł., Jasiński R., Jonderko K., “Ustalenia normowe, praktyczne aplikacje i wybrane badania murowych ścian z elementów murowych z ABK skrzepowanych żelbetem”, in *XXXIII Ogólnopolskie Warsztaty Pracy Projektanta Konstrukcji. Szczyrk 6-9 marca 2018 r.*, vol. 4, pp. 85-107.

Load and resistance factors for prestressed concrete girder bridges

Andrzej S. Nowak¹, Olga Iatsko²

¹ Department of Civil Engineering; Auburn University; Auburn, AL 36849-5337, USA,
nowak@auburn.edu

² Department of Civil Engineering; Auburn University; Auburn, AL 36849-5337, USA
ozi0002@auburn.edu  0000-0001-8380-9515

Funding: This work was supported by the Highway Research Center at Auburn University.

Abstract: There has been a considerable progress in the reliability-based code development procedures. The load and resistance factors in the AASHTO bridge design code were determined using the statistical parameters from the 1970's and early 1980's. Load and resistance factors were determined by first fixing the load factors and then calculating resistance factors. Load factors were selected so that the factored load corresponds to two standard deviations from the mean value and the resistance factors were calculated so that the reliability index is close to the target value. However, from the theoretical point of view, the load and resistance factors are to be determined as coordinates of the so-called "design point" that corresponds to less than two standard deviations from the mean. Therefore, the optimum load and resistance factors are about 10% lower than what is in the AASHTO LRFD Code. The objective of this paper is to revisit the original calibration and recalculate the load and resistance factors as coordinates of the "design point" for prestressed concrete girder bridges. The recommended new load and resistance factors provide a consistent reliability and a rational safety margin.

Keywords: design point, design formula, prestressed concrete girders, resistance factor, reliability index, bridge live load, safety margin

1. Introduction

The basis for the current AASHTO LRFD Code [1] was developed in the 1980's [8]. The major conceptual change from the Standard Specifications [2] was the introduction of four types of limit states and corresponding load and resistance factors.

The basic design formula for structural components in the Standard Specifications [2] is:

$$1.3D + 2.17(L + I) < \phi R \quad (1)$$

where:

D = dead load;

L = live load (HS-20);

I = dynamic load;

R = resistance (load carrying capacity);

ϕ = resistance factor (by default = 1).

On the other hand, the equivalent design formula in the AASHTO LRFD Code [3] is:

$$1.25D + 1.50D_w + 1.75(L + I) < \phi R \quad (2)$$

where:

D_w = dead load due to wearing surface;

L = live load (HL-93);

$\phi = 1$ for steel girders and pre-tensioned concrete girders and 0.9 for reinforced concrete T Beams.

Comparison of Eq. 1 and Eq. 2 indicates that the differences are on the load side only. The role of load and resistance factors is to provide safety margins, i.e. load factors are to increase the design loads so that there is an acceptably low probability of being exceeded. Role of resistance factor is to decrease the design load carrying capacity, to result in an acceptably low probability of exceeding the critical level. However, if $\phi = 1$, then resistance is not reduced and most of the safety reserve is on the load side of Eq. 1 and 2.

Therefore, there is a need to determine values of load and resistance factors that would represent rational and optimum safety margins. The derivation procedure involves the reliability analysis procedure and calculation of the so-called “design point” [10]. The product of load and load factor can be referred to as a factored load, and the product of resistance and resistance factor is a factored resistance. The coordinates of the design point are values of factored load and factored resistance corresponding to the minimum reliability index. The objective of this paper is to calculate the optimum load and resistance factors for selected representative bridge components and then propose a modified design formula to replace Eq. 2.

2. Limit state function and reliability index

For each limit state, a structural component can be in two states: safe when resistance, R , exceeds the load, Q , and unsafe (failure) when load exceeds resistance. The boundary between safe and unsafe states can be represented by the limit state function, in a simple form such as:

$$g = R - Q = 0 \quad (3)$$

Since R and Q can be considered as random variables, the probability of failure, PF , is equal to probability of g being negative,

$$P_{_F} = P \cdot (g < 0) \quad (4)$$

In general, R and Q can be functions of several variables such as dead load, live load, dynamic load, strength of material, dimensions, girder distribution factors, and so on. Therefore, the limit state function can be a complex function:

$$g(X_1, \dots, X_n) = 0 \quad (5)$$

A direct calculation of probability of failure can be difficult, in particular when g is non-linear. Instead, reliability index, β , can be calculated and the relationship between, β , and the probability of failure, P_F , is as follows:

$$P_F g = \Phi(-\beta) \quad (6)$$

and

$$\beta = -\Phi^{-1}(P_F) \quad (7)$$

where:

Φ = cumulative distribution function of the standardized normal random variable;

Φ^{-1} = the inverse of Φ [10].

There are several formulas and analytical procedures available to calculate β . If the limit state function is linear, and all the variables are normal (Gaussian), i.e.

$$g(X_1, \dots, X_n) = a_0 + \sum_{i=1}^n a_i X_i \quad (8)$$

then

$$\beta = \frac{\mu_g}{\sigma_g} \quad (9)$$

where:

$$\mu_g = g(\mu_1, \dots, \mu_n) \quad (10)$$

μ_i = mean value of X_i ;

$$\sigma_g = \sqrt{\sum (a_i \sigma_i)^2} \quad (11)$$

σ_i = standard deviation of X_i .

If the variables are non-normal, then Eq. 9 can be used as an approximation. Otherwise, a more accurate value of β can be calculated using an iterative procedure developed by Rackwitz and Fiessler [17]. However, in practical cases the results obtained using Eq. 9 can be considered as accurate.

If the limit state function is nonlinear, then accurate results can be obtained using Monte Carlo simulations [10].

3. Design point

The result of reliability analysis is reliability index, β . In addition, the reliability analysis can be used to determine the coordinates of the “design point”, i.e. the corresponding value of factored load for each load component and value of factored resistance. For the limit state

function in Eq. 5, the design point is a point in n -dimensional space, denoted by (X_1^*, \dots, X_n^*) , that satisfies Eq. 5, and if failure is to occur, it is the most likely combination of X_1^*, \dots, X_n^* [10].

For example, if the limit state function is given by Eq. 3, and R and Q are normal random variables, then the coordinates of the design point are [10]:

$$R^* = \mu_R - \frac{\beta\sigma_R^2}{\sqrt{\sigma_R^2 + \sigma_Q^2}} \quad (12)$$

$$Q^* = \mu_Q + \frac{\beta\sigma_Q^2}{\sqrt{\sigma_R^2 + \sigma_Q^2}} \quad (13)$$

If R and Q are not both normally distributed then R^* and Q^* can be calculated by iterations using Rackwitz and Fiessler procedure [17]. However, a relatively wider range of design point coordinates corresponds to the same value of reliability index, so in practice, Eq. 12 and Eq. 13 can be used even for non-normal distributions.

4. Statistical Parameters of Load Components

The basic load combination for bridge components include dead load, D , dead load due to the wearing surface, D_w , live load, L , and dynamic load, I . Each random variable is described by its cumulative distribution function (CDF), including the mean and standard deviation. It is also convenient to use the bias factor which is the ratio of mean-to-nominal value, denoted by λ , and the coefficient of variation, V , equal to the ratio of the standard deviation and the mean. Both λ and V are non-dimensional.

The total load is a sum of $D + D_w + (L + I)$. Dead load is time invariant so the only time-varying load components are L and I . In the original code calibration [12], the maximum expected 75-year live load was considered, therefore, the same time period is considered in this paper.

The statistical parameters of dead load that were used in the original calibration have not been challenged so far. Therefore, for factory-made components (structural steel and precast/prestressed concrete) $\lambda = 1.03$ and $V = 0.08$. For the cast-in-place concrete, $\lambda = 1.05$ and $V = 0.10$. For the wearing surface it is assumed that the mean thickness is 3.5in (90 mm) with $\lambda = 1.00$ and $V = 0.25$.

The live load parameters used in the original calibration were based on the Ontario truck survey data [18], with less than 10,000 vehicles, because no other reliable data was available at that time. In the meantime, a considerable weight-in-motion (WIM) database was collected by the FHWA. Therefore, the statistical parameters for live load are taken from the recent SHRP2 R19B report [15]. The processed data included 34 million vehicles from 37 locations in 18 states. For each location, the annual number of vehicles was 1 to 2 million.

Live load is the effect of trucks, therefore, the vehicles in the WIM database were run over influence lines to determine the moments and shears. CDF's of the maximum simple span moments were calculated for 30 ft (9 m), 60 ft (18 m), 90 ft (27 m), 120 ft (36 m) and 200 ft (60 m). For an easier interpretation of the results, the moments were divided by the corresponding HL-93 moments [1]. For the considered locations, the maximum ratios were about 1.35-1.40 of HL-93.

The cumulative distribution functions were extrapolated to predict the mean maximum 75 year moment. The ratio of mean-to-nominal value, or bias factor for live load moment, is plotted vs. span length in Fig. 1 for the average daily truck traffic (ADTT) from 250 to 10,000.

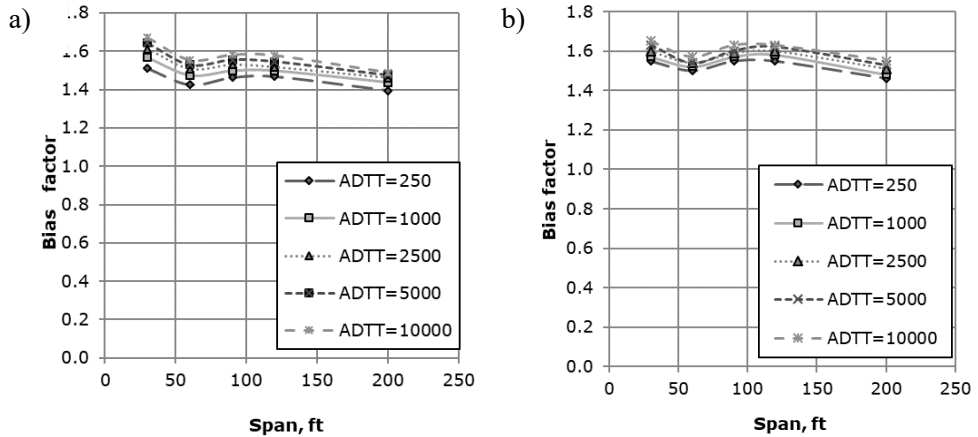


Fig. 1. Bias factor vs. span length for the maximum 75 year: a) moment, b) shear (1ft=3.05 m). *Source:* own study

Field tests showed that dynamic load practically does not depend on the truck weight [9]. Therefore, dynamic load factor decreases for heavier trucks. It is further reduced when a multiple presence of trucks is considered, in particular for side-by-side occurrence [12]. Therefore, in the reliability analysis, the mean value of the dynamic load factor is taken as 0.10.

The coefficient of variation for static and dynamic live load is taken as 0.14. The total load as a sum of several components can be considered as a normal random variable.

5. Statistical parameters of resistance

The load carrying capacity is considered as a product of three factors representing the uncertainties involved in material properties, dimensions/geometry and the analytical model. The statistical parameters, bias factor, λ , and coefficient of variation, V , that were used in the original calibration are listed in Table 1.

Table 1. Statistical parameters of resistance from NCHRP report 368. *Source:* [12]

Material	Moment		Shear	
	λ	V	λ	V
Steel – Non-composite	1.12	0.1	1.14	0.105
Steel – Composite	1.12	0.1	1.14	0.105
Reinforced Concrete	1.14	0.13	1.2	0.155
Prestressed Concrete	1.05	0.075	1.15	0.14

Since the original calibration, a considerable research was performed in conjunction with revision of the ACI 318 Code [13, 14, 16]. The data base included compressive strength of concrete, yield strength of reinforcing bars and tensile strength of prestressing strands. The results pointed out that the material properties are more predictable than 30 years ago. There is a reduction in coefficient of variation because of more efficient quality control procedures. It was observed that compressive strength of concrete has a bias factor of 1.3 for $f'_c = 3000$ psi (21 MPa) and 1.1 for $f'_c = 12,000$ psi (85 MPa), and corresponding coefficient of variation varies

from 0.17 for $f'_c = 3000$ psi (21 MPa) to 0.10 for $f'_c = 12,000$ psi (85 MPa). For reinforcing steel, $\lambda = 1.13$ and $V = 0.03$, and for prestressing strands $\lambda = 1.04$ and $V = 0.015$. These material parameters can serve as a basis for revising the resistance models for bridge components. It is estimated that the mean load carrying capacity of bridge girders is higher by 5 to 10% compared to what was considered in the original calibration. However, since additional analysis is required to develop updated statistical parameters for resistance of bridge components, in this paper, the reliability analysis is carried out using the parameters from Table 1.

6. Representative Design Cases

The reliability indices are calculated for the design cases considered in the original calibration using Eq. 9 [12]. The results are shown in Fig. 2 for prestressed concrete girders, Fig. 3 for reinforced concrete T-beams and Fig. 4 for steel girders. For each material, the analysis is performed for spans: 30, 60, 90, 120 and 200 ft (9, 18, 27, 36 and 60 m), and girder spacing 4, 6, 8, 10 and 12 ft (1.2, 1.8, 2.4 and 3.6 m). For reinforced concrete T-beams the span length was limited to 60 ft (18 m). The analysis was performed for ADTT from 250 to 10,000.

The resulting reliability indices are about 3.5, with a small degree of variation. This is an indication that the code is consistent.

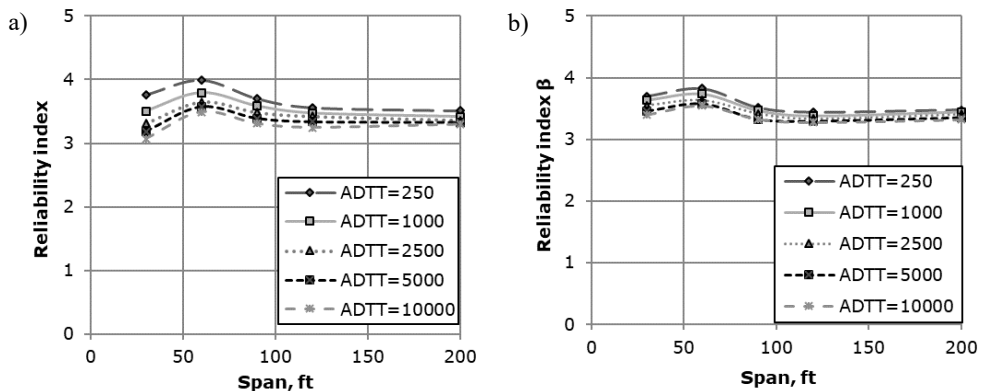


Fig. 2. Reliability index vs. span length for: a) moment, b) shear, for prestressed concrete girders (1 ft = 3.05 m). *Source:* own study

7. Optimum load and resistance factors

The reliability indices are calculated for the design cases considered in the original calibration. For these design cases, the parameters of the design point were also calculated using Eq. 12 and Eq. 13.

For each load component, X , the optimum load factor, γ_X , is (Eq. 14):

$$\gamma_X = \frac{\lambda_X X^*}{\mu_X} \quad (14)$$

where:

λ_X = bias factor of X ;

X^* = coordinate of the design point;

μ_x = mean value of X ;

and for resistance (Eq. 15):

$$\phi = \frac{\lambda_R R^*}{\mu_R} \tag{15}$$

Therefore, for D_1 (weight of factory made elements), the load factor, γ_{D1} , is:

$$\gamma_{D1} = \frac{\lambda_{D1} D_1^*}{\mu_{D1}} \tag{16}$$

for D_2 (weight of cast-in-place concrete), the load factor γ_{D2} is:

$$\gamma_{D2} = \frac{\lambda_{D2} D_2^*}{\mu_{D2}} \tag{17}$$

for D_3 (weight of the wearing surface), the load factor γ_{D3} is:

$$\gamma_{D3} = \frac{\lambda_{D3} D_3^*}{\mu_{D3}} \tag{18}$$

For live load, L , the load factor γ_L is:

$$\gamma_L = \frac{\lambda_L L^*}{\mu_L} \tag{19}$$

The dead load factors calculated using Eq. 16-18 are follows:

- for D_1 , γ_{D1} =1.05-1.1;
- for D_2 , γ_{D2} =1.10-1.17;
- for D_3 , γ_{D3} =1.03-1.

As an example, the dead load factors γ_{D2} load factors are shown in Fig. 3 for prestressed concrete girders.

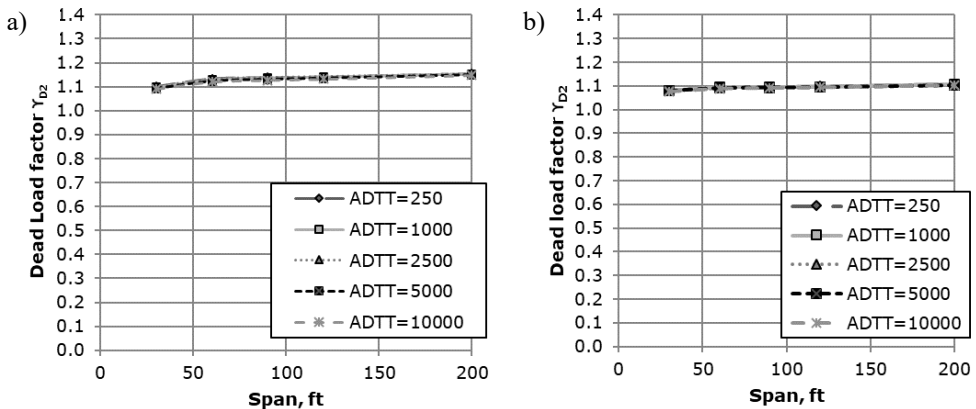


Fig. 3. Dead load factors vs. span length for: a) moment, b) shear, for prestressed concrete girders (1 ft = 3.05 m). Source: own study

The calculated live load factors are shown in Fig. 4 for prestressed concrete girders. For most cases, the optimum live load factor γ_L is between 1.4 and 1.55 for ADTT = 10,000 and the range is 1.3 to 1.5 for ADTT = 250. Therefore, 1.55 can be considered as a conservative value of live load, even for ADTT = 10,000.

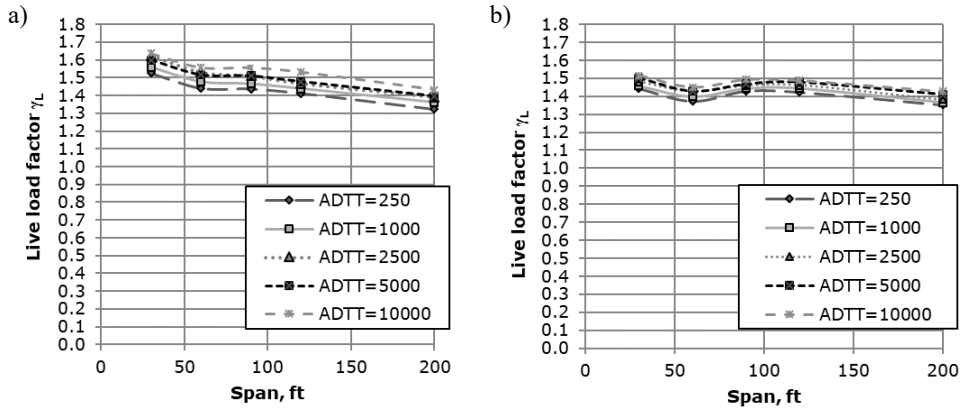


Fig. 4. Live load factor vs. span length for: a) moment, b) shear, for prestressed concrete girders (1 ft = 3.05 m). Source: own study

The resistance factors were calculated using Eq. 15. The results are presented in Fig. 5 for prestressed concrete girders, and they are summarized in Table 2.

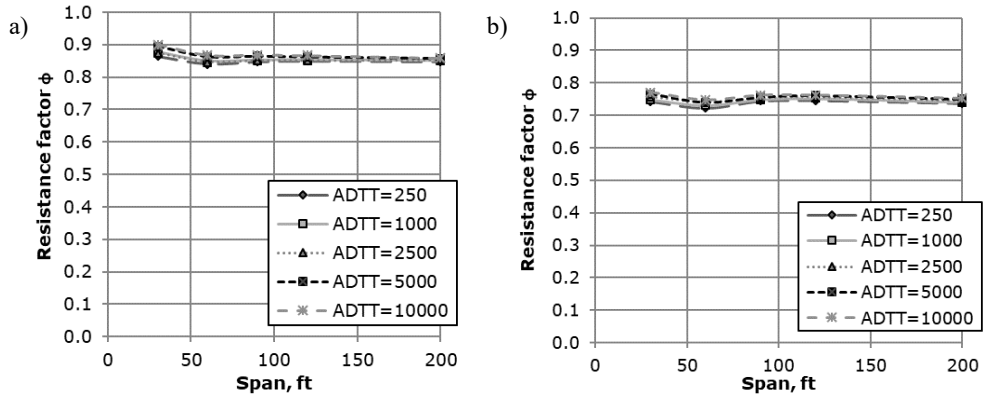


Fig. 5. Resistance factor vs. span length for: a) moment, b) shear, for prestressed concrete girders (1 ft = 3.05 m). Source: own study

Table 2. Current AASHTO resistance factors and calculated resistance factors

Material	Resistance Factor ϕ in Current AASHTO LRFD [3]		Calculated Resistance Factor ϕ	
	Limit State		Moment	Shear
	Moment	Shear		
Prestressed Concrete	1.00	0.9	0.85	0.75

8. Recommended load and resistance factors

The load and resistance factors corresponding to the coordinates of the design point are about 10-15% lower than what is in the current AASHTO Code [1]. The reliability indices calculated for design according to AASHTO [1] are consistent at about 3.5 level (Fig. 2-4). However, the bias factor for live load (Fig. 1) is higher for short spans compared to other span lengths which is an indication that the design live load for short spans has to be increased.

The calculated dead load factor for three components D_1 , D_2 and D_3 is 1.05-1.17. For the dead load due to wearing surface, the statistical parameters are based on assumption about future overlays, and for simplicity of the code, one dead load factor of 1.20 is recommended for all dead load components.

The calculated values of live load factor γ_L are between 1.40 and 1.50. Higher value shows only for a short span, and it is due to the design load being too low. Therefore, live load factor can be 1.50 but a conservative 1.60 is recommended.

Calculated values of resistance factor corresponding to the design point are shown in Table 2. However, it is recommended to increase the listed values by 0.05, which is justified because of conservatism in the dead load factor and live load factor. The recommended “ ϕ ” factors are as shown in Table 3.

$$1.20(D + D_w) + 1.6(L + I) < \phi R \tag{20}$$

Table 3. Current AASHTO resistance factors and recommended resistance factors. *Source:* [3]

Material	Resistance Factor ϕ in Current AASHTO LRFD		Recommended Resistance Factor ϕ	
	Limit State		Moment	Shear
	Moment	Shear		
Prestressed Concrete	1.00	0.9	0.9	0.8

The reliability indices are calculated for the recommended load and resistance factors and compared to the reliability indices corresponding to the current AASHTO and Eq. 2. The results are shown as scatter plot in Fig. 6 for moment and shear. The required moment carrying capacity corresponding to the recommended load and resistance factors is about 35% higher than for the current AASHTO [1] and for shear capacity it is about 5% higher than the current AASHTO [1].

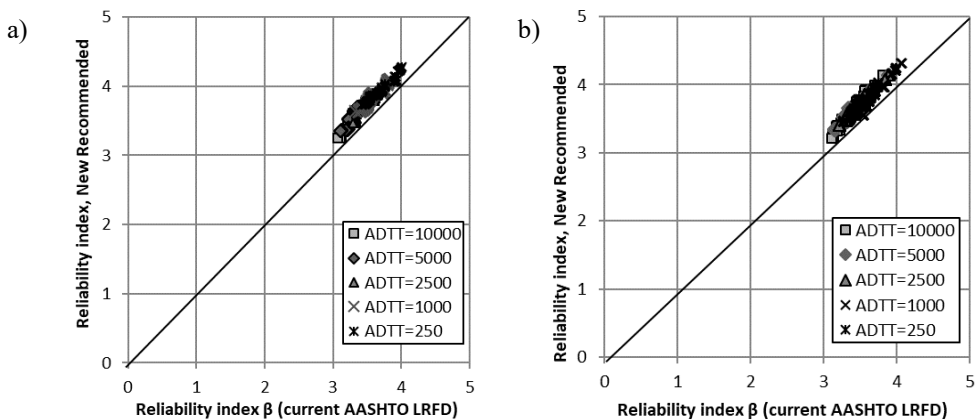


Fig. 6 Reliability indices for new recommended load and resistance factors vs. current AASHTO code: a) moment, b) shear. *Source:* own study.

Recommended load and resistance factors are 1.20 for dead load, 1.60 for live load and resistance factors of 0.90 for steel and P/C girders. Incidentally, these load and resistance factors would then be the same as in ASCE Standard 74 [6], ACI 318 [4], AISC LRFD [5] and National Design Specification for Wood [7].

9. Conclusions

Load factors in the AASHTO LRFD Code [1] were selected so that factored load corresponds to two standard deviations from the mean value. In this study, the optimum load factors are determined as corresponding to the “design point” and they are about 10% lower than specified in the code. The corresponding resistance factors are calculated as corresponding to the target reliability index. The resulting factors are also about 10% lower than in AASHTO Code. The acceptability criterion is, as in the original calibration, closeness to the target reliability index. The selection of load and resistance factors is checked on a set of representative bridges, the same as used in NCHRP Report 3689 [12]. In general, recommended load and resistance factors are about 10% lower than in the current AASHTO [1]. The reliability indices calculated for design cases using the current and recommended new load and resistance factors show a very good agreement.

References

- [1] AASHTO, Bridge Design Specifications, American Association of State Highway and Transportation Officials, Washington, D.C., 2014.
- [2] AASHTO, Bridge Design Specifications, American Association of State Highway and Transportation Officials, Washington, D.C., 2002.
- [3] AASHTO, Bridge Design Specifications, American Association of State Highway and Transportation Officials, Washington, D.C., 2016.
- [4] ACI 318-14, Building Code Requirements for Structural Concrete, American Concrete Institute, Farmington Hills, Michigan 2014.
- [5] AISC LRFD, Manual of Steel Construction: Load and Resistance Factor Design, 14th edition, American Institute Of Steel Construction Inc., Chicago, IL, 2011.
- [6] ASCE Standard 7, Minimum Design Loads for Buildings and Other Structures, American Society of Civil Engineers, Reston, VA, 2016.
- [7] National Design Specification for Wood, American Wood Council’s (AWC), Leesburg, VA, 2015.
- [8] Ellingwood B., Galambos T.V., MacGregor J.G. and Cornell C.A., *Development of a Probability Based Load Criterion for American National Standard A58*. National Bureau of Standards, NBS Special Publication 577, Washington, D.C. 1980.
- [9] Nassif H. and Nowak A.S., “Dynamic Load Spectra for Girder Bridges”, *Transportation Research Record*, no. 1476, 1995, pp. 69-83.
- [10] Nowak A. S. and Collins K.R., *Reliability of structures*. CRC Press, New York 2013.
- [11] Nowak A. S. and Rakoczy A.M., “Statistical Resistance Models for R/C Structural Components”, in *ACI SP-284-6*, vol. 248, 2012, pp. 1-16.
- [12] Nowak A.S., “Calibration of LRFD Bridge Design Code, NCHRP Report 368”, in *Transportation Research Board*, Washington, DC 1999.
- [13] Nowak A.S., Rakoczy A. M. and Szeliga E., “Revised Statistical Resistance Models for R/C Structural Components”, in *American Concrete Institute*, SP-284, 2012, pp. 6-16.
- [14] Nowak A.S., Szerszen M.M., “Calibration of Design Code for Buildings (ACI 318) Part 1: Statistical Models for Resistance”, *ACI Structural Journal*, vol. 100, no. 3, 2003, pp. 377-382.

-
- [15] SHRP2 R19B, “Bridges for Service Life Beyond 100 Years: Service Limit State Design Final Report”, in *Transportation Research Board*, Washington, D.C., 2015.
 - [16] Szerszen M. M. and Nowak A.S., “Calibration of Design Code for Buildings (ACI 318) Part 2: Reliability Analysis and Resistance Factors”, *ACI Structural Journal*, vol. 100, no. 3, 2003, pp. 383-391.
 - [17] Rackwitz R. and Fiessler B., “Structural Reliability under Combined Random Load Sequences”, *Computer and Structures*, vol. 9, 1978, pp. 489-494.
 - [18] Agarwal A. C. and Wolkowicz M., “Ontario Commercial Vehicle Survey 1975”, in *Ontario Ministry of Transportation and Communications, Interim Report, Engineering Research and Development Branch*, 1976.

Research on the recycled and hybrid fibre reinforced self-compacting concrete under flexure

Malgorzata Pająk

*Department of Structural Engineering, Silesian University of Technology,
5 Akademicka Street, 44-100 Gliwice, Poland;
malgorzata.pajak@polsl.pl  0000-0003-2627-9372*

Funding: This work was supported by the Higher Education and National Science Centre for funding the grant no. DEC-2017/01/X/ST8/01864.

Abstract: In the present study the steel fibres coming from the end-of-life tires were applied as a reinforcement of self-compacting concrete. The influence of the recycled fibres and their mixture with glass or polypropylene fibres (hybrid mixes) on the flexural behaviour of SCC was tested. The research revealed that the dosage of 1.5% of recycled fibres is highly effective in the SCC matrix. The values of the residual flexural tensile strengths obtained in the tests classified the R-SCC to be used as a partial replacement of the conventional reinforcement. The addition of other types of fibres to R-SCC caused the further enhancement of flexural parameters with no negative effect on the distribution of the fibres in the mix.

Keywords: recycled fibres, flexure, hybrid fibres, self-compacting concrete

1. Introduction

In general, short fibres are added to the brittle concrete matrix to enhance its tensile mechanical parameters and cracking resistance. The fibres improve the energy absorption capacity of the concrete under dynamic loading. Because of these advantages, fibre reinforced concrete (FRC) is applied in engineering structures, e.g. tunnels, water tanks, protective structures. A broad investigation conducted globally displays an improvement of mechanical parameters of concrete due to the application of the various types of fibres [1]–[3]. However, the research mainly focusses on manufactured fibres.

If the immense need for reduction of the people-produced waste is considered, recycled steel fibres (RSF) were investigated. Precisely, fibres from the end-of-life tires were considered in this paper. The attempts to reveal the effectiveness in improving mechanical parameters of concrete of the fibres from end-of-life tires can be found only in some research [4]–[6]. The problem is associated with their poor efficiency in comparison to the same amount of manu-

factured fibres in improving the flexural parameters of the concrete matrix [5]. In some of the papers, it was proved that when the dosage of RSF is not higher than 60 kg/m^3 , the efficiency of the fibres in the brittle concrete matrix is low [7], [8]. However, even in this case, the RSF had a positive effect on the cracking behaviour of concrete [8].

In this paper, a significant amount of fibres was chosen because so far, the research on the behaviour of concrete with high volume ratio of RSF has been sparse. It is believed it is impossible to apply high amounts of RSF fibres to the concrete matrix because their shape would impede the random distribution of the RSF in the matrix. Furthermore, the influence on of the other fibres on the distribution of the RSF in the concrete matrix is unknown. There is no research on the mixtures, in which the RSF were mixed with other than steel fibres, therefore in this study a blend of steel and waste fibres was tested in section 5 [5] and the flexural response of self-compacting concrete reinforced with mixes of RSF, polypropylene, and glass fibres were investigated. High dosages of all types of fibres were used to highlight their mutual impact on the parameters of the matrix.

This paper is a part of the comprehensive laboratory study on hybrid fibre reinforced self-compacting concrete under quasi-static and high strain rates conditions implemented under a grant. The results presented in the paper cover the flexural response of HFR-SCC. The behaviour of the mix under high strain rates was discussed in sections 9 and 10 [9], [10]. The designation for all the mixtures were the same in all the papers to facilitate the possible linking of data and to draw further conclusions.

The first aim was to investigate when the high-volume ratio of RSF can be applied to the concrete matrix.

2. Experimental program

2.1. Composition of the mix

The research aimed to apply the high-volume ratio of the waste fibres to the self-compacting concrete matrix. The dosage of recycled fibres (R) was equal to 118 kg/m^3 , which corresponds to a volume ratio of 1.5%. Such a large number of fibres decreased the rheological parameters of SCC. Thus, the amount of superplasticizer and water had to be increased with the reference mix. The composition of the mix was assigned with the condition that the slump flow of the plain SCC and recycled fibre reinforced SCC (R-SCC) was equal.

Table 1. Mixture composition. *Source:* own study

Mix	Cement CEM I 42.5R [kg/m^3]	Natural sand (0–2 mm) [kg/m^3]	Coarse aggregate (2–16 mm) [kg/m^3]	Super- -plasticizer [kg/m^3]	Water [kg/m^3]	Steel fibres (%) by volume			w/c [-]
						R	G	PP	
SCC	580	927	695	18.4	202	-	-	-	0.34
R-SCC						1.5	-	-	
RG-SCC	580	927	695	20.3	223	1.5	0.5	-	0.38
RPP-SCC						1.5	-	0.25	

Table 2. Properties of the fibres. *Source*: own study

Type of fibre	Designation	Length [mm]	Diameter [mm]	Aspect ratio (L/D) [-]	Tensile strength [MPa]	Modulus of elasticity [GPa]	Density [kg/m ³]
steel cord (from the end-of-life tires)	R	~2÷30	~0.15	13÷200	≥ 2850	210	7850
glass	G	12	0.014	-	-	-	~2500
polypropylene	PP	12	0.038	-	-	-	910

Natural sand and coarse aggregate were sourced from locally available sources in Silesia in Poland. The pebble aggregate was used. The exact composition of the mixes is presented in Table 1 and Table 2.

Hybrid mixes were created by adding glass (G) or polypropylene (PP) fibres to R-SCC. Dosages of these two types of fibres were also assigned experimentally. The 0.5% of glass fibres and 0.25% of PP fibres were added to the R-SCC. The photos of the fibres used in the analysis are collated in Fig. 1.

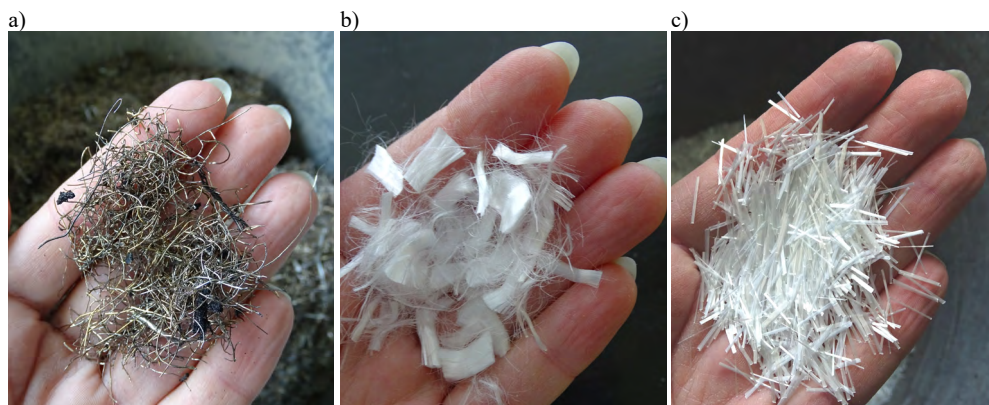


Fig. 1. View of the fibres used in the investigation: a) recycled fibres (R); b) polypropylene fibres (PP); c) glass fibres (G). *Source*: own study

2.2. Flexural tests

Flexural tensile tests were performed to investigate the improvement of the mechanical parameters of SCC after the application of fibres, with accordance with RILEM TC-162 TDF [11] and PN-EN 14651 [12]. Notched beams of the dimensions of 150×150×600 mm were subjected to the constant rate of deflection, equal to 0.2 mm/min. The CMOD was recorded during the tests. The details of the test procedure and stand can be found in other works of the author's dealings with the flexure of FRC, e.g. [13]. For each mix, three beams were tested.

3. Results

The results from broad research, covering the behaviour of hybrid fibre reinforced self-compacting concrete under quasi-static compression and high compression strain rates, were presented in [9, 10]. Values of the quasi-static compressive strengths and accompanying

strains of each mix, which were extensively discussed in previous papers, were presented in this article for the comparison (Table 3). In parenthesis, the coefficients of variation were presented.

3.1. Rheological tests

The slump flow of the plain SCC and R-SCC were designed to be equal. The addition of G or PP fibres reduced the slump flow diameter (SFD) and the time to reach 500 mm spread (t_{500}) of R-SCC (Table 3). During the development of the composition of the mixture, a strong influence of the PP and G fibres on the workability of the SCC was noted. The results from slump flow tests presented in the Fig. 2 indicate that the mix of R and PP fibres disturbed the homogeneity of the mix the most. The research also covered the L-box tests, which showed that none of the mixes was able to pass through the reinforcement in the spacing equal to 30 mm. The exact results were summarized in Table 3.

Table 3. Rheological parameters of HFR-SCC. *Source:* own study

Mix	SFD [mm]	t_{500} [s]	L-box (H_2/H_1) [-]	Compressive strength [MPa]	Strain at peak stress $\times 10^{-3}$ [-]
SCC	680	4	1	57.7 (11)	0.00240 (34)
R-SCC	680	4	0.52	53.5 (2)	0.00273 (12)
RG-SCC	570	7	0.53	58.8 (4)	0.00300 (5)
RPP-SCC	580	6	0.53	52.7 (1)	0.00284 (19)

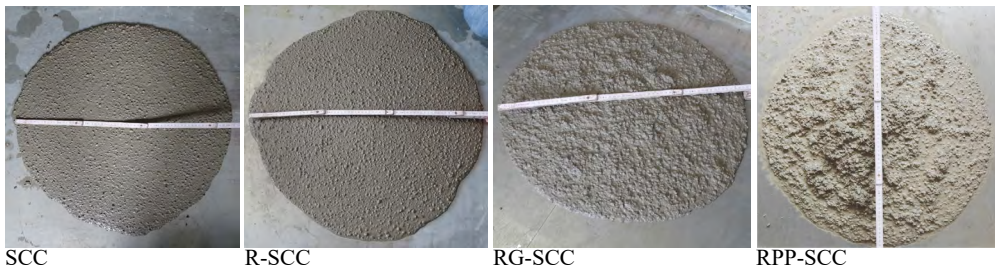


Fig. 2. Slump flow of the mixes. *Source:* own study

3.2. Flexural tensile tests

3.2.1. R-SCC

The results from flexural tests of the mixes were presented as load-CMOD curves in Fig. 3, and Fig. 4. Each graph contains the load-CMOD curves of three beams and their average.

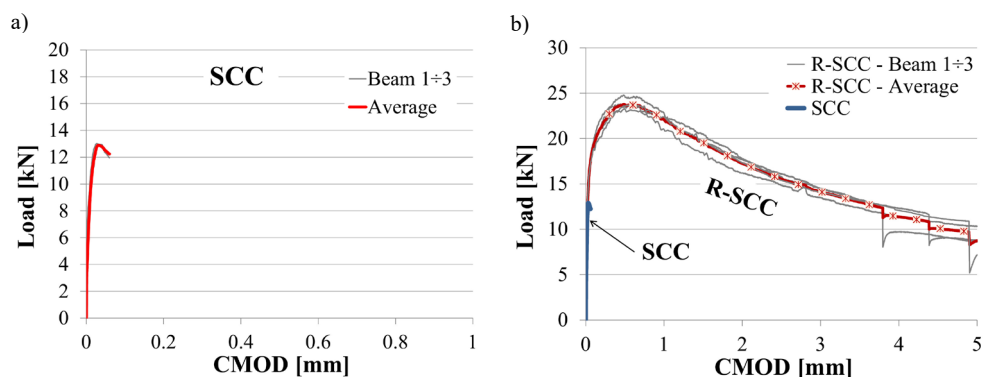


Fig. 3. Load-CMOD curves obtained in flexural tests of mixes: a) SCC, b) R-SCC. *Source:* own study

The application of 118 kg/m^3 of fibres recovered from used tires caused the pronounced enhancement of the mechanical parameters of the SCC (Fig. 3b). The maximum flexural tensile strength of plain SCC increased about twice, due to incorporation of RSF. The post-elastic mechanical parameters of SCC were significantly improved by recycled fibres, which can be seen in the comparison of the results of the tests presented in Fig. 3b. The results of the tests covering, e.g. residual and equivalent tensile strengths were presented in Table 4. The coefficients of variation were presented in parenthesis.

Table 4. Flexural tests results. *Source:* own study

Mix	f_{LOP} [kN]	f_{LOP} [MPa]	f_{max} [kN]	δ_{Fmax} [mm]	Equivalent flexural tensile strength [MPa]		Residual flexural tensile strength [MPa]				Toughness [N/m]	$f_{R,1}/f_{LOP}$ [-]	$f_{R,3}/f_{R,1}$ [-]
					$f_{eq,2}$	$f_{eq,3}$	$f_{R,1}$	$f_{R,2}$	$f_{R,3}$	$f_{R,4}$			
SCC	12.78 (2)	4.09 (2)	12.9 (1)	0.04 (40)	-	-	-	-	-	-	-	-	-
R- SCC	16.78 (2)	5.37 (3)	23.9 (3)	0.32 (21)	7.34 (5)	5.49 (10)	7.60 (3)	6.26 (4)	4.97 (4)	4.15 (3)	61.24 (3)	1.4	0.65
RG- SCC	20.32 (6)	6.50 (6)	27.6 (3)	0.60 (40)	7.10 (13)	6.37 (9)	8.77 (3)	6.69 (6)	5.31 (9)	4.33 (14)	67.26 (6)	1.4	0.61
RPP -SCC	17.79 (3)	5.69 (3)	28.3 (9)	0.38 (26)	8.80 (6)	6.67 (9)	8.95 (8)	7.39 (8)	5.69 (12)	4.62 (11)	71.52 (9)	1.6	0.64

In the research, the hardening phase was observed before reaching the maximum load. This type of flexural response is usually observed in the case of long fibres with the shape that ensures a good anchorage in the concrete matrix. Even high number of straight, short fibres was not able to trigger such an effect on the flexural behaviour of SCC, which was previously investigated in [13]. Therefore, this research proves that the length together with the curved and twisted shape of the RSF provides a very good anchorage of the RSF in the SCC matrix. The fact that the type of steel used in the tires are characterized by much higher tensile strength and ductility than the steel used for the production of typical fibres should also be considered [14].

In the previous work of the author [7], where the dosage of RSF was in the range of $30 \div 60 \text{ kg/m}^3$, their influence on peak and post-peak parameters of concrete were rather weak. No hardening phase in the flexural response was observed in this instance. The increase of the maximum load of concrete reinforced with recycled fibres did not exceed 25% of plain concrete. The meaningful dispersion of the results with the increase of the volume ratio of the fibres was noted. In the current research, this conclusion was not confirmed. A much bigger dosage of the RSF than in [7] was analyzed. The proceedings of the load-CMOD curves were comparable in the case of all the specimens that can be seen in the Fig. 3b. Notably, in [7] the conventional concrete was examined, which means it needs to be vibrated, whereas, in this study, self-compacting concrete was investigated. Thus, probably, the process of vibration was responsible for the dispersion of the results in [7].

3.2.2. Hybrid fibres

The R-SCC mix was further improved with glass (G) and polypropylene (PP) fibres (Fig. 4). Both types of fibres (G, PP) had a comparable influence on the flexural response of the R-SCC. Their addition caused the increase of maximum load and flexural mechanical parameters of the SCC matrix already containing the recycled fibres (Fig. 4).

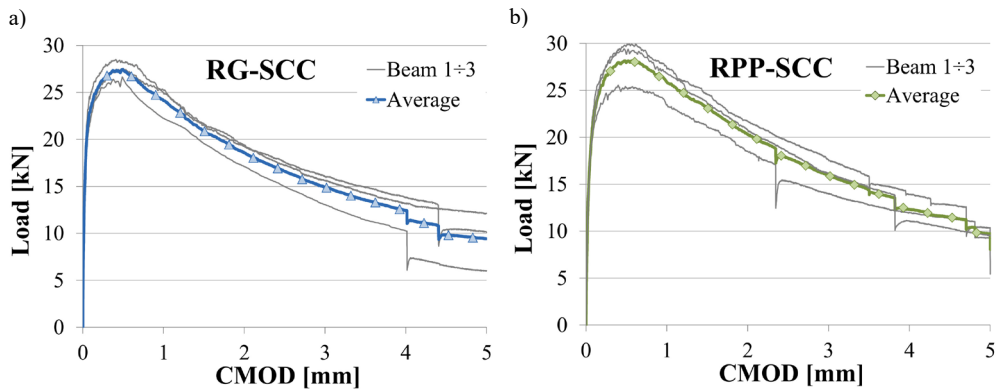


Fig. 4. Load-CMOD curves obtained in flexural tests of mixes containing hybrid fibres: a) RG-SCC; b) RPP-SCC. *Source:* own study

The scatters between the load-CMOD curves of mixes containing hybrid fibres were indeed more noticeable than in the case of the R-SCC (Fig. 3b). However, they still weren't meaningful. Although the dosage of polypropylene and glass fibres was high, it can be concluded that the addition of other types of fibres did not affect the distribution of the recycled fibres.

The comparison of the average load-CMOD curves obtained in all tests are presented in Fig. 5. It can be clearly seen that additional fibres (PP or G) improved the flexural parameters of the R-SCC. Polypropylene fibres seem to be more effective than the glass fibres. However, this difference was not pronounced.

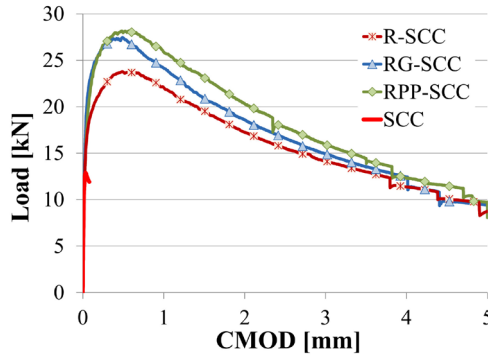


Fig. 5. Comparison of the load-CMOD curves. *Source:* own study

In general, the fibres bridge the cracks in the concrete matrix. Their effectiveness in the brittle matrix depends mainly on the dosage, length and material of the fibres. The shortest fibres can attract microcracks, while the longer ones delay the propagation of more significant cracks. In this paper, the PP fibres in combination with the RSF fibres were more effective in the matrix because their modulus of elasticity is lower than in the case of G fibres. The density of polypropylene fibres is lower than the glass fibres. Thus, the number of PP fibres was much higher in the matrix than in the case of G fibres. The difference in the impact on the load-CMOD relationship is not pronounced because the length of both types of fibres and their perimeter were somewhat comparable.

The investigations showed that the replacement of the manufactured fibres with the recycled ones is possible. The 1.5% of volume ratio of the RSF resulted in the increase of flexural parameters of the matrix. The enhancement that could be compared to the one obtained in the case of hooked fibres is believed to be the most effective in the concrete matrix. However, much smaller dosage of hooked fibres than the RSF would probably produce the same effect on the flexural parameters of the SCC.

4. Application of recycled fibres

There are two main applicable standards that deal with FRC: RILEM TC 162-TDF [11] and MC 2010 [15]. The procedure to obtain mechanical parameters from laboratory investigation that can be further applied in the calculation of FRC according to RILEM TC 162-TDF [11] was previously presented by the author in [7], where lower dosages of recycled fibres than in this paper were analysed. Herein, the approach proposed by MC 2010 [15] was discussed.

Considering the FRC reinforced with conventional bar reinforcement, the fibres carry the load in the tensile zone, which decreases the stress and strain in bars. MC2010 [15] classifies the FRC based on three parameters from flexural tests performed on notched beams: $f_{R,1}$, $f_{R,3}$ and f_{LOP} . According to MC2010 [15], the fibres can be considered in Ultimate Limit State (ULS) calculations when the conditions (1) are fulfilled:

$$\frac{f_{R,1}}{f_{LOP}} > 0.4; \frac{f_{R,3}}{f_{R,1}} > 0.5 \quad (1)$$

In other words, the residual flexural tensile strength of FRC at the CMOD equal to 0.5 mm ($f_{R,1}$) should be higher than 40% of the flexural tensile strength at the limit of proportionality (f_{LOP}). Thus, the fibres had to act in the concrete matrix after the cracking occurred.

Furthermore, when the CMOD reaches 2.5 mm the FRC should still have the residual tensile strength ($f_{R,3}$) not lower than 50% of the residual flexural tensile strength at CMOD = 0.5 mm ($f_{R,1}$) and in truth 20% of f_{LOP} .

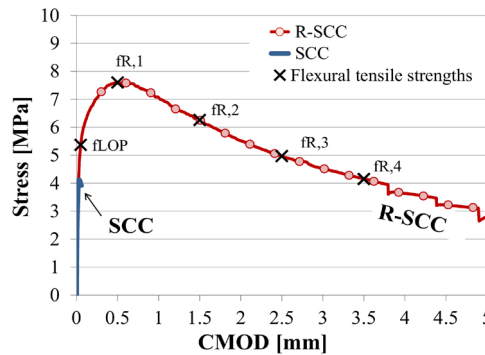


Fig. 6. The average residual flexural tensile strengths-CMOD curve for R-SCC. *Source:* own study

The residual flexural tensile strengths of R-SCC are depicted in Fig. 6. The R-SCC residual strength class acc. to MC 2010 [15] is “a”. It can be clearly seen in Table 4 that the dosage of 1.5% of the RSF exceeds the requirements (1). Though, the RSF could be used as a partial substitute to conventional reinforcement and decrease the number of bars. However, the L-box test results indicate, that the mix with such high dosage of fibres is not able to pass through the reinforcement with a distance of 30 mm. Therefore, it could be applied in, e.g. ground slabs, where the distance between the bars is usually much higher and can't be lower than 50 mm.

5. Conclusions

Based on the investigations performed, obvious advantages for the SCC brittleness with the application of huge amount of RSF can be noted. The main conclusions are:

- The addition of 1.5% of recycled fibres to SCC resulted in pronounced enhancement of the flexural parameters of the matrix.
- Based on the collation of current results with the results from the tests previously performed, it can be concluded that the effectiveness of the RSF was much better in self-compacting concrete than in conventional concrete. Thus, probably the influence of the process of vibration on the results is much higher than it is in the case of manufactured fibres.
- Hybrid mixes containing RSF and glass or polypropylene fibres exhibit higher flexural peak and post-peak parameters than the mixes containing only RSF.
- The addition of glass and polypropylene fibres to the R-SCC did not influence the distribution of RSF in the SCC pronouncedly. The proceedings of the load-CMOD curves obtained for the mixes with hybrid fibres were comparable.
- According to the MC2010, the flexural parameters of all the mixes could be considered in the ULS calculations of the structural elements.

One of the main conclusions from the research is that the manufactured fibres could be replaced by the recycled fibres with the same effect on the flexural parameters of the self-com-

pacting concrete matrix. Admittedly, higher volume ratio of the RSF should be applied to achieve the same effect as it is in the case of manufactured fibres, nevertheless it is possible.

References

- [1] Brandt A.M., “Fibre reinforced cement-based (FRC) composites after over 40 years of development in building and civil engineering”, *Composite Structures*, vol. 86, (2018), pp. 3-9. <https://doi.org/10.1016/j.compstruct.2008.03.006>
- [2] Rizzuti L., Bencardino F., “Effects of Fibre Volume Fraction on the Compressive and Flexural Experimental Behaviour of SFRC”, *Contemporary Engineering Sciences*, vol. 7, (2014), pp. 379-390. <http://dx.doi.org/10.12988/ces.2014.4218>
- [3] Abbass A., Abid S., Ozakça M., “Experimental Investigation on the Effect of Steel Fibers on the Flexural Behavior and Ductility of High-Strength Concrete Hollow Beams”, *Advances in Civil Engineering*, (2019), <https://doi.org/10.1155/2019/8390345>.
- [4] Grolí G., Caldentey A.P., Marchetto F., Fernández F.A., “Serviceability performance of FRC columns under imposed displacements: An experimental study”, *Engineering Structures*, vol. 101, (2015), pp. 450-464.
- [5] Zamanzadeh Z., Lourenço L., Barros J., “Recycled Steel Fibre Reinforced Concrete failing in bending and in shear”, *Construction and Building Materials*, vol. 85, (2015), pp. 195-207.
- [6] Centonze G., Leone M., Aiello A.M., “Steel fibers from waste tires as reinforcement in concrete: A mechanical Characterization”, *Construction and Building Materials*, vol. 36, (2012), pp. 45-67.
- [7] Pająk M., “Concrete reinforced with various amounts of steel fibres reclaimed from end-of-life tires.” in *64 Scientific Conference of the Committee for Civil Engineering of the Polish Academy of Sciences and the Science Committee of the Polish Association of Civil Engineers (PZITB) (KRYNICA 2018)*, MATEC Web of Conferences, vol. 262, 2019.
- [8] Grolí G., Caldentey A.P., Soto A.G., “Cracking performance of SCC reinforced with recycled fibres – an experimental study”, *Structural Concrete*, vol. 15, no. 2, (2014), pp. 136-153.
- [9] Pająk M., Janiszewski J., Kruszka L., “Hybrid fiber reinforced self-compacting concrete under static and dynamic loadings”, in *Proceedings of the Symposium 2019: Concrete – Innovations in Materials, Design and Structures*, 2019, pp. 766-772.
- [10] Pająk M., Janiszewski J., Kruszka L., “Laboratory investigation on the influence of high compressive strain rates on the hybrid fibre reinforced self-compacting concrete”, *Construction and Building Materials*, vol. 227, (2019). <https://doi.org/10.1016/j.conbuildmat.2019.116687>
- [11] RILEM TC 162-TDF, “Test and design methods for steel fibre reinforced concrete. Bending tests. Final recommendations”, *Materials and Structures*, vol. 35, (2002), pp. 579-82.
- [12] PN-EN 14651, “Metody badania betonu zbrojonego włóknem stalowym. Pomiary wytrzymałości na rozciąganie przy zginaniu (granica proporcjonalności LOP)”, (2007).
- [13] Pająk M., Ponikiewski T., “Flexural behavior of self-compacting concrete reinforced with different types of steel fibers”, *Construction and Building Materials*, vol. 47, (2013), pp. 397-408. <https://doi.org/10.1016/j.conbuildmat.2013.05.072>
- [14] Domski J., Katzer J., Zakrzewski M., Ponikiewski T., “Comparison of the mechanical characteristics of engineered and waste steel fiber used as reinforcement for concrete”, *Journal of Cleaner Production*, vol. 158, (2017), pp. 18-28. <https://doi.org/10.1016/j.jclepro.2017.04.165>
- [15] Model Code 2010 – Final Draft, FIB Bulletin, vol. 1-2, (2012).

The experimental investigation of the failure of load-bearing masonry walls supported by a deflecting structure

Adam Piekarczyk

*Department of Building Structures; Faculty of Civil Engineering; Silesian University of Technology;
Akademicka St. 2, 44-100 Gliwice, Poland;
Adam.Piekarczyk@polsl.pl  0000-0002-5790-9560*

Abstract: The paper presents selected results of tests of full-scale masonry walls linearly supported on a deflecting beam. The walls with thin bed joints and unfilled head joints were 4.55 m long and 2.45 m high, and were made of group 1 calcium silicate masonry units. The tests included walls with and without openings.

The tests were carried out in a specially designated and constructed test stand, which allowed simultaneous vertical load on the upper edge of the wall and vertical deflection of the beam supporting this wall. During the test, measurements of mutual displacements of six points on the wall surface were carried out. On both faces of masonry specimens, the changes of the length of the measuring bases connecting these six points were recorded.

Walls without openings were detached from the central part of the supporting beam at a deflection not exceeding 2 mm. Walls with one door opening also cracked at an early stage of tests. In this case, a detachment from the supporting beam and cracking at the ends of the lintel occurred because of the rotation of the pillars connected by the lintel above the opening. In walls with two door openings, first cracks were formed at the ends of lintels due to the rotation of pillars with a small deflection of the supporting beam, less than 3 mm. Whereas, in walls with door and window openings, first cracks occurred under the window and at the end of the lintel in the outer pillar of the wall.

Keywords: AAC blocks masonry, floors deflections, damages of masonry walls, transversal deformations of masonry

1. Introduction

Damage to masonry walls may result from uneven displacements of structural elements adjacent to these walls and on which they are supported. The above-mentioned elements include foundations, lintel beams and ceiling elements, for which a few millimetres of deflection can lead to cracking of masonry walls.

Damage to walls supported on ceilings results from the uneven movement of structural ceiling members. These displacements are most often deflections of reinforced concrete structure. Deflection, which is vital for a masonry wall supported on RC ceiling, is the effect of loads that occur after the erection of masonry and after removal or partial removal of ceiling props. The deflection of the ceiling results from permanent loads that affect the ceiling structure after masonry is erected, i.e. the self-weight of the floors, installations and suspended finishing systems, as well as other finishing materials such as plastering. The other reason of this deflection is imposing of service load which acts directly on the ceiling, and in the case of load-bearing walls, permanent and imposed loads transmitted via these walls from higher floors. It is also worth mentioning that the deflection of the loaded ceiling increases with time due to creep and shrinkage of concrete, and may rise several times over the decades compared to the deflection after the construction of a wall. Due to the low early strength of a wall and rheological processes taking place in the masonry, when determining the deflection of a ceiling after erection of a wall, it is not needed to take into account its self-weight without plaster layers, but only in case if walls are constructed on a completely unpropped ceiling.

Prevention of wall damage usually consists in reducing ceiling deflection at the design and construction stages. When designing, attention should be paid to the appropriate static assumption, including the use of ceilings supported on all edges on supports with the highest possible stiffness, shortening spans of multi-span systems, construction of supports with similar stiffness on all floors. At the construction stage, it is essential to make sure that the walls on the ceiling are erected only after the props have been removed, preferably completely. Masonry walls should be made with the use of deformable cement-lime mortars with normal thickness joints. It is desirable to finish the walls supported on the ceiling in such a way that plasterings of the walls and ceiling are separated from each other. Due attention is also needed to properly connect the vertical edges of the walls with the others, which minimises cracks at the junction. The use of reinforcement placed in masonry bed joints can also reduce the width of cracks, but usually does not prevent their occurrence, especially in the case of the walls with openings. More information on how to limit ceiling deflection, calculations of deflections, and their permissible values can be found in works [1]–[3] and standards [4]–[8].

Part of the results of tests of full-scale walls made of calcium-silicate masonry units was published in articles [9] and [10], and walls made of autoclaved aerated concrete blocks – in paper [11]. Besides, in the paper [12] it was proposed that the ratio of deflection of span length of the linear element supporting the masonry wall should be limited to 1/2000 and that the tensile strength of the masonry should be not less than 0.2 N/mm². In the paper [13], the authors suggest limiting of the ratio of deflection to span length to 1/3330. Studies of masonry walls at a scale 1:2 made of concrete blocks were published in [14]. Limiting the deflection of the structure supporting the masonry walls to 1/500 and 1/1000 of their span length, in the case of walls without openings and with openings, respectively, was suggested in the study [15]. Tests of masonry walls with and without openings supported on reinforced concrete beams are presented in the paper [16]. The tests of walls in the scale with openings made of solid ceramic masonry units was carried out by the authors of the study [17] and [18]. The first cracks occurred at a deflection not exceeding 2 mm, which was about 1/1000 of the span length of the supporting beam. The authors of publications [22]–[26] were also involved in experimental tests and theoretical analyses related to the problem of masonry walls supported on deflecting structure.

2. The specimens and test stand

2.1. The materials and specimens

Specimens were made of group 1 according to PN-EN 1996-1-1 [27] calcium-silicate blocks, 250 mm long, 180 mm wide and 220 mm high; mean compressive strength was determined in accordance with PN-EN 772-1 [28] $f_B = 17.7 \text{ N/mm}^2$ and normalised compressive strength $f_b = 21.8 \text{ N/mm}^2$. Designated masonry mortar with mean compressive strength $f_m = 12.5 \text{ N/mm}^2$ determined according to PN-EN 998-2 [29] standard was used.

Full-scale walls with total nominal length of 4.55 m and nominal height of 2.45 m with thin bed joints and unfilled head joints were tested. The type A walls did not have openings (Fig. 1a). The type B specimens contained one door opening asymmetrical to the vertical axis of the wall (Fig. 1b). The type C walls contained two door openings located symmetrically to the vertical axis of the wall (Fig. 1c). The type D walls had one door and one window opening (Fig. 1d). Above the door openings of the Type B and Type C specimens, single-span reinforced concrete lintels were placed with a section width of 180 mm and height of 220 mm. Above the door and window openings in the Type D walls, there was the double-span continuous lintel with the same cross-sectional dimensions as single-span lintels. The length of the lintel was chosen in such a way that the length of the support on the masonry was not less than 125 mm. Two walls of each type were tested – a total of eight specimens.

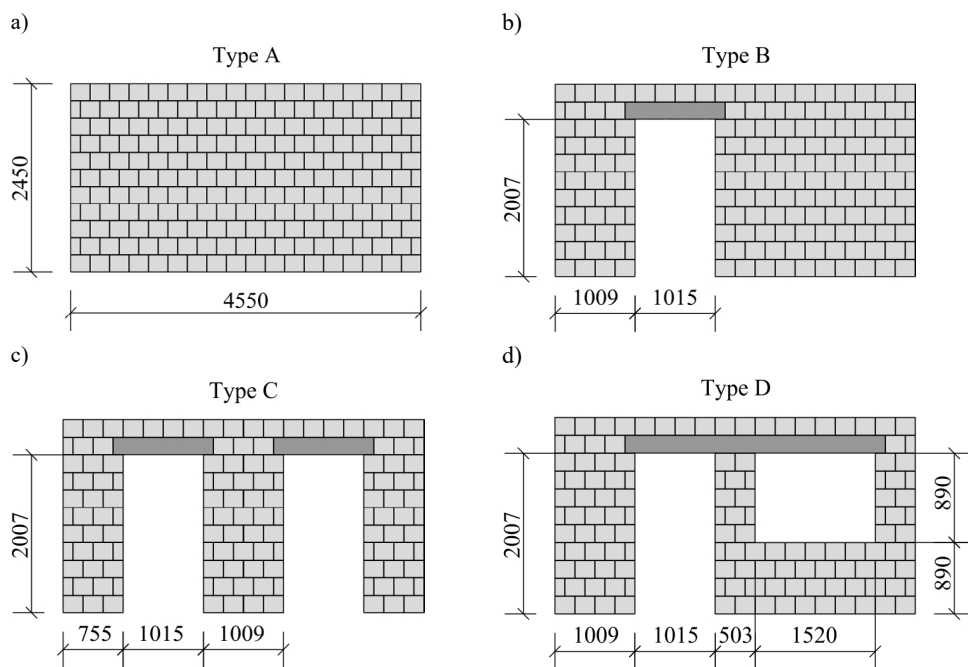


Fig. 1. The full-scale specimens: a) without openings, b) with one asymmetrically arranged door opening, c) with two door openings, d) with door and window openings. Source: the author's own study

2.2. The test stand and testing technique

The tests were carried out in the specially designated test stand shown in Fig. 2. The walls were built directly on a steel beam supported along the entire length during construction

(Fig. 2; item 8). After they were erected, a reinforced concrete ring beam 180 mm wide and 200 mm high was placed on the mortar layer (Fig. 2; item 5). Hydraulic cylinders induced the vertical load in the form of F forces with a range up to 500 kN (Fig. 2; item 3). Measurement of the force F was also made with a load cell with a range up to 500 kN (Fig. 2; item 2). The load was transferred to the specimens via steel transverse beams (Fig. 2; item 4).

The vertical displacements of the beam supporting the masonry wall reflected the deflection of the real reinforced concrete ceiling members, lintel beams or foundations. The flexural rigidity of the steel beam of the stand (Fig. 2; item 8) was intentionally low, thus it was possible to force additional vertical displacements, except for those resulting from the vertical load of F forces. The additional deflection of the structure supporting the masonry wall results from the loads acting directly on the ceiling (self-weight and service loads) and also are the effect of delayed concrete deformations related to creep and shrinkage. Therefore, the vertical beam displacements δ_{vi} in the tests were carried out in two ways. Firstly, the deflection was caused by the vertical load F transmitted through the wall, and then increased to the expected value with a system of elements designed for this purpose and equipped with hydraulic cylinders with a range up to 150 kN and load cells with up to 50 and 100 kN (Fig. 2; item 10 to 13). The deflection of the steel beam supporting the wall was measured using displacement transducers with a measuring range of ± 50 mm attached to steel angles that were connected to the supports of the test stand regardless of the deflecting beam (Fig. 2; item 7). Vertical displacements of the supporting beam were measured on both sides of the wall in 1/6 and 5/6 span (δ_{v1}), in 1/3 and 2/3 span (δ_{v2}) and half-span (δ_{v3}). The expected deflection value was fixed with M30 screws (Fig. 2; item 14).

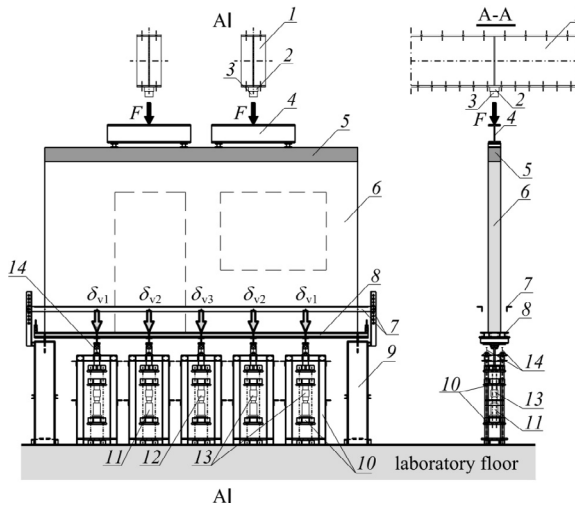


Fig. 2. The test stand: 1 – steel frame, 2 – load cell, 3 – hydraulic jack, 4 – steel crossbeam, 5 – RC ring beam, 6 – tested wall, 7 – members of the system for measuring the vertical displacements, 8 – flexible wall support (steel beam), 9 – beam supports, 10 – elements of the system enforcing vertical displacements, 11 – hydraulic jack with a range up to 150 kN, 12 – load cell with a range up to 100 kN, 13 – load cell with a range up to 50 kN, 14 – screws for fixing the deflections. *Source:* the author's own study

The deformations of the wall along eleven sections of the measuring bases located between six points on the wall surface were also measured. Deformations were recorded on both faces of the specimens. The measuring bases formed two rectangles, each 1.95 m long

and 1.90 m high, which were conventionally described as the left-field “L” and right-field “R” – Fig. 3. Changes in the length of the measuring bases as a result of the action of vertical forces F and deflections δ_{vi} were measured using displacement transducers with a measuring range of ± 5 and ± 10 mm. Eighth deformation angles θ_i were calculated on the basis of the changes in the length of sections indicated as a_i to k_i in Fig. 4. For example, angle θ_6 was determined from the following formula:

$$\theta_6 = \arcsin\left(\frac{c_i^2 - h_i^2 - g_i^2}{2c_i h_i}\right) \tag{1}$$

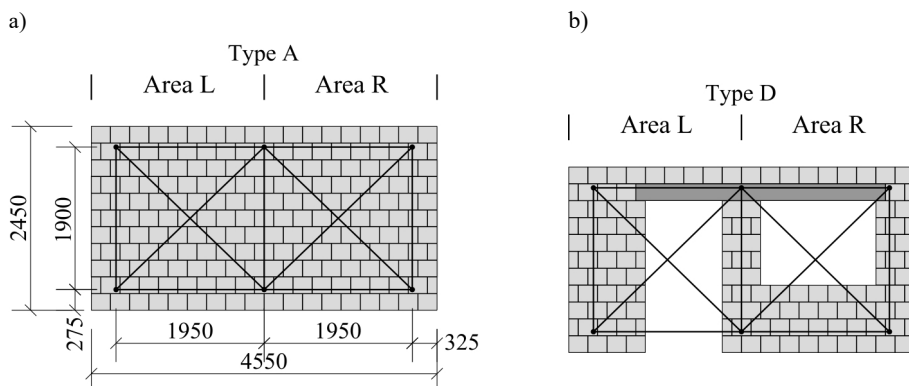


Fig. 3. The areas where measurements of wall deformations were made in the left-field „L” and right-field „R” based on changes in the length of sections of the measuring bases on the example of a wall: a) without openings, b) with door and window opening. Source: the author’s own study

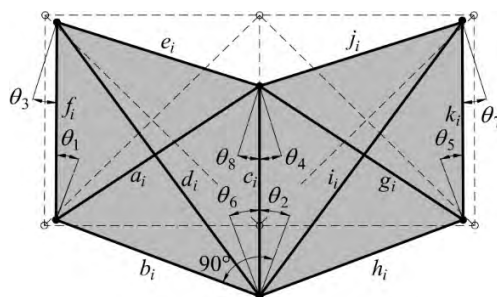


Fig. 4. The diagram of the method for determining the angles of deformation θ_i on the basis of changes in the length of eleven sections of measuring bases $a_i \dots k_i$. Source: the author’s own study

3. The mechanism of wall cracking and discussion of selected tests results

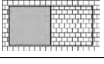
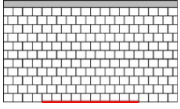
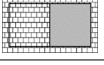

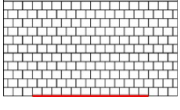


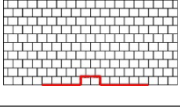


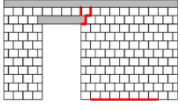
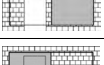
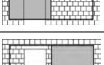
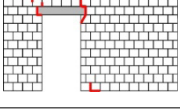
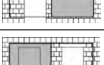
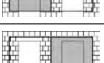
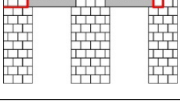
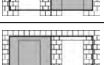
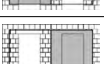
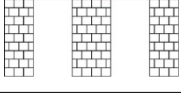
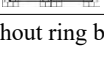
Table 1 summarises selected values of parameters determined at the moment of the first visible occurrence of cracking. Table 2 contains the test results referring to the values obtained at failure of the specimens, for which it was not possible to obtain higher values of F load. Tab. 1 and 2 in column 3 contain the values of the load on the upper edge of the wall p_v , at which the walls cracked p_{cr} and failed p_u given in kN/m^2 , i.e. equal to the average stress value in the horizontal cross-section of the wall as a result of the impact of F forces. The load p_i was determined from the following equation:

$$p_i = \frac{2F_i}{L_1 t'} \tag{2}$$

where F_i is the force transmitted to the wall from a single jack, L_1 is the wall length ($L_1 = 4.55$ m), t is the wall thickness ($t = 0.18$ m).

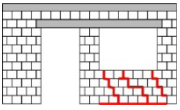
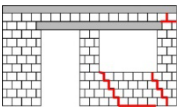
Column 4 summarises the deflection values in the mid-span of the supporting beam $\delta_{1/2,cr}$ and $\delta_{1/2,u}$ accompanying the relevant load p_i . Column 5 in both tables shows the values of the ratio of the corresponding deflection in the middle of the beam span to its length $\delta_{1/2,i}/L$ ($L = 4.5$ m). The values of the deformation angle calculated for the moment of first crack occurrence θ_{cr} and failure θ_u are listed in column 6 on the left “L” and right “R” of the individual walls. Columns 7 and 8 of the tables show a description of the cracking mechanism and drawings which illustrate these damages.

Table 1. Selected test results obtained at the moment of first occurrence of cracking. *Source:* the author’s own study

Wall	Area	p_{cr} kN/m ²	$\delta_{1/2,cr}$ mm	$\delta_{1/2,cr}$ /L	θ_{cr} mm/m	Description of pattern of cracks and damages	
1	2	3	4	5	6	7	8
A-1	L 	0	1.20	1/3750	0.005		
	R 				0.006		
A-2	L 	0	1.40	1/3214	0.013	detachment from the beam	
	R 				0.008		
A-0 ¹⁾	L 	0	1.62	1/2778	0.025		
	R 				0.019		
B-1	L 	0	1.39	1/3237	0.179	at the end of the lintel in wider pillar	
	R 				0.011		
B-2	L 	87.0	1.49	1/3020	0.089	at both ends of the lintel	
	R 				0.016		
C-1	L 	74.0	2.69	1/1673	0.211	horizontal and vertical at the end of the lintel from the external pillars	
	R 				0.134		
C-2	L 	88.0	1.71	1/2632	0.069	horizontal and vertical at the end of the lintel from the internal pillar	
	R 				0.089		

¹⁾ – wall without ring beam

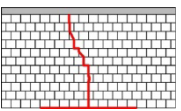
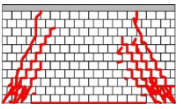
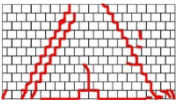
Table 1. (cont.) Continuation from the previous page. *Source:* the author's own study

Wall	Area	p_{cr} , kN/m ²	$\delta_{1/2,cr}$, mm	$\delta_{1/2,cr}$ /L	θ_{cr} , mm/m	Description of pattern of cracks and damages	
1	2	3	4	5	6	7	8
D-1	L	78.0	1.29	1/3488	0.080	no cracks	
	R				0.676	detachment from the beam; oblique cracks under the window	
D-2	L	0	2.00	1/2250	0.216	no cracks	
	R				3.52	detachment from a beam; oblique cracks under the window; horizontal and vertical cracks at the end of the lintel on an external pillar	

For walls with door and window openings, a different cracking and failure mechanism was observed. A common feature was the detachment of the walls from the supporting beam, which in the case of walls without openings and containing both window and door opening always occurred at the beginning of the test with a slight deflection not exceeding 2.0 mm and without the load on the upper edge of the wall or with a small load.

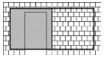
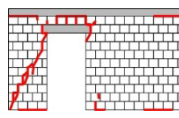
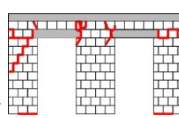
In the case of walls without openings, two types of failure have been observed. One of the walls failed at relatively low load and deflection occurred in a manner typical for bending elements, i.e. a vertical crack running through the entire height of the wall. Two walls without openings failed by diagonal cracks, but in the case of the wall without a reinforced concrete ring beam, a lower ultimate load and associated deflection were observed.

Table 2. Selected test results obtained at walls failure. *Source:* the author's own study

Wall	Area	p_u , kN/m ²	$\delta_{1/2,u}$, mm	$\delta_{1/2,u}$ /L	θ_u , mm/m	Description of pattern of cracks and damages	
1	2	3	4	5	6	7	8
A-1	L	286	6.05	1/744	0.086	vertical crack in the middle of the wall; detachment from the beam	
	R				0.130		
A-2	L	609	25.6	1/176	2.61	oblique cracks from the lower corners; detachment from the beam; crushing of the masonry in the corners	
	R				4.64		
A-0 ¹⁾	L	521	19.7	1/228	3.23	oblique cracks from the lower corners; detachment from the beam	
	R				3.47		

1) – wall without ring beam

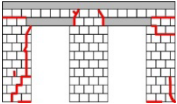
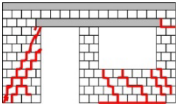
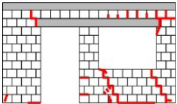
Table 2. (cont.). Continuation from the previous page. *Source:* the author's own study

Wall	Area	$p_{u,}$ kN/m ²	$\delta_{1/2,u,}$ mm	$\delta_{1/2,u}$ /L	$\theta_{u,}$ mm/m	Description of pattern of cracks and damages	
1	2	3	4	5	6	7	8
B-1	L	391	11.2	1/402	12.2	horizontal and vertical at the ends of the lintel; diagonal cracking of the pillar; detachment of a part of the pillar separated by the crack; crushing of the masonry under the lintel; detachment from the beam	
	R						
B-2	L	354	6.59	1/683	6.24	at the ends of the lintel; detachment from the ring beam; detachment from the beam; under the lintel on the wider pillar; the opening of vertical joints over the lintel; diagonal cracking of the external pillar	
	R						
C-1	L	620	23.4	1/192	13.3	horizontal and vertical at the ends of the lintel; under the lintel on the side of the internal pillar; "stepped" cracking of the external pillar; detachment from the supporting beam	
	R						

The first damages of Type B walls with one door opening appeared in the areas at the ends of the lintels and the wall was detached from the supporting beam. The failure of walls of this type consisted of diagonally cracking of the narrow pillar.

In the case of the Type C walls with two door openings, the first cracks occurred at the lintel ends at a deflection not exceeding 3 mm and a load not exceeding 90 kN/m². The failure of this type of walls was manifested by the development of cracks at the ends of the lintels and the creation of a diagonal crack in one of the outer pillars.

Table 2. (cont.) Continued. *Source:* own study

Wall	Area	p_u , kN/m ²	$\delta_{1/2,u}$, mm	$\delta_{1/2,u}$ /L	θ_u , mm/m	Description of pattern of cracks and damages	
1	2	3	4	5	6	7	8
C-2	L	538	22.0	1/205	11.0	horizontal at the end of the lintel on the side of the external pillar; vertical and diagonal at the end of the lintel in the internal pillar; vertical and diag. on the external pillar; detachment from the beam	
	R				12.9	vertical and diagonal at the end of the lintel on the internal pillar; vertical and horizontal at the end of the lintel on the external pillar; vertical on the external pillar; detachment from the beam	
D-1	L	458	15.0	1/300	2.60	diagonal „stepped” cracking	
	R				10.5	vertical and horizontal at the end of the lintel on the external pillar; oblique “stepped” cracks under the window; detachment from the beam	
D-2	L	519	20.0	1/225	3.32	vertical and horizontal at the end of the lintel on the external pillar; diagonal in the corner; horizontal on the internal pillar; detachment from the beam	
	R				15.6	vertical and horizontal at the end of the lintel on the external pillar; opening of vertical joints over the lintel; oblique “stepped” cracks under the window; detachment from the beam; crushing of masonry under the lintel on the external pillar	

The first cracks in Type D walls after the wall was detached from the supporting beam were formed at a deflection not exceeding 2.0 mm under the window opening. They were “stepped” cracks. The failure of this type of wall consisted in crushing the masonry under the longer span of the lintel or diagonal cracking of the outer pillar adjacent to the door opening.

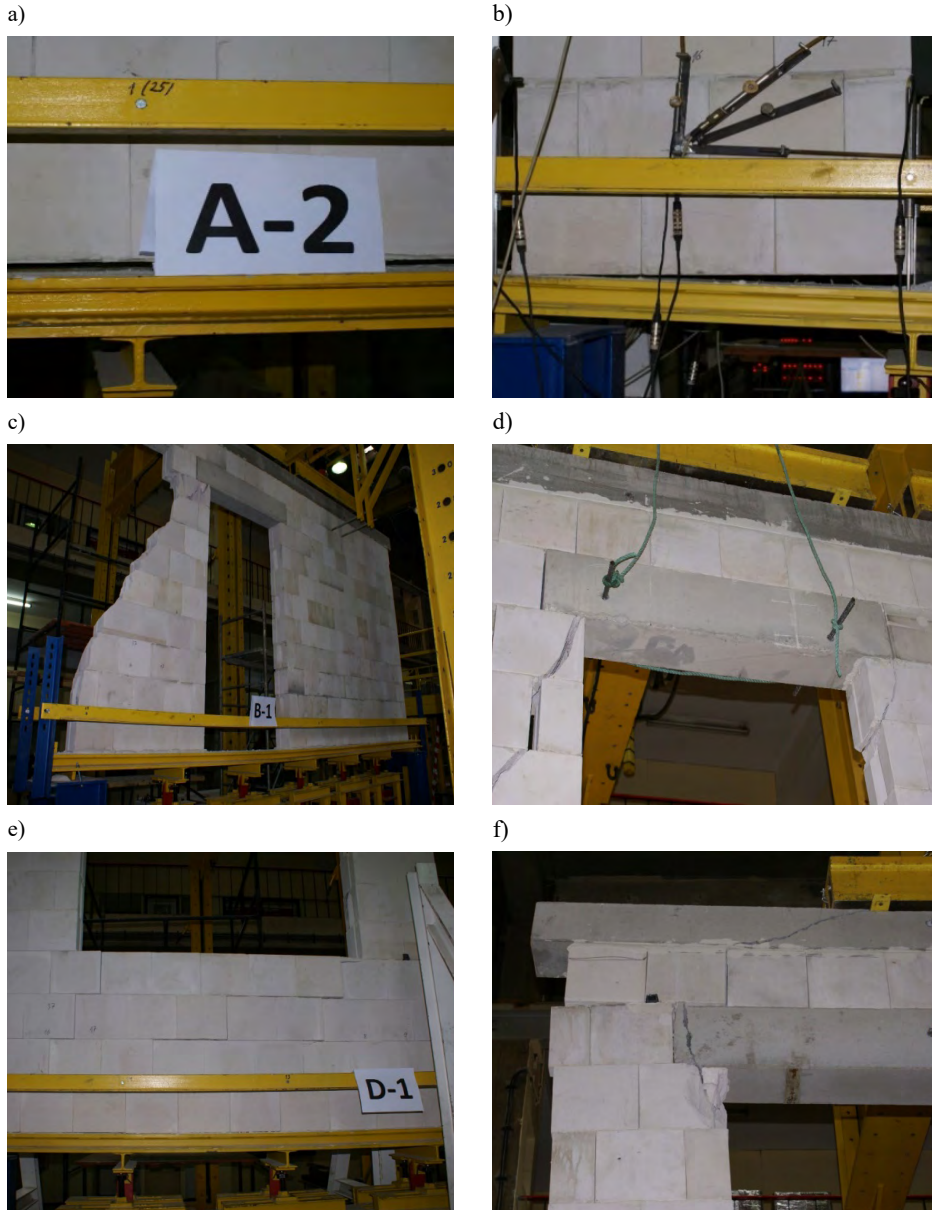


Fig. 5. Photographs of most common ways of cracking and failure of the walls: a) detachment of the lower edge of the A-2 wall, b) detachment of the lower part of the outer pillar of the C-1 wall, c) destruction of the pillar in the B-1 wall, d) destruction of the B-2 wall under the lintel, e) cracks in the wall D-1 under the window opening, f) failure of the outer pillar in the D-2 wall under the lintel. *Source:* the author's own study

4. Conclusions

Based on the tests of full-scale masonry walls subjected to simultaneous compression and the effects of vertical displacements of the beam supporting these walls carried in the above-described range, it could be observed that:

- the first cracks occurred already with a small deflection of the supporting beam, not exceeding 2.7 mm, which was less than 1/1700 beam span and zero or a low vertical load of the upper wall surface; this confirms the conclusions of [12] and [13] papers, which in order to minimise the possibility of damage of masonry walls proposed to limit vertical displacements of wall supporting elements to 1/2000 or even 1/3330 of their span;
- in the case of walls without openings, the detachment from the supporting beam in the central part occurred first;
- in walls with openings, the first cracks usually appeared at the ends of the lintels and also, in the case of walls with window and door openings, in the area of the wall under the window opening;
- one of the walls containing a single door opening and one wall without openings were damaged with deflection less than 1500 of the support beam span;
- in most cases, the deflection at failure did not exceed 1/300 of the span;
- in the case of geometrically asymmetrical walls, the effect of this asymmetry on the deformation angles of the left and right part of the wall was visible; in the Type B walls, the area without a door opening behaved almost like a rigid body compared to the other part of the wall weakened by the opening, which had an impact on the mechanism of failure of this type of wall;
- disproportions of deformation in the case of walls with both window and door opening were slightly smaller, although equally distinct; the part of the wall with a window opening suffered at least four times greater deformations, the measure of which was the angle of deformation.

References

- [1] Drobiec Ł., Kubica J., „Zapobieganie zarysowaniom ścian murowanych opartych na stropach żelbetowych”, *Materiały Budowlane*, no. 4, 2006.
- [2] Nowicki M., „Zapobieganie uszkodzeniom murowanych ścian wypełniających spowodowanych uginaniem się żelbetowych stropów w budynkach mieszkalnych”, *Inżynier budownictwa*, accessed on: 04.02.2014.
- [3] Szulc J., „Ugięcia czynne stropów żelbetowych a uszkodzenia elementów opartych na stropach żelbetowych”, *Materiały Budowlane*, no. 4, 2013.
- [4] PN-EN 1992-1-1 Eurocode 2: Design of concrete structures – Part 1-1: General rules and rules for buildings.
- [5] PN-EN 15037-1 Precast Concrete Products - Beam-and-Block Floor Systems Part 1: Beams.
- [6] ISO 4356 Bases for the design of structures. Deformations of buildings at the serviceability limit states.
- [7] ACI 318-02 Building code requirements for structural concrete.
- [8] DIN 1045-1 Concrete, reinforced and prestressed concrete structures. Part 1: Design and construction.
- [9] Piekarczyk A., Jasiński R., “Distorsions and the way of damaging masonry walls supported on deflected structural elements”, in *16th International Brick and Block Masonry Conference – Trends, Innovations and Challenges*. Taylor & Francis Group, London 2016, pp. 1659-1666.

- [10] Piekarczyk A., "Cracking and Failure Mechanism of Masonry Walls Loaded Vertically and Supported by Deflecting Structural Member", in *3rd World Multidisciplinary Civil Engineering – Architecture – Urban Planning Symposium, WMCAUS 2018, 18-22 June. Prague, Czech Republic*. IOP Conference Series: Science and Engineering, vol. 471, 2019.
- [11] Piekarczyk A., "Reinforced and Unreinforced AAC Masonry Walls Supported on Deflecting Structure", in *6th International Conference on Autoclaved Aerated Concrete, September 4-6, 2018, University Potsdam*. Ce/papers Ernst & Sohn, A Wiley Brand, vol. 2, 2018, pp. 377-387.
- [12] Meyerhof G., "Some recent foundation research and its application to design", *The Structural Engineer*, vol. 32, no. 4, 1953, pp. 55-93.
- [13] Polshin D.E., Tokar R.A., "Maximum allowable non-uniform settlement of structure", in *Proceedings of Fourth International Conference on Soil Mechanics and Foundation Engineering*. Butterworths Scientific Publications, London, vol. 1, 1957, pp. 402-405.
- [14] Rosenhaupt S., "Experimental Study on Masonry Walls on Beams", *Journal of the Structural Division*, (June 1962), pp. 137-166.
- [15] Pfeffermann O., "Deformations admissible dans le batiment", *CSTC Revue*, 1981, Nlt 131, Bruxelles, p. 29.
- [16] Wenzong X., Qinglin W., "A study of the behavior of the supporting beams on walls", in *Third International Symposium on Wall Structures CIB*. Warsaw, vol. 1, 1984, pp. 309-315.
- [17] Holanda G., Ramalho M., Corrêa M., "Experimental and numerical analysis of masonry load-bearing walls subjected do differential settlements", in *Proceedings of the 9th North American Masonry Conference*. Clemenson, USA, 2003, p. 134-145.
- [18] Holanda G., Ramalho M., Corrêa M., "Experimental and numerical analysis of masonry walls with openings subjected do differential foundation settlements", in *Proceedings of the 10th North American Masonry Conference*. St. Louis, USA, 2007, pp. 26-27.
- [19] Henry A.W., *Structural Brickwork*. The MacMillan Press LTD, London, 1981.
- [20] Capozucca R., "An approximate method for analysis of stress distribution in masonry walls", *Masonry International*, vol. 1, 1984, pp. 22-26.
- [21] Henry A.W., Sinha B.P., Davies S.R., *Design of Masonry Structures*. E & FN Spon, London, 1988.
- [22] Valsangkar A.J., Dawe J.L., Seah C.K., "An Evaluation on Masonry Walls-foundation Interaction Using Finite Element Method", in *Proceedings of the British Masonry Society; Proceedings of the Third International Masonry Conference*, no. 6, (March 1994), pp. 144-146.
- [23] Loots J.J., van Zijl G., "Experimental verification of settlement induced damage to masonry walls", in *Proceedings of 13th International Brick and Block Masonry Conference*. Amsterdam, 2004.
- [24] Martens D.R.W., Vermeltoort A.T., "The Effect of the Position of Supports on the Behavior of Composite Masonry Walls", in *Proceedings of 15th International Brick and Block Masonry Conference*. Florianopolis, Brasil, 2012.
- [25] Moraes R.S., Serafim J.A., Parsekian G.A., "Macro modelling of the arch effect: A parametric study", in *Proceedings of 15th International Brick and Block Masonry Conference*. Florianopolis, Brasil, 2012.
- [26] Vermeltoort A.T., "Practical Aspects of Testing Composite Action in Masonry Walls", in *Proceedings of 15th International Brick and Block Masonry Conference*. Florianopolis, Brasil, 2012.
- [27] PN-EN 1996-1-1 Eurocode 6: Design of masonry structures – Part 1-1: General rules for reinforced and unreinforced masonry structures
- [28] PN-EN 772-1 Methods of tests for masonry units. Part 1: Determination of compressive strength.
- [29] PN-EN 998-2 Specification for mortar for masonry Part 2: Masonry mortar.

ISSN 1899-0665